

**LOCALIZING THE EPILEPTOGENIC ZONE
A DYNAMICAL SYSTEMS PERSPECTIVE**

by
Adam Li

A dissertation submitted to The Johns Hopkins University in conformity
with the requirements for the degree of Doctor of Philosophy

Baltimore, Maryland
November, 2021

© 2021 A. Li
All rights reserved

Abstract

Over 15 million epilepsy patients worldwide do not respond to drugs. In focal epilepsy, successful surgical treatment requires complete removal or disconnection of the epileptogenic zone (EZ), a clinically defined brain region that causes seizures. However, there is no agreed upon definition of the EZ that allows prospective identification. Moreover, no biomarker for the EZ exists and thus surgical success rates vary between 30%-70%. In this thesis we develop and validate a new dynamical network-based EEG biomarker - *neural fragility* and demonstrate its utility as a biomarker for the EZ. We first present background related to epilepsy, matrix theory and relevant statistical machine learning. We then present theoretical analyses, retrospective studies on patients collected from multiple centers and in virtual patients with epilepsy using the Virtual Brain neuroinformatics platform. When compared with traditional time-frequency and graph metrics, neural fragility outperforms all other features in predictive power and interpretability.

Thesis Readers

Dr. Sridevi Sarma (Primary Advisor)
Associate Professor
Department of Biomedical Engineering
Johns Hopkins University

Dr. Joshua Vogelstein
Assistant Professor
Department of Biomedical Engineering
Johns Hopkins University

Dr. Nathan Crone
Professor
Department of Neurosurgery
Johns Hopkins University

*Dedicated to my wonderful mother, father, sister, nephew and significant other
who all helped me realize the contents of this thesis.*

Acknowledgements

I have been incredibly fortunate during my PhD to have support from so many people.

First, I would like to thank my advisor, Dr. Sridevi Sarma, who first believed in me when I started graduate school. Her insightful feedback, never-ending support and unwavering attention to details pushed me to become a better scientist, thinker and human being. I would not be who I am today without her guidance throughout the years. Whether it is for a technical presentation, or a new experiment, she always provided valuable and positive feedback. Although I disagreed numerous times with her at meetings, I found that she was always right in the end. I want to thank her for being optimistic even when I was most discouraged. It is difficult to find someone that will consistently believe in you to the degree that Dr. Sarma has and I am grateful to have spent my graduate studies with her.

Next, I would like to acknowledge my mother, Xueqin Li and father, Houshi Li for enabling me to pursue graduate studies and pushing me to always be the best that I can be. Their love and support has enabled me to pursue my passion for science. I would like to acknowledge my sister, Mandi Li, who always served as a role model for me when growing up and my nephew, Alex Li, who inspired me to persevere and cherish the small moments. Finally, I would like to thank my wonderful girlfriend, Soo Kyung Sarah Kim, who has never stopped believing in me and supporting my scientific endeavors. Our conversations enabled me to persevere in the toughest times.

I would also like to thank my committee members, Dr. Nathan Crone and Dr.

Joshua Vogelstein for their valuable guidance throughout my studies. I would like to thank all my collaborators who made collaborative work pleasant and fulfilling. Dr. Crone taught me to appreciate the impact and complexities in clinical problems. Dr. Vogelstein inspired me to pursue a deeper knowledge of statistics and mathematics. I would also like to thank Dr. Viktor Jirsa, who supervised me for one year in his lab at Aix-Marseille University and has continuously served as a great collaborator. He taught me computational modeling and how to utilize the Virtual Brain.

I would also like to thank some notable teachers I had during my childhood. Specifically, Scott Holloway, whom taught with excitement and enthusiasm in my first AP Physics class. He imprinted a love for science and mathematics when applied to the physical world. It was this early experience that motivated me to pursue mathematics and engineering in my undergraduate studies. I would like to thank all my undergraduate and graduate professors who took the time to teach me and inspire me to pursue knowledge. Specifically, Dr. Todd Coleman who gave me my first exposure to machine learning in medicine, and Dr. Carey Priebe for exposing me to the fundamental concepts of the bias-variance tradeoff in statistics.

In addition, I would like to thank my lab mates who have collaborated with me and made late nights in the lab bearable. They made conference trips a blast and I am lucky to have spent so much time around such strong and intelligent women and men. I would also like to thank extremely talented undergraduate students that I have had the fortune of working with: Anil Palepu, Chester Huynh and Patrick Myers. Each one of them contributed as co-authors on papers with me and shown me how exciting it can be to be a mentor in science. Finally, I would like to thank my housemate of 6 years, Sean Murphy, who taught me an appreciation for board games, schnauzers, friendship and organization.

Contents

Abstract	ii
Dedication	iv
Acknowledgements	v
Contents	vii
List of Figures	xi
Chapter 1 Introduction	1
Epilepsy	1
Drug-resistant epilepsy and the epileptogenic zone	1
Diagnosing epilepsy	2
Drug treatment paradigms	3
Surgical treatment paradigms	4
Computationally defining the epileptogenic zone	5
Prior methods in computational localization of the EZ	5
Aims and Hypotheses of This Thesis	9
Aim 1: Develop an Epilepsy EEG Data Platform	10
Aim 2: Develop and Test Localization Model on iEEG Data	11
Aim 3: Validate Localization Model on Intraoperative and Postoperative Data	11

Chapter 2 Neural fragility - a dynamical networked-system representation of the epileptic network	14
Linear systems	15
A review of matrix perturbations	19
Neural fragility - A structured rank-one perturbation	23
Chapter 3 A Retrospective Study: Neural Fragility as an EEG Marker of the Epileptogenic Zone	26
Methods	27
Data collection	27
Preprocessing of data	29
Neural fragility of iEEG network	29
Baseline features - spectral features	32
Baseline features - graph analysis of networks	34
Experimental design	36
Pooled Patient Analysis	36
Non-parametric Decision-Tree Classifier	37
Hyperparameters	38
Structured Heatmap Input	38
Nested Cross-Validation Feature Evaluation	39
Statistical analysis	40
Feature evaluation using predicted probability of successful surgery	41
Spatiotemporal feature heatmap interpretability	42
Fragility heatmaps are more interpretable than all other EEG feature maps	43
Data availability	45
Code availability	45
Results - Neural fragility can localize the epileptogenic zone	45

Neural fragility agrees with clinicians on successful surgical outcomes	47
Neural fragility disagrees with clinicians on successful surgical outcomes	48
Neural fragility outperforms other features in predicting the surgical outcome of patients	49
Neural fragility correlates with expected clinical covariates	52
Discussion	54
Challenges in validating iEEG features as SOZ markers	54
Clinical case complexity and surgical outcomes	54
Limitations of the most popular iEEG features	54
 Chapter 4 Neural Fragility of the Intracranial EEG Network During Intraoperative and Postoperative Monitoring	 70
Methods - Dataset and Code	73
Ethics Statement	73
Data availability	73
Code availability	74
The Hospital for Sick Children	74
The Virtual Brain Data	75
Methods - Analysis	75
iEEG Data Preprocessing	75
Neural Fragility Analysis	76
Time Frequency Representation Analysis	77
The Virtual Brain Patient-Specific Modeling	78
Statistical Analysis	83
Results	83
Neural fragility of an iEEG network	85
Neural fragility modulates after complete, partial and incomplete resec- tion of the EZ in simulation	86

Neural fragility decreases in patients with successful resections	87
Neural fragility increases in patient with failed resection	87
Comparing neural fragility and time-frequency spectral features of iEEG	88
Discussion	89
The effect of anesthesia on epileptic dynamics	89
Neural fragility compared to traditional proposed features of the EZ .	89
Conclusions and general discussion	97
Challenges in validating iEEG features as SOZ markers	97
Clinical case complexity and surgical outcomes	99
Virtual epileptic patients can guide EZ hypotheses	99
Why Neural Fragility Performs Well	100
Converging to a prospective definition of the EZ	101
Outlook of neural fragility and continuous post operative iEEG	102
Scientific and Technological Advances Emerging from Neural Fragility . . .	103
References	105
Appendix IAppendix	119
A. Estimating a linear time-invariant model from data	119
B. Supplementary Figures	121
Curriculum vitae	123

List of Figures

Figure 1-1 Different theories of the epileptogenic zone - (A) Shows Penfield-Jasper theory, where the EZ is contained only in the initial onset zones.(B) shows Tailarach-Bancaud theory, where they emphasize the extended EZ that includes the initial onset zone as well as the regions of seizure propagation. And (C) shows the Spencer theory of the EZ, where epileptogenicity is spread throughout the neural network.	3
Figure 1-2 Pathways to epilepsy surgery - A flow chart of how an epilepsy patient will arrive at surgical treatment.	12
Figure 1-3 Clinical process of EZ localization - A schematic of what occurs clinically to localize the EZ by i) starting with ECoG, or sEEG implantations, ii) analyzing EEG signatures, then iii) formulating a clinical hypothesis about where the SOZ is, iv) performing surgery at the proposed brain regions and finally v) measuring outcome of the surgery with at least 12 months of follow up.	13
Figure 2-1 Intuition of neural fragility - unbalanced and balanced networks (Top) iEEG traces in between seizures (left) and during a seizure (right). (Bottom) network schematic showing change in connectivity (right) in fragile node that causes seizure.	

Describes qualitatively the concept of neural fragility in the context of a dynamical iEEG network, with nodes representing excitatory (E) and inhibitory (I) population of neurons. From a dynamical systems point of view, such imbalance arises from a few fragile nodes causing instability of the network in the form of over-excitation, or under-inhibition. We define fragility of a network node to be the minimum-energy perturbation applied to the node's weights on its neighbors before rendering the network unstable [77, 81]. In systems theory, stable systems return to a baseline condition when a node is perturbed. In contrast, unstable systems can oscillate and grow when a node is perturbed. In the context of epilepsy, a fragile node is one that requires a smaller perturbation to lead to seizure activity. Fragility theory can be modeled in the context of linear dynamical systems: $x(t + 1) = Ax(t)$. Perturbing the columns of the A matrix will alter dynamical connections of a particular node (i.e. that column) on its neighbors, resulting in an imbalanced network. 16

Figure 2-2 Neural fragility in a 2-node network To build quantitative intuition on what neural fragility means in the context of a dynamical iEEG system, we construct a 2-node EEG network example with an excitatory (E) and inhibitory (I) population of neurons. For a qualitative description, see Figure 2-1. $x_I(t)$ and $x_E(t)$ are the EEG activity of the I and E neuronal population respectively. 'A' is a linear network model quantifying how each population affects the rest over time. Δ (i.e. the fragility), is the amount of change added to a node's connections. The

fragility of the node is quantified as the minimal amount of change necessary to cause seizure-like phenomena. **(a)** shows a stable network without a perturbation added, such that the network responses due to an impulse at I result in a transient that reverts to baseline. **(b)** shows a perturbation added, but the network is still stable with a slightly larger transient when an impulse is applied to node I . Then **(c)** shows enough of a perturbation is added, such that the network becomes unstable; an impulse applied at node I results in oscillatory activity that does not quickly return to baseline. The magnitude of the Δ added in **(c)** is the fragility of node I (i.e. $\sqrt{8}$). 17

Figure 2-3 Three perturbation topologies in $\mathbf{R}^{N \times N}$ - **(A)** Diagonal perturbations only disrupt autofeedback terms. **(B)** Column perturbations have non-zero entries in a single column while **(C)** row perturbations have a single row with non-zero entries. 24

Figure 3-1 Clinical complexity and our experimental paradigm **(a)** Schematic of the difficulty of different epilepsy etiologies that might arise in DRE patients. Since there is no biomarker for the EZ and it is never observed directly, the network mechanisms that cause seizures are complex. Case clinical complexity ordered by increasing localization difficulty: lesional (1), focal temporal (2), focal extratemporal (3), and multi-focal (4) that are present in the dataset. These four categories simplify the possible epilepsy presentations, but provide a broad categorization of simple to complex cases observed in the clinic. **(b)** Schematic of our experimental design. **(bottom row)** Shows a simplified analogous workflow that clinicians take to evaluate

their confidence in a proposed *SOZ* localization resulting in a surgery. During invasive monitoring, clinicians identify the *SOZ* from iEEG patterns (e.g. spiking/rhythmic activity). When possible, subsequent surgical resection or laser ablation, generally including the *SOZ* along with a variable extent of additional tissue, is performed. Post-operatively, patients are followed for 12+ months and categorized as either success, or failure, resulting in an Engel or ILAE score. **(top row)** We evaluate various representations of iEEG in the form of spatiotemporal heatmaps, creating a partitioned summary of the clinically annotated *SOZ* around seizure onset, feed them into a Random Forest classifier and compute a probability of success (i.e. a confidence score) in the clinically hypothesized *SOZ*. The probability was then compared with the actual outcome of patients. These predictions can then be stratified based on clinical covariates, such as the actual surgical outcome. For a feature to be an accurate representation of the underlying epileptic phenomena, the following assumptions are made. As a result of seizure freedom, assume that the clinically hypothesized *SOZ* was sufficient, and the probability of success has a high value. In contrast, if seizures continue, then the *SOZ* was not sufficient and the probability should have a low value. . . . 30

Figure 3-2 Computational experiment setup for all candidate *SOZ* features and statistical analysis - (a) Any candidate feature that can produce a spatiotemporal heatmap was computed from EEG data and then partitioned by the clinically annotated *SOZ* set and the complement, SOZ^C (i.e. non-*SOZ*

electrodes) to compute a confidence statistic measuring the feature’s belief of the clinician’s hypothesis. Here F_{SOZ} and F_{SOZ^c} were the feature values within their respective sets. f_θ is the function depending on the Random Forest model parameters, θ that maps the statistics of the F_{SOZ} and F_{SOZ^c} to a confidence statistic. An ideal feature would have high and low confidence for success and failed outcomes respectively. Each point on the final CS distribution comparisons represent one patient. **(b)** A more detailed schematic of how our proposed fragility and baseline features were computed from EEG data for a single snapshot of EEG data. See fragility methods section for description of x , A and Δ 33

Figure 3-3 Baseline feature evaluation schematic - An schematic describing how we processed baseline features, such as spectral power, and graph metrics. The feature heatmap processing is exactly the same as fragility, allowing us to compare the feature representations of neural fragility, spectral power and graph metrics of correlation and coherence derived graphs for the purposes of SOZ localization. 35

Figure 3-4 Pooled fragility distribution analysis for all patients - failed **(a)**, no surgery **(b)** and successful surgery **(c)** datasets. Each SOZ (soz in blue bars) and SOZ^c ('nsoz' in orange bars) distribution per patient was bootstrap sampled (see [Methods](#) for more information on sampling) and then compared using the one-sided Mann-Whitney U test. The corresponding test yielded a statistic of 2776334 (PValue = 0.355) for the failed patient outcomes and a statistic of 36836739 (PValue = 3.326e-

70) for the successful patient outcomes. The patients without resection were not included in the analysis comparing to outcome, but these patients can present as interesting case studies where the SOZ was hypothetically localizable, but perhaps was too close to eloquent areas. 55

Figure 3-5 Patient-specific *SOZ* vs *SOZ^C* neural fragility near seizure

onset - Red *SOZ* vs black *SOZ^C* signals for patients presented in Figure ??: Patient_01 (a), Patient_26 (b), Patient_40 (c). For each patient, the ictal snapshots available are visualized around seizure onset with 5 seconds before onset until the first 20% of the seizure. Not necessarily all electrodes in the clinically annotated *SOZ* are part of the EZ when the patient had a successful outcome. Therefore, if neural fragility had value in contrasting true EZ electrodes from non-EZ electrodes, then any extra electrodes clinically annotated in the *SOZ* should have relative lower fragility. The lines represent mean +/- sem. 57

Figure 3-6 Pooled-patient per clinical center *SOZ* vs *SOZ^C* neural

fragility - Red *SOZ* vs black *SOZ^C* fragility signals for pooled patients within each of the five centers with successful (a) and failed outcomes (b) for NIH (n=14), JHH (n=4), CC (n=61), UMH (n=5), and UMMC (n=7) (top to bottom respectively). Note UMMC only had successful outcomes, so there was no curve for the failures. Seizure periods were resampled and normalized to 100 samples for averaging and viewing purposes. In JHH and UMH, there were only one and two patients in successful outcomes respectively. The lines represent mean +/- sem. 59

Figure 3-7 Fragility heatmaps, and corresponding raw EEG traces of successful and failed outcome patients. (a) From top to bottom, Patient_1 (success, NIH treated, CC1, Engel score 1), Patient_26 (failure, JHH treated, CC3, Engel score 4), and Patient_40 (failure, CCLinic treated, CC4, Engel score 3) are shown respectively. The color scale represents the amplitude of the normalized fragility metric, with closer to 1 denoting fragile regions and closer to 0 denoting relatively stable regions. **(Left)** Overlaid average neural fragility value of each electrode in the window of analysis we used. Black dark squares represent a depth electrode that is not shown easily on the brain. Black lines outline where the clinicians labeled *SOZ*. Note in Patient_26, RAD and RHD electrodes are denoted by the squares with the color showing the average over the entire electrode. **(Right)** Clinically annotated heatmaps of the implanted ECoG/SEEG electrodes with red y-axis denoting *SOZ* contacts. The red contacts are also part of the surgical resection in these patients. Data is shown in the turbo colormap. Best seen if viewed in color. **(b)** Corresponding raw EEG data for each patient with electrodes on y-axis and time on x-axis with the dashed white-lines denoting seizure onset. Each shows 10 seconds before seizure onset marked by epileptologists, and 10 seconds after. EEG was set at a monopolar reference with line noise filtered out. Not all electrodes are visualized in the brain plot because channels that were deemed noisy, or in white matter were not included in analysis (for more information, see Methods Section). In addition, only a select set of channels are chosen for

the heatmap and time-series for sake of visualization on a page and to demonstrate select channels that demonstrated different fragility values. Each EEG snapshot is shown at a fixed scale for that specific snapshot that was best for visualization, ranging from 200 uV to 2000 uV. 60

Figure 3-8 Entire fragility heatmap of seizures in successful and failed surgical outcomes

- Fragility heatmaps with electrodes on y-axis and time on x-axis with the dashed white-lines denoting seizure onset and offset. Shows a period of 30 seconds before seizure onset and 30 seconds after seizure offset. **(a)** Shows clinically annotated maps of the implanted ECoG/SEEG electrodes with red denoting SOZ contacts. **(b)** shows spatiotemporal fragility heatmaps for example of successful outcome (Patient_01), and failed outcome (Patient_26 and Patient_40). The color scale represents the amplitude of the normalized fragility metric, with closer to 1 denoting fragile regions and closer to 0 denoting relatively stable regions. The contacts in red and orange are part of the SOZ and RZ, respectively as defined in Methods section. Note that the red contacts are also part of the RZ. Within the seizures, estimating the linear systems are not as stable, which can be seen by fragility "everywhere" in the map. Visualized with Turbo continuous colormap. Best seen if viewed in color. 62

Figure 3-9 Area under the curve and average precision performance.

Specific results for neural fragility are marked in red for each of the panels (a-d). **(a)** Discrimination plot (measured with AUC) shows the relative performance of benchmark

outcome (see Methods section). Fragility and the top-3 baseline features in terms of AUC are visualized. The shaded area represents the standard deviation of the curve obtained by linear interpolation for visualization purposes. The AUC of fragility obtained a 0.88 ± 0.064 over the 10 standard deviation with a relative improvement of 7.2% improvement in AUC compared to the next best feature representation (i.e. the beta frequency band). At the Youden point (stars), neural fragility obtains a balanced accuracy score of 0.76 ± 0.06 , and an improvement of 0.32 in TPR and 0.32 in FPR compared to the clinical operating point (red star). **(b)** The average PR curve showing that fragility is better than the top 3 features by at least an average precision of 0.04. **(c)** A paired estimation plot showing how the same test set of patients differed in AUC depending on whether it was using the fragility, or beta feature heatmap representation. The paired Cohen's D effect size was computed at -0.975 (-1.97 to -0.29; 95% CI). The p-values associated with the difference between Neural Fragility and the Beta frequency band were 0.0204, 0.0273, and 0.0225 using the one-sided Wilcoxon rank-sum test, permutation test, and the paired student t-test respectively. **(d)** Calibration curve showing the fraction of actual successful surgical outcomes on the y-axis vs the average CS output on the x-axis. The curve measures how calibrated the predicted success probability values are to the true risk stratification of the patient population. The closer a curve is to the $y = x$ line, then the more calibrated a model is. It is quantified by the Brier-loss (closer to 0 is better), which is

shown in the legend, and is significantly lower than the next best feature (an improvement of 15%). The shaded region represents 95% confidence interval of two standard deviations.

65

Figure 3-11 Neural fragility of patients stratified by clinical covari-

ates. (a) Distribution of success probability values per patient stratified by clinical complexity (CC; see [Methods - Data collection](#)), where lesional (1) and temporal lobe epilepsy (2) patients have similar distributions because they are generally the "easier" patients to treat, whereas extratemporal (3) and multi-focal (4) have lower general probabilities because they are "harder" patients to treat. It is important to note that the classification experiment posed did not explicitly optimize this separation between clinical case complexities. There is a median predicted probability of success of 0.59 (boxplot summary = 0.06, 0.88, 0.31, 0.75; min, max, first quartile, third quartile) for CC 1. For CC2, CC3, and CC4, there is a median probability of success of 0.62 (boxplot summary = 0.14, 0.96, 0.40, 0.80), 0.28 (boxplot summary = 0.07, 0.77, 0.14, 0.55), and 0.26 (boxplot summary = 0.07, 0.61, 0.20, 0.33) respectively. **(b)** The distribution of the probability values per patient stratified by Engel score. Due to the AUC being high for fragility, it is expected that Engel I has high predicted probability of success, while Engel II-IV have lower success probability. However, the relative downward trend in the success probabilities from Engel II-IV indicated that neural fragility is present in the clinical *SOZ* in varying degrees from Engel II-IV, suggesting that it correlates with the underlying severity of failed outcomes. Engel IV has the lowest

average predicted probability of success as expected. Engel I, II, III, and IV subjects had a median predicted probability of success of 0.63 (boxplot summary = 0.09, 0.96, 0.46, 0.80), 0.27 (boxplot summary = 0.07, 0.72, 0.14, 0.45), 0.30 (boxplot summary = 0.07, 0.71, 0.25, 0.38) and 0.20 (boxplot summary = 0.06, 0.85, 0.10, 0.24) respectively. (c) A similar distribution for another measure of surgical outcome, the ILAE score, where 1 are considered success and 2-6 are considered failure. Here, ILAE 2-5 follow a decreasing trend with ILAE-6 having the lowest average predicted probability of success. ILAE 1-6 has a median predicted probability of success of 0.63 (boxplot summary = 0.09, 0.96, 0.46, 0.80), 0.34 (boxplot summary = 0.21, 0.88, 0.29, 0.60), 0.30 (boxplot summary = 0.07, 0.72, 0.11, 0.60), 0.26 (boxplot summary = 0.07, 0.85, 0.20, 0.33), 0.20 (boxplot summary = 0.06, 0.52, 0.11, 0.37), and 0.16 (boxplot summary = 0.08, 0.33, 0.09, 0.22) respectively. 66

Figure 3-12 Estimated feature importance (mean and stdev) of the associated fragility heatmap used estimated using permutation - The metric of interest was the concordance statistic (i.e. AUC) of the ROC curve. The original feature map is transformed into a 20-dimensional set of time-varying statistics of its *SOZ* and *SOZ^C* electrodes describing the quantiles of the spatiotemporal heatmap (10% - 100% quantiles). This time-varying summary allows these heatmaps to be pooled together across subjects when training a Random Forest classifier as described in Methods section. 67

Figure 3-13 Neural fragility vs frequency power values - Fragility ver-

sus frequency power in the delta, theta, alpha, beta, gamma and highgamma band for Patient_01, Patient_26, and Patient_40. For band definitions, refer to ?? - ??. Every point represents the spectral power and neural fragility value from a randomly chosen window and electrode from one of the patients. No significant correlation is seen or computed from the data. Each spectral feature and fragility are normalized as described in Methods section. 68

Figure 3-14 Interpretability ratio of feature heatmaps - (a) Two heatmap examples of a seizure snapshot of Patient_01 (NIH treated, ECoG, CC1, Engel I, ILAE 1) with the beta frequency band (left) and the neural fragility heatmap (right). Both colormaps show the relative feature value normalized across channels over time. The black line denotes electrographic seizure onset. **(b)** A box plot of the interpretability ratio that is defined in Results Section computed for every feature. The y-axis shows an effect size difference between the interpretability ratios of success and failed outcomes. The interpretability ratio for each patient’s heatmap is defined as the ratio between the feature values in the two electrode sets ($\frac{SOZ}{SOZ^c}$). Neural fragility is significantly greater than the beta band (alpha level=0.05). 69

Figure 4-1 Clinical workflow with continuous iEEG monitoring before and after a surgical resection An overview of the DRE treatment clinical procedure. Patients are accepted into the Epilepsy Monitoring Unit (EMU) and implanted with intracranial electrodes to undergo monitoring. They are typically in the EMU for many days, up to a few weeks. Pre-resection

being perturbed. Similarly, the norm of the Δ matrix can be computed as a row perturbation over the N nodes, where the perturbation matrix computed has a rank-1 structure with 0's in every row except for the node being perturbed. **(D)** The row and column fragility are combined as a product for all electrodes at every single time point. **(E)** This is then summarized as a spatiotemporal heatmap. **(F)** Taking iEEG data from preresection sessions, we compute heatmaps and then compare these with **(G)** postresection sessions. When we compare the spatiotemporal values between the two sessions using a bootstrap sampling procedure, we expect **(H)** successful surgeries to have a positive effect size. **(I)** Partially failed surgeries, where the EZ is not fully captured, should result in smaller, but still positive effect size. **(J)** Finally, a failed surgery, where the EZ is not resected at all would result in a 0 effect size, or even possibly negative effect size difference between pre and post resection sessions. If a biomarker can detect the presence of the EZ in the network, then one expects it to modulate depending on if the EZ is successfully removed. 91

Figure 4-3 Neural product fragility of complete, partial and incomplete in-silico resections of the EZ (A) Neural fragility heatmap of a successful resection of the underlying EZ. The heatmap shows two concatenated sessions: the pre-resection iEEG and post-resection iEEG. The white region represents the channels that were in the resected regions for the post-resection iEEG simulation. **(B)** Neural fragility of a partially successful resection, where one epileptic region was resected, but another

one was left in. Values in the post-resection period still go down, but relative to panel (a), they are slightly higher. (C) Neural fragility of a completely failed resection, where an incorrect brain region was removed. There is qualitatively very little difference with respect to the pre-resection session. The turbo colormap is used in these heatmaps a-c. (D) A summary effect size difference between pre and post resection fragility values for the three resective scenarios from a-c. Each dot represents the Cohens D effect size computed on a bootstrap sample from pre and post resection heatmap. The successful resections have an improvement in overall network fragility (positive Cohen's D), while the failed resection shows essentially no effect difference. The Cohen's D effect size of successful, partial, and incomplete resections were 0.761 ± 0.322 (PValue of $4.16e-7$), 0.542 ± 0.272 (PValue of $2.19e-5$) and 0.025 ± 0.244 (PValue of $4.12e-3$) respectively (all effect sizes are 95% confidence interval). All PValues were computed using a K-Sample MANOVA test using distance correlation with 0.05 alpha level. For more information on how the bootstrap procedure was implemented, see [Statistical Analysis](#). 92

Figure 4-4 Neural product fragility of successful and failed resections in DRE patients at Sick Children Hospital (A) Resected brain photograph (top) of subject E1 from HSC with Engel III outcome. The heatmap (bottom) shows neural fragility of the pre and post-resection iEEG for a patient with failed resection. The heatmaps show two concatenated sessions: the pre-resection iEEG and post-resection iEEG. Values in the

post-resection period go up. **(B)** Resected brain photograph (top) of subject E3 from HSC with Engel I outcome. The heatmap (bottom) shows neural fragility heatmap of the pre and post-resection iEEG for a patient with successful resection. The heatmap shows fragility goes down in the post-resection period. The white region represents the channels that were in the resected regions for the post-resection iEEG simulation, or disconnected due to surgical necessity. The turbo colormap is used in these heatmaps. On the heatmaps' y-axis, are channel labels, with red channel labels annotated as part of the clinical EZ hypothesis. Note that not all channels are annotated, as some are discarded due to poor recording quality (more information in ??). In addition, depth electrodes are not visualized as they are all removed as part of the surgical procedure. We analyzed the raw iEEG under a monopolar reference. 93

Figure 4-5 Neural fragility of pre vs post resection effect size differences **(A)** A summary effect size difference between pre and post resection fragility values for the six patients. Each dot represents the Cohens D effect size computed on a bootstrap sample from pre and post resection heatmap. The successful resections have an improvement in overall network fragility (positive Cohen's D), while the failed resection shows an actual increase in overall network fragility. **(B)** Showing the distribution of pvalues computed from the same bootstrap samples in (a), that are computed using a K-Sample MANOVA test with alpha level of 0.05. For more information on how the bootstrap procedure was implemented, see [Statistical Analysis](#). **(C)** A

summary effect size difference between pre and post resection HFO rate values for the six patients. Each dot represents the Cohens D effect size computed on a bootstrap sample from pre and post resection session. A positive effect size indicates that there was a decrease in the HFO rates. HFOs were computed using the RMS detector, described in [Time Frequency Representation Analysis](#). **(D)** Corresponding pvalues computed over bootstrap samples of the HFO rates using a Wilcoxon rank-sum test. The graph is displayed on a log-scale on the y-axis. . . . 94

Figure 4-6 Product neural fragility heatmaps using common average referencing (A) Subject E1 with common average reference and **(B)** subject E3 with common average reference. This is the same heatmaps over the same period of data as Figure 4-4, but using a different reference on the data. . . . 95

Figure 4-7 Column perturbation neural fragility heatmaps using common average referencing (A) Subject E1 with common average reference and **(B)** subject E3 with common average reference. This is the same heatmaps over the same period of data as Figure 4-4, but using a different reference on the data. 95

Figure 4-8 Pre vs post resection effect size plots of power in frequency bands (a)-(f) Are delta, theta, alpha, beta, gamma, and highgamma frequency bands respectively. For full details on computing the frequency band power heatmaps, see Methods Section. For examples of the time-frequency heatmaps for all subjects and all frequency bands computed, see Supplementary files. . . . 96

Figure I-1 Distributions of the 91 patient dataset based on a variety of

clinical factors, such as gender **(a)**, handedness **(b)**, clinical complexity **(c)**, and Engel class **(d)**. The plots show distributions over the 91 patients used in analysis. 121

Figure I-2 Neural fragility correlation against non-epileptic clinical covariates - Fragility success probabilities (denoted as "Confidence Statistic" in y-axes) split by clinical factors, such as handedness **(a)**, gender **(b)**, ethnicity **(c)** and age at surgery **(d)**. Not all patients had data for each of these categories, so the subset of available data was used. Note the sample sizes vary across different groups shown. For ethnicity, we also had 1 Asian subject, but left it out because the permutation effect size estimation procedure does not work for 1 sample. Effect sizes were estimated using the permutation test and Mann Whitney U test described in ???. The corresponding effect sizes and p-values were (0.1/0.99) for handedness, and (0.12/0.7) for gender. The pvalue was computed using the one-sided Mann-Whitney U test. The slope was negligibly close to 0 for surgery age linear fit. There was no relatively significant trend in the data related to ethnicity. The significant Cohen's D effect size difference is primarily due to the low sample sizes in non-Caucasian ethnicities. The error bars represent 95% confidence interval specified by 2 standard deviations. 122

Chapter 1

Introduction

Epilepsy

Drug-resistant epilepsy and the epileptogenic zone

Over 15 million epilepsy patients worldwide and 1 million in the US suffer from drug-resistant epilepsy (DRE) [1, 2]. DRE is defined as continued seizures despite two trials of appropriately chosen anti-epileptic drugs [3]. DRE patients have an increased risk of sudden death and are frequently hospitalized, burdened by epilepsy-related disabilities, and their cost of care is a significant contributor to the \$16 billion dollars spent annually in the US treating epilepsy patients [4]. Approximately 50% of DRE patients have focal DRE, where specific brain region(s), termed the epileptogenic zone (EZ), is necessary and sufficient for initiating seizures and whose removal (or disconnection) results in complete abolition of seizures [5, 6]. DRE patients may be amenable to surgical treatment via resection or disconnection of the EZ. In general, the EZ encompasses the clinically identified seizure onset zone (SOZ) and early propagation zone (EPZ). The brain regions associated with the *SOZ* demonstrate the earliest electrophysiological changes during a seizure event, and in general precede the clinical onset of seizures; and the EPZ regions are involved at the time of the earliest clinical (semiological) manifestations during a seizure event [7].

The EZ is a theoretical conceptualization of epileptogenicity that essentially con-

stitutes the minimum amount of cortex that needs to be removed to have seizure freedom. There are currently three main differing opinions of what the EZ is (see Fig 1-1). The Penfield and Jasper hypothesis that states only the initial ictal-onset zones are important, 2) the Tailarach and Bancaud conceptualization of an extended EZ that includes both the initial ictal-zone and the regions of seizure propagation and 3) the "large network" hypothesis by Spencer states that focal epilepsy is based on an organization of a neural network in which epileptogenicity is distributed throughout the entire network [6, 8, 9]. In a review by D. Nair in 2003, it seems evidence mainly points to a Penfield/Jasper hypothesis [10]. There is no convincing neurophysiological evidence to suggest that all regions of a neural network are important in the generation and maintenance of seizures. There is also little evidence to suggest that "early" seizure spread zones must be resected for seizure freedom.

Due to the lack of a prospective and agreed upon definition of the EZ, localizing the EZ is an ill-posed task. It is impossible to identify despite multimodal pre-operative assessments. The definition requires one to resect brain tissue and then verify that a patient is seizure-free to be certain that the EZ was correctly identified. In cases of seizure-freedom, it is impossible to be certain whether a smaller resection may have achieved similar outcomes. Clinicians typically have to wait 6-12 months (or more), to obtain accurate outcome measurements of a surgical resection in terms of an Engel score, or ILAE classification [11, 12].

Diagnosing epilepsy

Before discussing how we might approach localization of the EZ, we first review how general epilepsy is diagnosed in the first place. A person is considered to have epilepsy when two or more unprovoked seizures occur that can't be explained by a medical condition such as fever or substance withdrawal [13, 14]. It can be characterized by one or more seizures with a relatively high recurrence risk (i.e., 60% or greater likelihood)

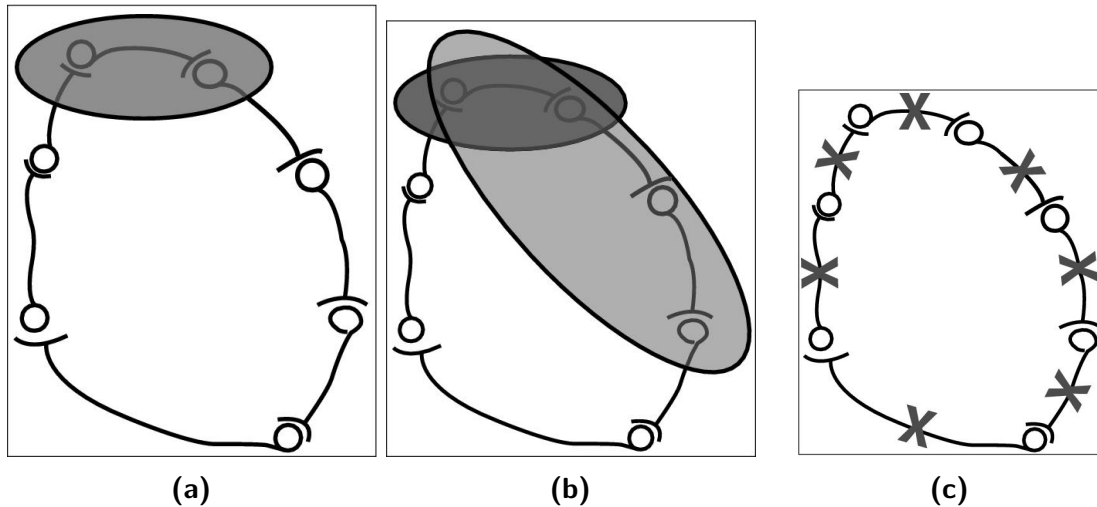


Figure 1-1. Different theories of the epileptogenic zone - (A) Shows Penfield-Jasper theory, where the EZ is contained only in the initial onset zones.(B) shows Tailarach-Bancaud theory, where they emphasize the extended EZ that includes the initial onset zone as well as the regions of seizure propagation. And (C) shows the Spencer theory of the EZ, where epileptogenicity is spread throughout the neural network.

[15]. Diagnosis is carried out in epilepsy monitoring units (EMUs) where routine electroencephalogram (EEG) are used to assist in classification of seizure type(s) and identification of epileptiform abnormalities [15]. However, challenges remain because there is no explicit biomarker for epilepsy. Blood tests do not contribute to the diagnosis of any patient in prospective studies [16]. Thus, the diagnosis is largely clinical and limited by observations. This presents with tremendous difficulties as continuous video EEG monitoring is not feasible when the patient is not in the hospital. Patient self-reporting seizures has been documented to be as low as 50% of the actual occurrence rate [17].

Drug treatment paradigms

The first line of treatment for any epilepsy patient is anti-epileptic drugs (AEDs). There are many kinds of seizures, each with characteristic behavioral changes and electrophysiological disturbances that can usually be detected in scalp electroencephalographic (EEG) recordings. Having a single seizure does not necessarily mean

that a person has epilepsy. Thus it is important to understand the types of seizures for clinicians to prescribe the correct course of AEDs. There are three main types of seizures: partial, generalized, and unclassified [7, 14]. Once a clinician understands the etiology and possible pathology of the patient's epilepsy, then they will make a decision to prescribe AEDs. AED therapy, the treatment for most patients, has four goals: i) to eliminate seizures or reduce their frequency to the maximum degree possible, ii) to evade the adverse effects associated with long-term treatment, and iii) to aid patients in maintaining or restoring their usual psychosocial and vocational activities, and iv) in maintaining a normal lifestyle [14, 18, 19]. Pharmacotherapy however, carries its own risks, with 30% having adverse affects after initial treatment [14].

Surgical treatment paradigms

The focus of this thesis is on guiding surgical treatments. DRE patients are candidates for surgical treatment when they have focal epilepsy, seizures originating from one or few regions of the brain (see Figure 1-2). Successful surgical and neuromodulatory treatments can stop seizures altogether or allow them to be controlled with medications [20], but outcomes for both treatments critically depend on accurate localization of the EZ.

Localizing the EZ is an ill-posed task as it is impossible to identify despite multimodal pre-operative assessments. The common definition requires one to resect brain tissue and then verify that a patient is seizure-free to be certain that the EZ was correctly identified [5]. In cases of seizure-freedom, it is impossible to be certain whether a smaller resection may have achieved similar outcomes. Clinicians typically have to wait 6-12 months (or more), to obtain accurate outcome measurements of a surgical resection in terms of an Engel score, or ILAE classification [11, 12]. If seizures reoccur, re-operations have increased risk of permanent postoperative neurological deficits [21], health-care costs are 32% higher than in patients with successful first-time

surgeries [22], and the delay in surgery may lead to a more widespread seizure network and lesser likelihood of surgical success [23].

When localizing the EZ, the focus is typically on identifying the SOZ, the brain regions that initiate seizures, and the EPZ, the regions associated with early propagation of the seizure activity. This requires observation of the seizures (see Figure ??). As a result, there are lengthy hospital stays and increased risks of complications [24, 25]. Interictal (periods without seizures) localization typically relies on visual identification of "epileptic signatures", such as beta-buzz, high-frequency oscillations, or interictal spiking [26–28]. This requires clinicians to visually inspect intracranial EEG (iEEG) data where they attempt to identify abnormalities in the iEEG channels that may correlate to the *SOZ*. Unfortunately, this task is challenging to even the most experienced clinicians because epilepsy is fundamentally a network disease, which cannot be entirely defined by the current methods of localization. Due to imprecise EZ localization, healthy neural tissue may be included within resection margins potentially resulting in avoidable neurological deficit [29–32]. Furthermore, surgical resection may yield poor outcomes in the most challenging cases with success rates varying between 30-70% [33].

Computationally defining the epileptogenic zone

Prior methods in computational localization of the EZ

Unfortunately, even the most experienced clinicians are challenged in localizing the EZ because epilepsy is fundamentally a network disease, which cannot be entirely defined by the current methods of localization. Thus, there is a great need for developing robust, replicable and validated computational tools that can assist in EZ localization. Prior attempts at performing computational localization of the EZ, can be bucketed into three different categories: i) univariate signal processing methods, ii) static

connectivity methods and iii) computational modeling.

Univariate signal processing methods typically look at spectral power of a single EEG electrode. These typically model the data as a Fourier series, possibly over sliding windows, to estimate the frequency content of the signal, and then correlate this back to the EZ using retrospective data. Many entail investigations of the spectral power in each iEEG channel including high frequency oscillations [34–40], but these approaches do not consider network properties of the brain because they treat each EEG channel independently.

High frequency oscillations (HFOs) are a specific type of EEG metric that epilepsy researchers have been interested in the last two decades. A google scholar search using the keywords: "localization of seizure onset zone epilepsy intracranial EEG" produces over 24,000 results. This is striking considering no computational tools to assist in SOZ localization are in the clinical workflow today. The majority of proposed features lack consistency in finding objective iEEG quantities that correlate to clinically annotated SOZ because they fail to capture internal properties of the iEEG network which are critical to understand when localizing the SOZ. Proposed algorithms either (i) compute EEG features from individual channels (e.g. spectral power in a given frequency band), thus ignoring dependencies between channels [40, 41] to name a few, or they (ii) apply network-based measures to capture pairwise dependencies in the EEG window of interest [42, 43]. Specifically, correlation or coherence between each pair of EEG channels is computed and organized into an adjacency matrix, on which summary statistics are derived including degree distribution and variants of centrality [42–46]. Such network-based measures are not based on well formulated hypotheses of the role of the epileptic tissue in the iEEG network, and many different networks (adjacency matrices) can have identical summary statistics resulting in ambiguous interpretations of such measures [47].

A popular EEG feature that has been proposed as an iEEG marker of the SOZ and

reported in over 1000 published studies is High-frequency oscillations (HFOs) ([48–51] to name a few). HFOs are spontaneous events occurring on individual EEG channels that distinctively stand out from the background signal and are divided into three categories: ripples (80–250 Hz), fast ripples (250–500 Hz), and very-fast ripples (>500 Hz) [52]. Retrospective studies suggested that resecting brain regions with high rates of HFOs may lead to good post-surgical outcome (e.g., [53, 54]). Although they found significant effects for resected areas that either presented a high number of ripples or fast ripples, effect sizes were small and only a few studies fulfilled their selection criteria [54]. Furthermore, several studies have also questioned the reproducibility and reliability of HFOs as a marker [49, 53, 55]. In addition, there are also physiologic, non-epileptic HFOs, which poses a challenge, as disentangling them from pathological HFOs is still an unsolved issue [56].

Similar inconclusive results hold in completed prospective studies of HFOs. In 2017, an updated Cochrane review [27] investigated the clinical value of HFOs regarding decision making in epilepsy surgery. They identified only two prospective studies at the time and concluded that there is not enough evidence so far to allow for any reliable conclusions regarding the clinical value of HFOs as a marker for the SOZ. Today, five clinical trials are listed as using HFOs for surgical planning on *clinicaltrials.gov* as either recruiting, enrolling by invitation, or active and not enrolling and none have reported results. The fundamental limitation of the aforementioned studies lies in the fact that they approach the SOZ EEG marker discovery process as a signal processing and pattern recognition problem, concentrating on processing EEG observations to find events of interest (e.g. HFOs) as opposed to understanding how the observations were generated in the first place and how specific internal network properties can trigger seizures.

Others have proposed graph-based analysis of iEEG [45, 46, 57–61], but these approaches fail to identify internal network properties that cause seizures to occur in

the first place. These methods typically define a bivariate connectivity function that takes two signals, and outputs a metric of connectivity (e.g. Pearson Correlation). This bivariate connectivity function then can be applied to all pairs of EEG signals observed, resulting in a connectivity matrix. Then a thresholding step is typically applied to the connectivity matrix to zero any values less than some threshold, while any values above the threshold are turned to one. This results in a non-weighted graph. Moreover, if the bivariate connectivity function is symmetric, then the result is a non-weighted symmetric graph. Afterwards, researchers typically apply a series of different graph metrics, such as degree, centrality, shortest-path and more, which are then fed into a machine learning classifier to predict whether a channel is epileptic or not [43, 62]. However, without including the thresholding step in a cross-validation step, it is possible that many results are spurious correlations [63].

Another class of attempts at localizing the EZ stem from computational modeling. Researchers posit models that describe the onset of seizures, phenomenological evolution of seizures and other related epilepsy phenomena [64–68]. These models are then integrated into the Virtual Brain (TVB) neuroinformatics platform, which combines patient structural imaging data (e.g. T1 MRI, DTI) with clinical sEEG implantations and clinical EZ hypotheses to generate realistic simulated data [69]. From this virtual cohort of simulated data, derived from realistic patient structural connectomes, researchers have attempted to invert the models using Bayesian inference to then estimate the actual EZ [70]. However, these methods generally can be slow to compute, and also difficult to invert to the high-dimensionality. Thus, there is a need to develop robust, efficient and networked dynamical metrics of EEG to assist in EZ localization.

Aims and Hypotheses of This Thesis

There are currently three invasive treatments for DRE: i) surgical resection, ii) laser ablation, or iii) stimulation of the EZ. However, treatment success rates vary between 30-70%. Currently, clinicians face a two-tiered problem in localizing the EZ: The first problem comes from non-invasive monitoring of the patient, which involves analyzing scalp electroencephalography (EEG), MRI and PET scans along with neuropsychological evaluations. When patients have visible lesions on their MRI scans, the surgical outcome rates reach 70%. However, if the MRI scans look normal, then clinicians must resort to invasive monitoring where electrodes are implanted into the brain in order to localize the EZ. Clinicians analyze the scalp EEG to determine the optimal region (i.e., the region that most likely covers the EZ) to implant intracranial EEG (iEEG) electrodes. The second problem clinicians face is to identify the EZ by visual inspection of single-channel EEG recordings of seizure events over the course of multiple days to weeks. In these patients, despite large brain regions being removed, surgical success rates vary between 30%-50% [71–76].

Such disappointing outcomes are often due to imprecise and/or inaccurate localization of the EZ, which stems from the fact that epilepsy is fundamentally a network-based disease that requires analysis of the EEG recordings as a *network*. One must inspect how multiple channels (i.e., brain regions) interact dynamically. However, simultaneously interpreting network effects from more than 80 iEEG channels is difficult and prone to error. Furthermore, accurate EZ localization requires actually covering the EZ with the invasive electrodes, which is driven by scalp EEG data that are noisy and lack spatial resolution. There is a clear need to bring in data analytics and computational approaches to address these challenges. Current computational studies have the following three shortcomings. First, the size of the datasets analyzed are small; they typically come from one epilepsy center, and only

analyze a single recording modality on a homogenous population with the same clinical etiology. Second, current methods can have high computational cost, and thus not readily usable in a clinical setting. Third, many methods use black-box machine learning algorithms that are difficult to interpret by clinicians.

My goal is to develop a computational tool that assists in accurately localizing the EZ in DRE patients - This tool and algorithm will be validated on a multi-center, multi-modality and multi-etiology dataset. I will apply fragility theory, [77], to linear time-varying network (LTVN) models constructed from iEEG data. Fragility of a node in a network is defined as the minimum-norm perturbation that can be applied to the node's connectivity that destabilizes the entire network (i.e. causes a seizure). More discussion will follow in 2. Application of the theory to a LTVN model, will generate a fragility map that describes fragility of each channel over time. The most fragile network nodes will correspond to the clinically hypothesized EZ for patients who had successful surgical treatment, whereas fragile nodes will disagree with the clinical hypothesis in failed surgical outcomes. Development of the tool is broken down into the following three aims:

Aim 1: Develop an Epilepsy EEG Data Platform

In this aim, I will collect, aggregate and preprocess iEEG datasets of epilepsy patients from Cleveland Clinic (CCLinic), National Institute of Health (NIH), Johns Hopkins Hospital (JHH), University of Maryland Medical Center (UMMC) and University of Miami Florida (UMF). Each dataset will have clinical annotations, implantation regions, surgical outcomes, and the clinical hypotheses. In addition, we will label each patient with an additional metric, clinical complexity, which is reflective of the difficulty of the data to localize the EZ. This will result in a large sample size, multi-modal and multi-etiology dataset of the DRE population that will be used to develop my tool. *I hypothesize that stratification of patients based on different clinical*

factors will result in varying degrees of agreement between the model and clinicians. Moreover, I will convert the dataset to the Brain Imaging Data Structure (BIDS) format and make it openly accessible [78].

Aim 2: Develop and Test Localization Model on iEEG Data

In this aim, I will develop and test a fast algorithm for computing a LTVN model from each EEG dataset covering a seizure event. Then, I will apply fragility theory to the LTVN model and compute a fragility map for each seizure event. To determine the effective information in differentiating the EZ, I will compare the clinically hypothesized EZ (CEZ) with the rest of the network’s fragility (CEZ^C) by predicting surgical outcome of each patient and measure the sensitivity, specificity and accuracy of the tool. *I hypothesize that the degree of agreement will be higher in patients who had successful surgical outcomes and lower in patients who had failed surgical outcomes. In addition, I hypothesize that neural fragility will produce a better feature representation for predicting surgical outcome than traditional univariate and static connectivity measures.*

Aim 3: Validate Localization Model on Intraoperative and Postoperative Data

In this aim, I will apply fragility theory to simulated iEEG data from the Virtual Brain (TVB) and interoperative and postoperative iEEG data from the Hospital for Sick Children (HSC). I will evaluate neural fragility as a correlate of surgical outcome using pre and post resection iEEG interictal recordings of the same subjects. *We hypothesize that neural fragility of the brain network will decrease in cases of successful surgical resection. In iEEG data, neural fragility will modulate with respect to the surgical outcome, increasing, or staying the same after resection in the context of residual epileptic tissue, and decreasing after resection if the procedure was successful.*

Comprehensive Evaluation For Drug Resistant Epilepsy And Pathways To Nonpharmacologic Treatments

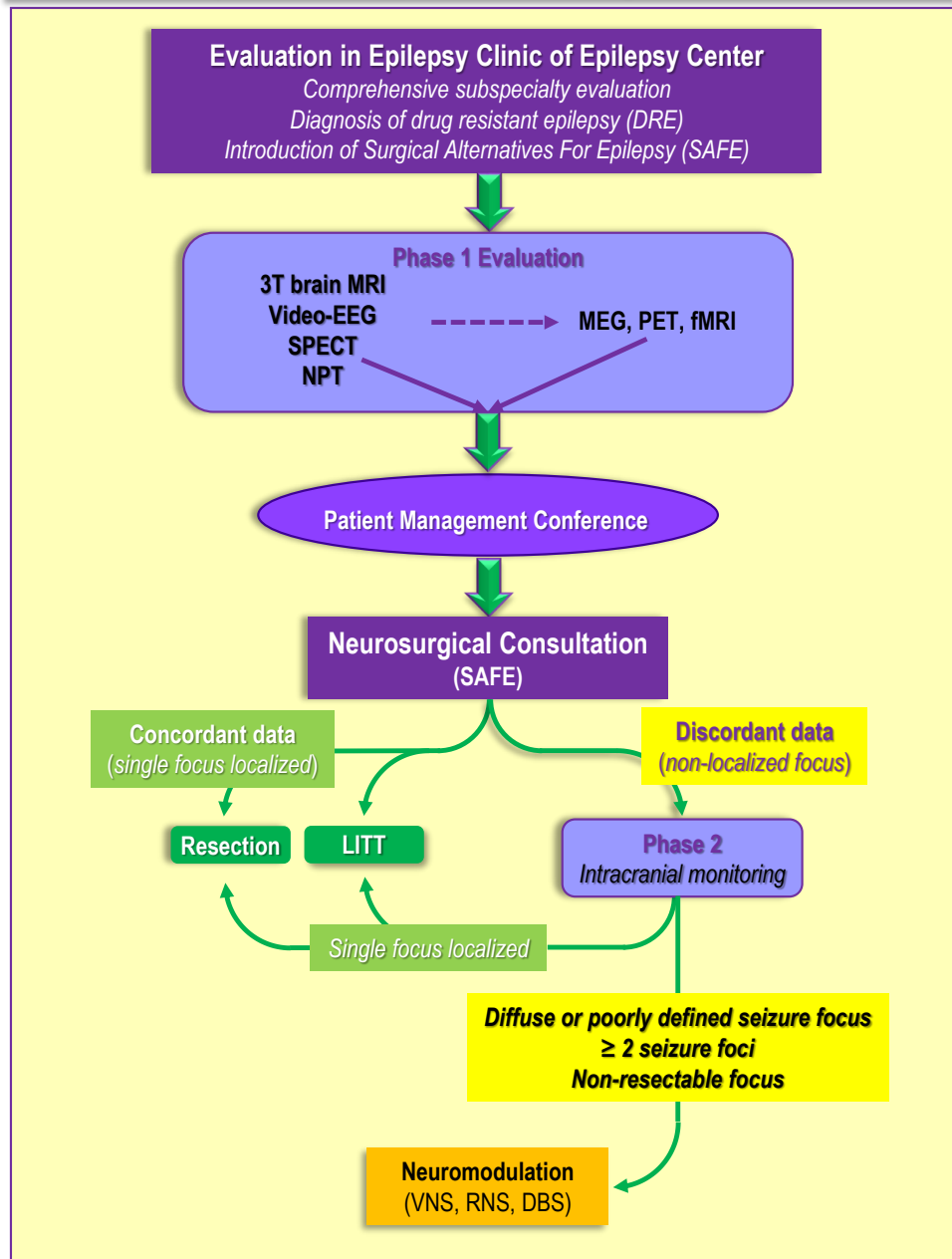


Figure 1-2. Pathways to epilepsy surgery - A flow chart of how an epilepsy patient will arrive at surgical treatment.

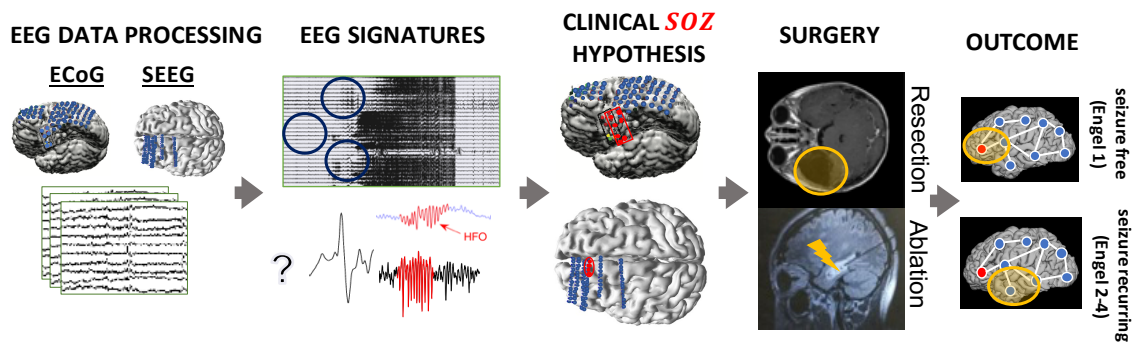


Figure 1-3. Clinical process of EZ localization - A schematic of what occurs clinically to localize the EZ by i) starting with ECoG, or sEEG implantations, ii) analyzing EEG signatures, then iii) formulating a clinical hypothesis about where the SOZ is, iv) performing surgery at the proposed brain regions and finally v) measuring outcome of the surgery with at least 12 months of follow up.

Chapter 2

Neural fragility - a dynamical networked-system representation of the epileptic network

Abnormal connections across several channels may constitute a more effective marker of the *SOZ* [79]. Localization thus lends itself to a data-driven network-based computational approach and several electroencephalogram (EEG) algorithms have been proposed to localize the *SOZ* from recordings. Many entail investigations of the spectral power in each iEEG channel including high frequency oscillations [48], but these approaches do not consider network properties of the brain because they treat each EEG channel independently. Others have proposed graph-based analysis of iEEG [43–46, 59, 80], but these approaches fail to identify internal network properties that cause seizures to occur in the first place.

We propose an EEG marker of the *SOZ*, neural fragility (conceptually described in Figure 2-1 and quantitatively in Figure 2-2). To create the fragility marker, we first build a personalized dynamic model of the brain network from observed iEEG signals (top row Figure 2-2). The generative model can accurately reconstruct the patient’s iEEG recordings [81, 82]. We then calculate neural fragility which measures the degree network nodes are imbalanced, i.e., small impulse perturbations on the network and thus can trigger seizures (see Figure 2-1) [77].

In order to put neural fragility into context, we first review relevant linear systems theory, system identification and matrix perturbations.

Linear systems

As some preliminaries, we first review notation. We say that $A \in M_n$ is a $n \times n$ matrix; we only consider real matrices in this work. We denote, M_n^1 as the space of $n \times n$ matrices that have rank of one. Then we say $C_k(\Gamma)$ is the space of matrices with all zeros except for one column, with $\Gamma \in \mathbb{R}^n$ occupying the k th row. Then $R_k(\Gamma)$ is the space of matrices with all zeros except for one row, with Γ occupying the k th row. We say that $Res(z)$ is resolvent matrix parametrized by $z \mapsto (A - zI)^{-1}$ for a given A matrix. It is defined for $z \notin \sigma(A)$.

Consider a discrete time linear system with state evolution equation as equation 2.1 with state vector $\mathbf{x}(t) \in \mathbf{R}^N$, and state transition matrix $\mathbf{A} \in \mathbf{R}^{N \times N}$ with eigenvalues $\lambda_{1...N} \in \mathbf{C}$ where $|\lambda_1| \geq \dots \geq |\lambda_N|$.

$$\mathbf{x}(t + 1) = \mathbf{A}\mathbf{x}(t). \tag{2.1}$$

The state transition matrix can be viewed as an adjacency matrix representation of the functional connectivity of a network of N nodes, whose dynamics are linear and captured in the evolution of the state vector. The elements in the state vector are some metric of the activity of each node. Element A_{ij} indicates how the activity of node j , $x_j(t)$, affects the future activity of node i , $x_i(t + 1)$. Element A_{ii} is an autofeedback term, representing a first-order approximation to the internal dynamics of node i . More generally, the i^{th} row of \mathbf{A} dictates the network's cumulative functional effect on node i , while the j^{th} column captures the functional effect of the activity of node j on the entire network.

From linear systems theory, the system is said to be asymptotically stable about a

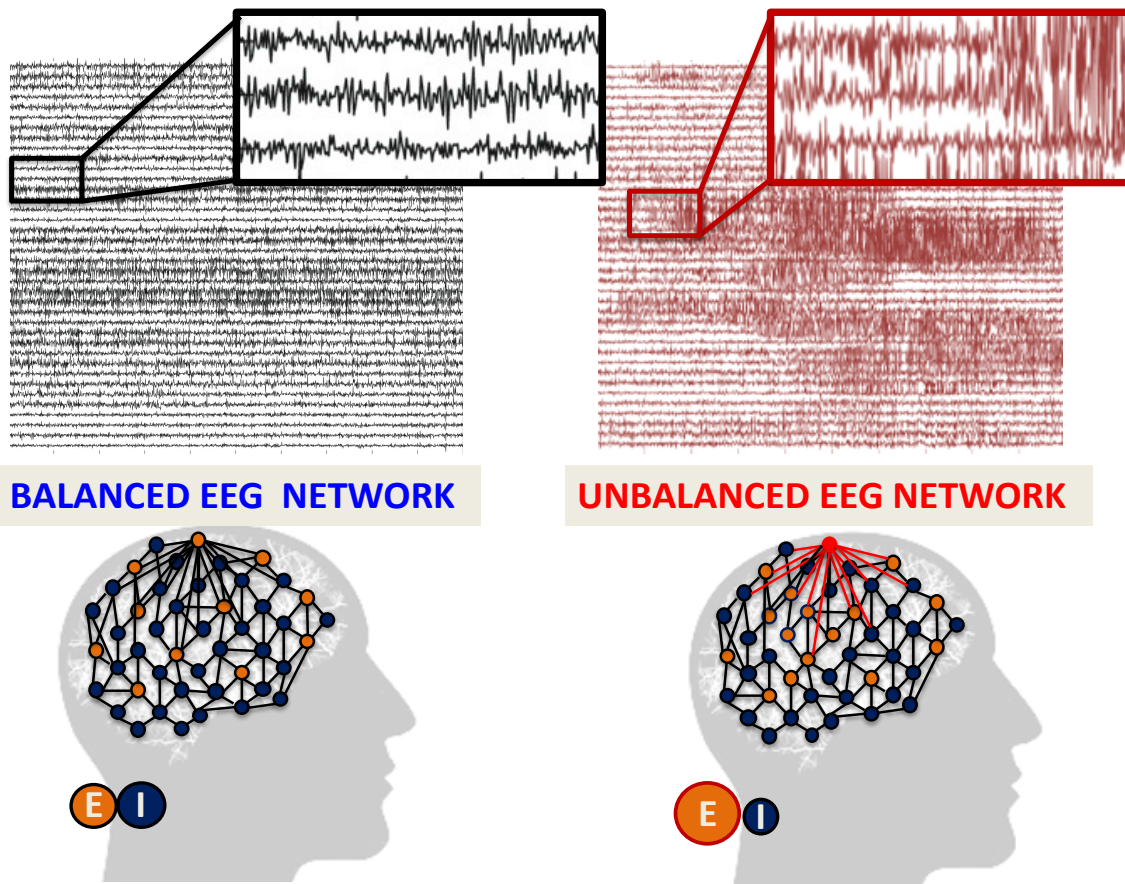


Figure 2-1. Intuition of neural fragility - unbalanced and balanced networks
(Top) iEEG traces in between seizures (left) and during a seizure (right). **(Bottom)** network schematic showing change in connectivity (right) in fragile node that causes seizure. Describes qualitatively the concept of neural fragility in the context of a dynamical iEEG network, with nodes representing excitatory (E) and inhibitory (I) population of neurons. From a dynamical systems point of view, such imbalance arises from a few fragile nodes causing instability of the network in the form of over-excitation, or under-inhibition. We define fragility of a network node to be the minimum-energy perturbation applied to the node's weights on its neighbors before rendering the network unstable [77, 81]. In systems theory, stable systems return to a baseline condition when a node is perturbed. In contrast, unstable systems can oscillate and grow when a node is perturbed. In the context of epilepsy, a fragile node is one that requires a smaller perturbation to lead to seizure activity. Fragility theory can be modeled in the context of linear dynamical systems: $x(t+1) = Ax(t)$. Perturbing the columns of the A matrix will alter dynamical connections of a particular node (i.e. that column) on its neighbors, resulting in an imbalanced network.

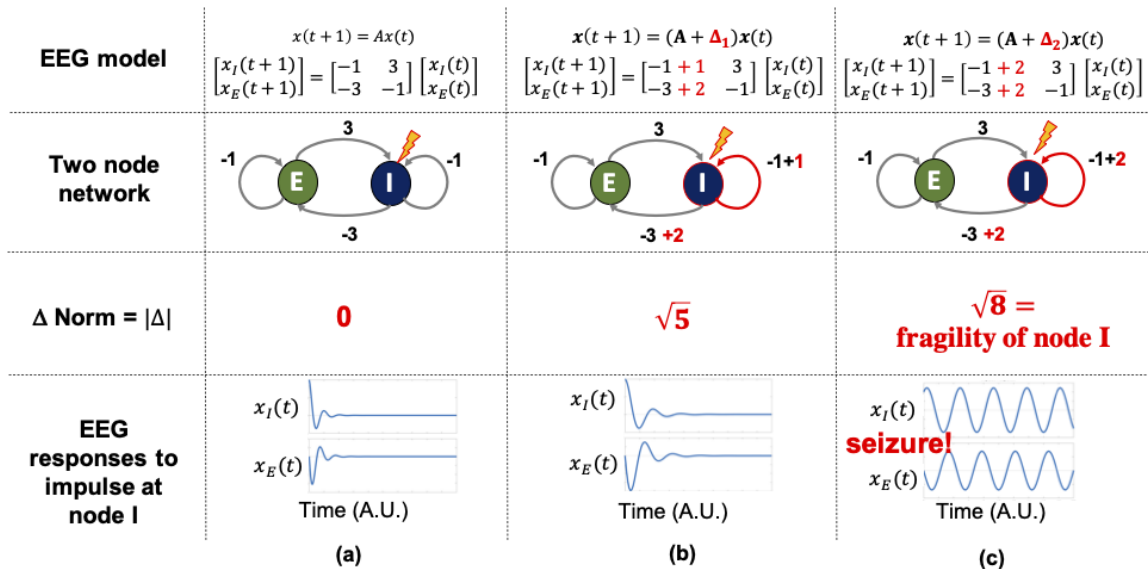


Figure 2-2. Neural fragility in a 2-node network To build quantitative intuition on what neural fragility means in the context of a dynamical iEEG system, we construct a 2-node EEG network example with an excitatory (E) and inhibitory (I) population of neurons. For a qualitative description, see Figure 2-1. $x_I(t)$ and $x_E(t)$ are the EEG activity of the I and E neuronal population respectively. 'A' is a linear network model quantifying how each population affects the rest over time. Δ (i.e. the fragility), is the amount of change added to a node's connections. The fragility of the node is quantified as the minimal amount of change necessary to cause seizure-like phenomena. **(a)** shows a stable network without a perturbation added, such that the network responses due to an impulse at I result in a transient that reverts to baseline. **(b)** shows a perturbation added, but the network is still stable with a slightly larger transient when an impulse is applied to node I . Then **(c)** shows enough of a perturbation is added, such that the network becomes unstable; an impulse applied at node I results in oscillatory activity that does not quickly return to baseline. The magnitude of the Δ added in **(c)** is the fragility of node I (i.e. $\sqrt{8}$).

fixed point, $\bar{\mathbf{x}}$, if $\mathbf{x}(t)$ converges to $\bar{\mathbf{x}}$ as $t \rightarrow \infty$ for all initial conditions. This implies that the activity of the nodes remains at a baseline value and responds transiently to external inputs before recovering. In terms of the matrix representation, stability is equivalent to the eigenvalues of \mathbf{A} being inside the unit disk in the complex plane, i.e., $|\lambda_i| < 1$ for all $i = 1, 2, \dots, N$.

This is more evident when equation 2.1 is cast in modal form as shown in equation 2.2 where $c_i \in \mathbf{C}$ are set according to initial conditions and $\mathbf{v}_i \in \mathbf{C}^N$ are the eigenvectors of \mathbf{A} corresponding to λ_i . Assume the system has already been transformed so the fixed point is at the origin ($\bar{\mathbf{x}} = \mathbf{0}$) and that there are n distinct eigenvalues of \mathbf{A} . Then the solution to the linear system can be written as:

$$\mathbf{x}(t) = \sum_{i=1}^N c_i |\lambda_i|^t \mathbf{v}_i \quad (2.2)$$

If $|\lambda_1| < 1$, the real components of the other eigenvalues are also negative by virtue of their ordering, and all the terms in equation 2.2 decay so that the system settles to its baseline activity (transformed to be at the origin). If $\lambda_1 = 0$, then the other eigenvalues have negative real components and their corresponding terms vanish over time, so the state settles somewhere along the first eigenvector based on initial conditions: $\mathbf{x}(t) \rightarrow c_1 \mathbf{v}_1$. Therefore, the network gets stuck in some pattern of activity instead of decaying to its baseline. If the elements in the state vector represent spiking rates, this may be analogous to tonic spiking or silenced neurons. Finally, if $\lambda_{1,2} = \pm j\omega$, then for large t , the activity of each node oscillates around its baseline without ever decaying. This may be a suitable representation for spiking rates entrained to an oscillation.

A linear system becomes unstable if there is a change to the state matrix so that the stability conditions on the eigenvalues are no longer met. This change can be

modeled as an additive perturbation, Δ , to the state matrix so that $\mathbf{A} + \Delta$ replaces \mathbf{A} in the state equation, equation 2.1, to give equation 2.3.

$$\mathbf{x}(t) = (\mathbf{A} + \Delta)\mathbf{x}(t) \quad (2.3)$$

This notion of instability can be adopted for networks whose dynamics are linear or can be approximated as linear in some regime. For such networks, the eigenvalues of the functional connectivity matrix determine the stability properties.

A review of matrix perturbations

First, we restate the theorem of [77, 83], which derives how to compute neural fragility given a linear dynamical system, represented by the matrix, A . We say $\lambda \in \sigma(A)$ is an eigenvalue in the spectrum of A and has a corresponding eigenvector, $v \in \mathbb{R}^n$ such that: $Av = \lambda v$.

Theorem (Computation of neural fragility from linear system). *Suppose $A \in M_n$ represents the state matrix of a linear dynamical system. Assume that $r \in \mathbb{C}$ is a number (possibly complex) that is not an eigenvalue of A . Then, for all $k = 1, \dots, n$, there exists a rank-one matrix, $\Delta \in R_k(\Gamma)$, such that:*

$$r \in \sigma(A + \Delta)$$

and with minimum 2-norm. Moreover, Δ can be solved analytically by the equation:

$$\widehat{\Delta} = \mathbf{B}^T(\mathbf{B}\mathbf{B}^T)^{-1}\mathbf{b}]e_{\mathbf{k}}^T \quad (2.4)$$

where

$$\mathbf{B}(r, k) = \begin{bmatrix} \text{Im}\{e_k^T(\mathbf{A} - r\mathbf{I})^{-T}\} \\ \text{Re}\{e_k^T(\mathbf{A} - r\mathbf{I})^{-T}\} \end{bmatrix} \quad (2.5)$$

$$\mathbf{b} = \begin{bmatrix} 0 \\ -1 \end{bmatrix} \quad (2.6)$$

k is the index at which the perturbation is computed, $e_k \in \mathbb{R}^n$ is a unit vector with the one at the k th position.

Moreover, when $r \in \mathbb{R}$, then:

$$\Gamma = -\frac{(rI - A)^{-1}e_k}{e_k^T(rI - A)^{-T}(rI - A)^{-1}e_k}$$

which is the $n \times 1$ vector that perturbs the k th row of A .

This theorem differs slightly from [77] because we use a discrete time model, but the proof follows as in [77]. Next, we restate a few key results that will be useful for proving various bounds in the next section.

We remind the readers of what is known as the Neumann Series, which generalizes the geometric series of real numbers.

Definition 2.0.1 (Neumann Series). A Neumann series of a matrix, T is an infinite series:

$$\sum_{k=0}^{\infty} T^k$$

We have the following theorem that utilizes the definition of the Neumann Series.

Lemma. For any matrix, $A \in M_n(\mathbf{C})$, with $\|A\| < 1$. The matrix, $(I - A)$ is invertible and

$$\|(I - A)^{-1}\| \leq \frac{1}{1 - \|A\|}$$

Proof. We use the matrix version of the Taylor series to expand $(I - A)^{-1}$ for $\|A\| < 1$, such that we get the convergent series:

$$(I - A)^{-1} = I + A + A^2 + A^3 + \dots$$

Thus, taking the norm of both sides:

$$\|(I - A)^{-1}\| = \|I + A + A^2 + \dots\| \tag{2.7}$$

$$\leq \|I\| + \|A\| + \|A^2\| + \dots \quad (\text{Sub-additivity of norms}) \tag{2.8}$$

$$= \frac{1}{1 - \|A\|} \quad (\text{Geometric series for } \|A\| < 1) \tag{2.9}$$

□

Using this lemma, one has the following bound on the norm of the resolvent.

Lemma. *For any $A \in M_n(\mathbb{C})$ and $z \in \mathbb{C}$, such that $|z| > \|A\|$, then the resolvent $Res(z)$ exists and*

$$\|Res(z)\| \leq \frac{1}{|z| - \|A\|}$$

Proof. Since $|z| > \|A\|$, then $\|\frac{A}{z}\| < 1$, so we can apply the previous lemma on the quantity $\frac{A}{z}$.

$$(I - \frac{A}{z})^{-1} = z(zI - A)^{-1} = (I + A/z + A^2/z^2 + \dots)$$

such that:

$$(zI - A)^{-1} = z^{-1}(I + A/z + A^2/z^2 + \dots)$$

We can take the norm on both sides of this equation and utilize the previous lemma to obtain:

$$\|(zI - A)^{-1}\| \leq \frac{1}{|z|} \frac{1}{1 - \|A/z\|} = \frac{1}{|z| - \|A\|}$$

□

Next we define the notion of relative boundedness with respect to a linear operator.

Definition 2.0.2. Let A and T be matrices with the same domain space, but not necessarily the same range space. Then for a, b non-negative constants, if

$$\|Au\| \leq a\|u\| + b\|Tu\|$$

Then we say A is relatively bounded with respect to T , or A is T -bounded.

In [84], Theorem 1.16 (page 196) states the stability of bounded invertibility, which we will leverage later. It states the following:

Theorem (Stability of bounded invertibility from [84]). *Let A and T be linear operators from $\mathbb{R}^n \rightarrow \mathbb{R}^n$ (i.e. $n \times n$ matrices). Assume that A^{-1} exists and is T -bounded with the constants a, b satisfying the following inequality:*

$$a\|T^{-1}\| + b < 1$$

Then we have the following result: $S = T + A$ is invertible and:

$$\|S^{-1}\| \leq \frac{\|T^{-1}\|}{1 - a\|T^{-1}\| - b}$$

and

$$\|S^{-1}\| \leq \frac{\|T^{-1}\|}{1 - a\|T^{-1}\| - b}$$

Corollary (Stability of bounded invertibility for bounded linear operators). *If A is bounded, and we assume that T is A -bounded with constants $a = \|T\|$ and $b = 0$, $S = T + A$, and $\|A\| < 1/\|T^{-1}\|$, then we have:*

$$\|S^{-1}\| \leq \frac{\|T^{-1}\|}{1 - \|A\|\|T^{-1}\|}$$

and

$$\|S^{-1} - T^{-1}\| \leq \frac{\|A\|\|T^{-1}\|^2}{1 - \|A\|\|T^{-1}\|}$$

Neural fragility - A structured rank-one perturbation

A variety of perturbation matrices in equation 2.3 can push the original network in equation 2.1 into instability. Based on the structure of the perturbation (e.g. $\Delta \in \mathbf{R}^{N \times N}$ or $\Delta \in \text{diag}\{\mathbf{R}^N\}$ as in Figure 2-3A), and which elements are preferentially affected, different perturbation strengths (measured by a matrix norm) are required to cause the perturbed system to become unstable. Network fragility is defined here as the magnitude of the minimum energy perturbation required to push the network to the brink of instability. If a large magnitude perturbation is required, the network is more robust, while small energy perturbations correspond to a fragile network. The elements that are modified by the minimum energy perturbation define the edges of the most fragile subnetwork.

Whole network perturbations or diagonal perturbations will not be considered because they are biologically unlikely. It is improbable that a whole host of functional network connections need to be modified to cause aberrant behavior or that changes in autofeedback occur in different neurons independently and in isolation without affecting functional connectivity in any other way.

$$\begin{array}{c}
\mathbf{A} \\
\left[\begin{array}{ccc} \Gamma_1 & \cdots & 0 \\ \vdots & \ddots & \vdots \\ 0 & \cdots & \Gamma_N \end{array} \right]
\end{array}
\quad
\begin{array}{c}
\mathbf{B} \\
\left[\begin{array}{cccc} \cdots & | & | & | \\ \cdots & \mathbf{0} & \mathbf{\Gamma} & \mathbf{0} \\ \cdots & | & | & | \end{array} \right]
\end{array}
\quad
\begin{array}{c}
\mathbf{C} \\
\left[\begin{array}{ccc} \vdots & & \\ - & \mathbf{0} & - \\ - & \mathbf{\Gamma}^T & - \\ - & \mathbf{0} & - \\ \vdots & & \end{array} \right]
\end{array}$$

Figure 2-3. Three perturbation topologies in $\mathbf{R}^{N \times N}$ - **(A)** Diagonal perturbations only disrupt autofeedback terms. **(B)** Column perturbations have non-zero entries in a single column while **(C)** row perturbations have a single row with non-zero entries.

Network fragility will therefore be derived for row perturbations (see Figure 2-3C) corresponding to changes in the effect of incoming projections to a single neuron or population. Row perturbations may be a plausible perturbation structure to reflect anomalies a neuron or population that affects how it integrates inputs. The column perturbation case can be derived similarly [77].

Next, we reproduce from [77] the structured row perturbation problem formulation and solution for a discrete time linear system.

Theorem (Solving the minimum norm of a structured rank-one perturbation). *Suppose $\mathbf{A} \in \mathbf{R}^{N \times N}$ represents the state transition matrix of a stable linear network. Then the minimum 2-induced norm additive row perturbation, $\widehat{\Delta} \in \Lambda_r = \mathbf{e}_k \mathbf{\Gamma}^T$ and $\mathbf{\Gamma} \in \mathbf{R}^N$, that will destabilize the linear network (or more precisely place an eigenvalue of $\mathbf{A} + \widehat{\Delta}$ at $\lambda = \sigma + j\omega$, $-1 < \omega \leq 1$), is given by*

$$\widehat{\Delta} = \mathbf{e}_{\widehat{k}} \left[\mathbf{B}^T (\mathbf{B}\mathbf{B}^T)^{-1} \mathbf{b} \right]^T \tag{2.10}$$

where

$$\mathbf{B}(\sigma, \omega, \widehat{k}) = \begin{bmatrix} \text{Im} \left\{ \mathbf{e}_{\widehat{k}}^T (\mathbf{A} - (\sigma + j\omega)\mathbf{I})^{-T} \right\} \\ \text{Re} \left\{ \mathbf{e}_{\widehat{k}}^T (\mathbf{A} - (\sigma + j\omega)\mathbf{I})^{-T} \right\} \end{bmatrix} \tag{2.11a}$$

$$\mathbf{b} = \begin{bmatrix} 0 \\ -1 \end{bmatrix}. \tag{2.11b}$$

and \hat{k} is the row where the perturbation is applied. $\mathbf{e}_k \in \mathbf{R}^N$ is the k^{th} elementary basis vector.

Here, I can add orthogonality constraints to the columns, or rows of the matrix perturbation problem.

$$\min_{\Delta \in \Lambda_{c,\omega}} \|\Delta\|_2 \iff \min_{0 < \omega \leq \omega_l, k} \|\Gamma\|_2 \quad \left| \quad \begin{bmatrix} a_i^T(\omega, k) \\ a_r^T(\omega, k) \end{bmatrix} \Gamma = \begin{bmatrix} 0 \\ -1 \end{bmatrix} \Gamma_k \Gamma_k^T = I \quad (2.12)$$

Chapter 3

A Retrospective Study: Neural Fragility as an EEG Marker of the Epileptogenic Zone

To evaluate neural fragility as a marker for the SOZ, we conduct a retrospective study using iEEG data from 91 patients treated across 5 epilepsy centers: Johns Hopkins Hospital (JHH), National Institute of Health (NIH), Cleveland Clinic (CCLinic), University of Maryland Medical Center (UMMC) and Jackson Memorial Hospital of University of Miami (UMF). In the study population, all DRE patients underwent invasive iEEG monitoring followed by surgical resection or laser ablation of the *SOZ* (44 success and 47 failure outcome). We demonstrate that neural fragility is higher/lower in electrode contacts within clinically annotated SOZs for success/failure patients. In addition, we compare fragility of iEEG nodes to 6 frequency-based and 14 graph theoretic features in a 10-fold nested-cross validation experiment. Neural fragility has an area under the curve (AUC) discrimination score of 0.88 +/- 0.064, which is 13% better compared to the next best feature. In addition, it has a high degree of interpretability, which we demonstrate by computing an interpretability ratio suggesting that spatiotemporal heatmaps of neural fragility can be a robust iEEG biomarker of the *SOZ*, seamlessly integrated into the clinical workflow.

Methods

All data were acquired with approval of local Institutional Review Board (IRB) at each clinical institution: UMMC by IRB of the University of Maryland School of Medicine, UMH by University of Miami Human Subject Research Office - Medical Sciences IRB, NIH by the National Institute of Health IRB, JHH by Johns Hopkins IRB and CClinic by Cleveland Clinic Institutional Review Board. Informed consent was given at each clinical center. The acquisition of data for research purposes was completed with no impact on the clinical objectives of the patient stay. Digitized data were stored in an IRB-approved database compliant with Health Insurance Portability and Accountability Act (HIPAA) regulations.

Data collection

iEEG data from 91 DRE patients who underwent intracranial EEG monitoring, which included either electrocorticography (ECoG), or depth electrodes with stereo-EEG (SEEG) were selected from University of Maryland Medical Center (UMMC), University of Miami Jackson Memorial Hospital (UMH), National Institute of Health (NIH), Johns Hopkins Hospital (JHH), and the Cleveland Clinic (CClinic). Patients exhibiting the following criteria were excluded: no seizures recorded, pregnant, sampling rate less than 250 Hz, previous surgeries more than 6 months before, and no surgery performed (possibly from *SOZ* localizations in eloquent areas). We define successful outcomes as seizure free (Engel class I and ILAE scores of 1 and 2) at 12+ months post-op and failure outcomes with seizure recurrence (Engel classes 2-4) [85–88]. Of these 91 patients, 44 experienced successful outcomes and 47 had failed outcomes (age at surgery = 31.52 +/- 12.32 years) with a total of 462 seizures (seizure length = 97.82 +/- 91.32 seconds) and 14703 total number of recording electrodes (159.82 +/- 45.42 per subject). Decisions regarding the need for invasive monitoring and the placement of electrode arrays were made independently of this work and part of routine clinical

care. Data collection and labeling of patients were done retrospectively and thus blind to the authors conducting data analysis (i.e. AL, CH, SVS), but not with respect to the corresponding clinicians. Data analysis were not performed blind to the conditions of the experiments. Sample sizes were determined by attempting to gather as many patients as possible from multiple clinical centers (see Table 1 for summary of all patients gathered). When possible, we sought to have a balance of lesional, temporal, extra-temporal and multi-focal epilepsy patients, along with a relatively proportional number of success and failed epilepsy surgery patients (success = seizure freedom, failure = seizure recurrence). We collected 100 patients and then removed 9 due exclusion criterion. No statistical methods were used to pre-determine sample sizes but our sample sizes are larger than those reported in previous publications [80].

Our clinician team categorized patients by surgical outcome, Engel class and ILAE score. In addition, we categorized patients by their clinical complexity (CC) as follows: (1) lesional, (2) focal temporal, (3) focal extratemporal, and (4) multi-focal (Figure 3-1) [7, 88]. Each of these were categorized based on previous outcome studies that support this increasing level of localization difficulty. Lesional patients have success rates of $\tilde{70}\%$, experiencing the highest rate of surgical success because the lesions identified through MRI are likely to be part of the SOZ [89]. Localization and surgical success are more challenging patients with non-lesional MRI, with average surgical success rates in temporal, extratemporal and multi-focal epilepsy of $\tilde{60}\%$, $\tilde{45}\%$ and $\tilde{30}\%$, respectively [7, 72]. Patients that fit into multiple categories were placed into the more complex category. Next, clinicians identified electrodes that they hypothesized as *SOZ*. In general, this was a subset of the resected region for all patients, unless otherwise noted. The epileptologists define the clinically annotated *SOZ* as the electrodes that participated the earliest in seizures. Every patient’s *SOZ* was labeled by 1-3 trained epileptologists (depending on the center). The corresponding *SOZ* complement that we define, or *SOZ^C*, are the electrodes that are not part of the *SOZ*.

For more detailed information regarding each patient, see Supplemental clinical data summary Excel file and Table 1.

Preprocessing of data

Every dataset was notch filtered at 60 Hz (with a cutoff window of 2 Hz) and bandpass filtered between 0.5 and the Nyquist frequency with a fourth order Butterworth filter. A common average reference was applied to remove any correlated noise. EEG sequences were broken down into sequential windows and the features were computed within each window (see 3 - [Neural fragility of iEEG network](#), [Baseline features - spectral features](#) and [Baseline features - graph analysis of networks](#) for details). Each proposed feature representation produces a value for each electrode for each separate window, and results in a full spatiotemporal heatmap when computed over sequential windows with electrodes on the y-axis, time on the x-axis and feature value on the color axis. In total, we computed 20 different baseline feature representations from the iEEG data: 6 frequency power bands, 7 eigenvector centralities (one for each frequency band coherence connectivity matrix and one for a correlation connectivity matrix), 7 degrees (one for each frequency band coherence connectivity matrix and one for a correlation connectivity matrix). Values at each window of time were normalized across electrodes to values that could range from 0 up to at most 1, to allow for comparison of relative feature value differences across electrodes over time; the higher a normalized feature, the more we hypothesized that electrode was part of the SOZ [81].

Neural fragility of iEEG network

When one observes iEEG data during interictal, or preictal periods, activity recorded from each channel is noisy and hovers around a baseline value. In contrast, when one observes iEEG data during a seizure event, activity (i) grows in amplitude, (ii)

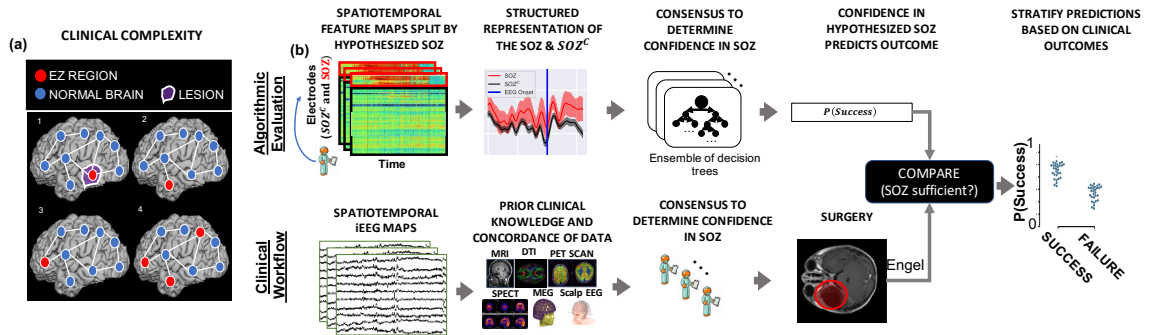


Figure 3-1. Clinical complexity and our experimental paradigm (a) Schematic of the difficulty of different epilepsy etiologies that might arise in DRE patients. Since there is no biomarker for the EZ and it is never observed directly, the network mechanisms that cause seizures are complex. Case clinical complexity ordered by increasing localization difficulty: lesional (1), focal temporal (2), focal extratemporal (3), and multi-focal (4) that are present in the dataset. These four categories simplify the possible epilepsy presentations, but provide a broad categorization of simple to complex cases observed in the clinic. (b) Schematic of our experimental design. (bottom row) Shows a simplified analogous workflow that clinicians take to evaluate their confidence in a proposed *SOZ* localization resulting in a surgery. During invasive monitoring, clinicians identify the *SOZ* from iEEG patterns (e.g. spiking/rhythmic activity). When possible, subsequent surgical resection or laser ablation, generally including the *SOZ* along with a variable extent of additional tissue, is performed. Post-operatively, patients are followed for 12+ months and categorized as either success, or failure, resulting in an Engel or ILAE score. (top row) We evaluate various representations of iEEG in the form of spatiotemporal heatmaps, creating a partitioned summary of the clinically annotated *SOZ* around seizure onset, feed them into a Random Forest classifier and compute a probability of success (i.e. a confidence score) in the clinically hypothesized *SOZ*. The probability was then compared with the actual outcome of patients. These predictions can then be stratified based on clinical covariates, such as the actual surgical outcome. For a feature to be an accurate representation of the underlying epileptic phenomena, the following assumptions are made. As a result of seizure freedom, assume that the clinically hypothesized *SOZ* was sufficient, and the probability of success has a high value. In contrast, if seizures continue, then the *SOZ* was not sufficient and the probability should have a low value.

oscillates, and (iii) spreads in the brain. From a dynamical systems perspective, the iEEG network has switched from a stable (non-seizure) to an unstable (seizure) network. The only difference between the iEEG networks in Figure ?? is the connection strengths representing the dynamical interactions between a few channels, i.e., the *SOZ*. Our conjecture is that small changes in connection strengths at *SOZ* nodes cause an imbalance in inhibitory and excitatory connectivity between brain regions. Either inhibition is decreased and/or excitation is increased; thus, if the *SOZ* is perturbed then over excitation can occur manifesting in a seizure.

To compute fragility heatmaps from iEEG recordings, we first constructed simple linear models as described above and in equation ?. Since each observation, $x \in \mathbb{R}^d$, has dimension d (number of channels), we would like to formulate a least-squares estimation procedure with $n > d$ samples. We choose n to represent a 250 ms iEEG window. We then have the following representation of $X(t) \in \mathbb{R}^{d \times n-1}$:

$$X(t) = \begin{pmatrix} | & | & \cdots & | \\ \mathbf{x}(1) & \mathbf{x}(2) & \cdots & \mathbf{x}(n-1) \\ | & | & & | \end{pmatrix} \quad (3.1)$$

and the following representation for $X(t+1) \in \mathbb{R}^{d \times n-1}$

$$X(t+1) = \begin{pmatrix} | & | & \cdots & | \\ \mathbf{x}(2) & \mathbf{x}(3) & \cdots & \mathbf{x}(n) \\ | & | & & | \end{pmatrix} \quad (3.2)$$

The least-squares will now seek to fit a linear operator A such that:

$$X(t+1) \approx AX(t) \quad (3.3)$$

This linear operator representation of the dynamical system has connections to Koopman operator theory [90] and Dynamic Mode Decomposition in Fluid Mechanics

[91]. We seek to approximate the inherently nonlinear iEEG dynamics within a small window of time using a finite-dimensional approximation of the Koopman operator using the observables (i.e. $x(t)$) themselves. We specifically used least-squares algorithm with a $10e-5$ l2-norm regularization to ensure that the model identified was stable (with absolute value of eigenvalues ≤ 1) as in [81, 82]. Then, we slid the window 125 ms and repeated the process over the entire data sample, generating a sequence of linear network models in time as in Figure 3-2.

We systematically computed the minimum perturbation required for each electrode’s connections (see Figure 3-2) to produce instability for the entire network as described in [81]. This is represented in equation 3.4, where the Δ_i is the desired column perturbation matrix for channel i , and the $\lambda = r \in \mathbb{C}$ is the desired radii to perturb one single eigenvalue to.

$$\Delta_i = \min \|\Delta_i\| \text{ s.t. } \exists \lambda = r \in \sigma(A + \Delta) \tag{3.4}$$

More specifically, we compute a structured perturbation matrix, such that:

$$\Delta_i = \begin{pmatrix} | & & | & & | \\ \mathbf{0} & \cdots & \Gamma_i & \cdots & \mathbf{0} \\ | & & | & & | \end{pmatrix} \tag{3.5}$$

where each $\Gamma_i \in \mathbb{R}^d$ is the actual column perturbation vector. The intuition for using this type of structured perturbation is described in 3. We demonstrate how to solve for this using least-squares in [81]. The electrodes that were the most fragile were hypothesized to be related to the SOZ in these epilepsy networks.

Baseline features - spectral features

We constructed spectral-based features from frequency bands of interest by applying a multi-taper Fourier transform over sliding windows of data with a window/step

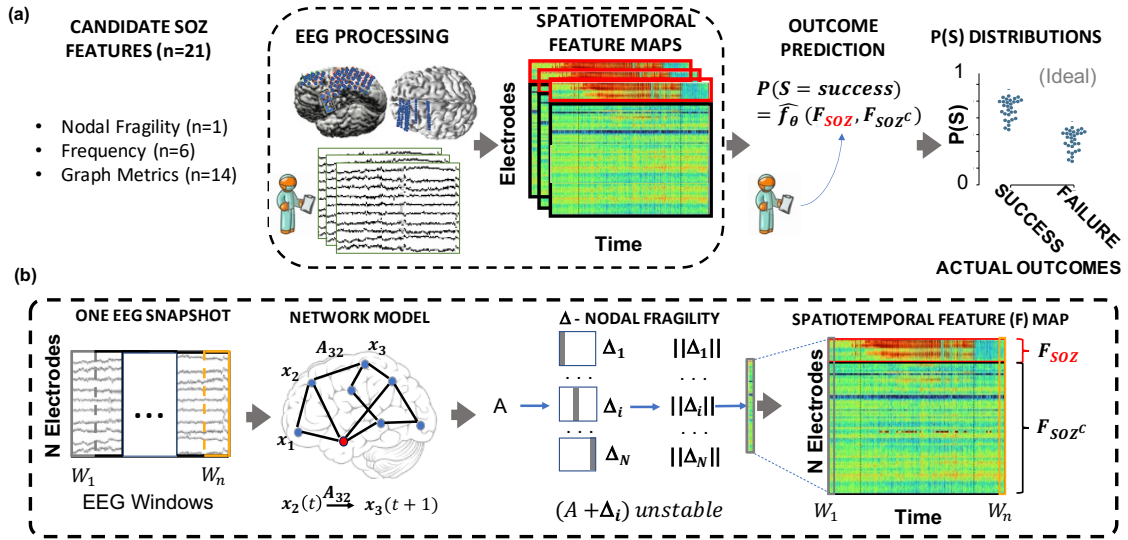


Figure 3-2. Computational experiment setup for all candidate *SOZ* features and statistical analysis - (a) Any candidate feature that can produce a spatiotemporal heatmap was computed from EEG data and then partitioned by the clinically annotated *SOZ* set and the complement, SOZ^C (i.e. non-*SOZ* electrodes) to compute a confidence statistic measuring the feature's belief of the clinician's hypothesis. Here F_{SOZ} and F_{SOZ^C} were the feature values within their respective sets. f_θ is the function depending on the Random Forest model parameters, θ that maps the statistics of the F_{SOZ} and F_{SOZ^C} to a confidence statistic. An ideal feature would have high and low confidence for success and failed outcomes respectively. Each point on the final CS distribution comparisons represent one patient. **(b)** A more detailed schematic of how our proposed fragility and baseline features were computed from EEG data for a single snapshot of EEG data. See fragility methods section for description of x , A and Δ .

size of 2.5/0.5 seconds [43, 92]. We required relatively longer time windows in order to accurately estimate some of the lower frequency bands. Each EEG time series was first transformed into a 3-dimensional array (electrodes X frequency X time), and then averaged within each frequency band to form six different spectral feature representations of the data. We break down frequency bands as follows:

1. Delta Frequency Band [0.5 - 4 Hz]
2. Theta Frequency Band [4 - 8 Hz]
3. Alpha Frequency Band [8 - 13 Hz]
4. Beta Frequency Band [13 - 30 Hz]
5. Gamma Frequency Band [30 - 90 Hz]
6. High-Gamma Frequency Band [90 - 300 Hz]

Note that the High-Gamma frequency band includes frequencies of "ripples" - a category of HFOs.

Baseline features - graph analysis of networks

We computed a time domain model using Pearson correlation (equation 3.6) and a frequency domain model using coherence (equation 3.7). We computed the connectivity matrix using MNE-Python and used the default values [93, 94]. In the equations, (i, j) are the electrode indices, Cov is the covariance, σ is the standard deviation, f is the frequency band, and G is cross-spectral density. Note that these connectivity models attempt to capture linear correlations either in time, or in a specific frequency band, but are not dynamical system representations of the data (i.e. $x(t+1) = Ax(t)$). In Figure 3-3, for each network-based feature, a sliding window/step size of 2.5/0.5 seconds were used, resulting in a sequence of network matrices over time resulting in 3-dimensional arrays (electrodes X electrodes X time) [43, 44, 80].

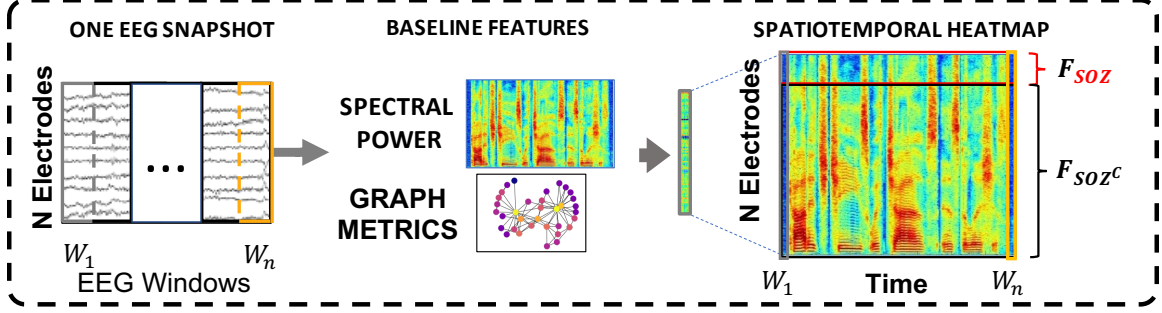


Figure 3-3. Baseline feature evaluation schematic - An schematic describing how we processed baseline features, such as spectral power, and graph metrics. The feature heatmap processing is exactly the same as fragility, allowing us to compare the feature representations of neural fragility, spectral power and graph metrics of correlation and coherence derived graphs for the purposes of SOZ localization.

$$Corr_{ij} = \frac{Cov(x_i, x_j)}{\sigma_{x_i} \sigma_{x_j}} \quad (3.6)$$

$$Coh_{ij}(f) = \frac{|G_{ij}(f)|^2}{G_{ii}(f)G_{jj}(f)} \quad (3.7)$$

From each network matrix, we computed the eigenvector centrality [43, 80], and the degree [57] features of the network for each electrode across time. Since coherence and pearson correlation are symmetric matrices, the in-degree is equivalent to the out-degree. Centrality describes how influential a node is within a graph network. Degree is the weighted sum of the connections that connect to a specific node. Both features are potential measures that attempt to capture the influence of a specific electrode within an iEEG network, through the lens of graph theory. Inherently, these feature assume that the connectivity model is represented by linear correlations either in time, or a specific frequency band. We produced a spatiotemporal heat map of electrodes over time of the eigenvector centrality and the in-degree for all datasets.

Experimental design

We tested if the neural fragility representation of iEEG data localized the *SOZ* better compared to other proposed features, compared to clinicians and compared to chance. Electrodes with extreme feature values deviating from the average were hypothesized as part of the *SOZ*.

To compute a probability of successful surgical outcome for each patient, we trained a non-parametric machine learning classifier, a Random Forest classifier to output a probability value that the surgery was a success. We input the distribution of feature values in the clinically *SOZ* and the *SOZ^C*. We considered a set of hyperparameters that we then performed evaluation over a 10-fold nested cross-validation scheme. We then performed statistical analysis on the final classification performance to determine the most robust feature representation.

Pooled Patient Analysis

First, we analyzed the difference in the distributions of neural fragility between *SOZ* and the *SOZ^C*. We pooled all patients together, stratified by surgical outcome and compared the neural fragility distributions using a one-sided Mann-Whitney U test (Success pvalue = 3.326e-70, Fail pvalue = 0.355; Figure 3-4). This suggested that there is some effect on average where fragility is higher in the *SOZ* for successful outcomes, so we next looked at the distributions per patient's seizure snapshot around seizure onset. In Figure 3-5, success outcome patients have a higher neural fragility in the *SOZ*. This effect is seen when pooling patients across all centers as well, where neural fragility is either i) higher before the seizure onset, or ii) has a marked difference starting at seizure onset (Figure 3-6). Next, we performed a classification experiment (Figure 3-1) that would determine the robustness of the neural fragility representation at the patient level benchmarked against 20 other features.

Non-parametric Decision-Tree Classifier

To determine the value of a feature representation of the iEEG data, we posed a binary classification problem where the goal would be to determine the surgical outcome (success or failure) for a particular patient’s spatiotemporal heatmap. Each spatiotemporal heatmap was split into its *SOZ* and *SOZ^C* set (F_{SOZ} and F_{SOZ^C} in Figure 3-2). Then each set of electrodes’ feature distributions were summarized with its quantile statistics over time, resulting in twenty signals: ten quantiles from 10-100 of the *SOZ* and ten quantiles of the *SOZ^C* over time. We used a Random Forest (RF) classifier [95]. Specifically, it was a variant known as the Structured Random Forest, or Manifold Random Forests [96, 97]. The manifold RF approach allows one to encode structural assumptions on the dataset, such as correlations in time of the fed in data matrix. The input data matrix for each RF is a multivariate time series that summarizes the quantile statistics of the *SOZ* and *SOZ^C* over time. As a result, we obtained better results using the manifold RF because it took advantage of local correlations in time, rather than treating all values in the data matrix input as independent as done in a traditional RF model. This approach allowed our classifiers to learn faster with less data, compared to treating all inputs as independent in the traditional RF model. For more information on how manifold RF improves on traditional RF, we refer readers to [96, 97]. For every model, we used the default parameters from scikit-learn and the rerf package [97, 98]: 500 estimators, max depth is None, minimum samples split is 1, max features is auto, feature combinations is 1.5, image height of 20 (20 quantiles total), patch height max of 4, patch height minimum of 1, patch width max of 8, patch width minimum of 1. The output of the decision tree classifier is:

$$\hat{f}_\theta(F_{SOZ}, F_{SOZ^C}) = P(\text{success})$$

where θ are the trained RF parameters and F_{SOZ} are the heatmap values for the SOZ and F_{SOZ^C} are the heatmap values for the SOZ^C for a specific feature representation F (shown in Figure 3-2). \hat{f} is the function we are trying to estimate, which predicts the probability of successful surgical outcome for a given feature heatmap.

Hyperparameters

When looking at iEEG data, clinicians inherently select windows of interest due to external and prior information about when the seizure clinically manifests. Similarly, we consider a window of 10 seconds before seizure onset to the first 5% of the seizure event. This window was chosen apriori to analysis, and we repeated the analyses with slightly varying windows, but the results were consistent. To provide further contrast to the spatiotemporal heatmaps, we considered also a threshold between 0.3 and 0.7 (spaced by 0.1) that would be applied to the heatmap such that values below were set to 0. This is analogous to clinicians being able to look at a iEEG data and hone in only on areas that are extreme relative to the rest. We selected a fixed threshold through nested cross-validation, where thresholds are selected on the train/validation set, and then performance is measured on the held out test set.

Structured Heatmap Input

To train a RF classifier on patients with varying number of channels, we structured the spatiotemporal heatmap inputs to summarize the distributions of the feature values in the SOZ and SOZ^C sets. We converted these into a vector of 20 quantile values (10 quantiles for SOZ and 10 for SOZ^C), taken evenly from the 10th to the 100th quantiles. This forms a data matrix per heatmap (20×105 size), which summarizes the SOZ and SOZ^C distributions over time, fixed around the seizure onset time.

Nested Cross-Validation Feature Evaluation

It is common practice when building a supervised machine learning model to incorporate cross-validation (CV) where the dataset is split into a training and testing set. However, when one has hyperparameters (in addition to the machine learning model parameters) it is crucial to control against over-fitting to the test dataset [63]. Due to our hyperparameter selection of the optimal heatmap thresholds, we used a nested CV scheme, where we split the dataset into a training, validation and a "lock-box" dataset, where the hyperparameters were tuned on an inner CV (70% of the dataset) with the training and validation data, and then performance was evaluated on the lock-box dataset. All features were optimized separately, so that their hyperparameters were optimal for that feature. We computed the discrimination statistic known as the area under the curve (AUC). We repeated the nested-cross validation 10 times, resulting a 10-fold CV. Statistical analysis was done using nested cross-validation, splitting training, validation and testing groups based on subjects, while sampling proportionally the different epilepsy etiologies. We set aside 60% of subjects for training, 10% for validation and then 30% as a held-out test set. We used a heuristic of attempting to sample approximately randomly from clinical complexity 1-4 as defined in the paper. This heuristic attempted to place at least 25% of the subjects in the training, validation and held-out test set for each clinical complexity. Besides this covariate, the training, validation and held-out test set were determined randomly. We found that this performed slightly better for all features compared to random sampling. We performed patient-level CV, ensuring that no patient was in multiple splits of the dataset (i.e. any one patient is only in the train, test, or lock-box dataset).

Statistical analysis

Success probability values were computed from the RF classifiers trained on the spatiotemporal feature representations of the iEEG data (fragility, spectral features, and graph metrics from correlation and coherence graphs) resulting in a distribution of probabilities for each feature.

To compare the RF model performance across the 20 proposed features of fragility, spectral power and graph metrics, we computed Cohen’s D effect size differences between the groups of interest, and then Mann-Whitney U tests for unpaired data, and paired Wilcoxon rank-sum tests for paired data [99]. We corrected for any multiple comparisons using the Holm-Bonferroni step-down method. In some cases, we also present the Likelihood Q-ratio test (LQRT) results to show that the results are robust to statistical test chosen. The LQRT has been shown to be more robust compared to both the Mann-Whitney U-test and t-test in the presence of noise [100, 101]. LQRT utilizes a bootstrapping procedure, so it’s resolution is 0.001 (i.e. if it produces a p-value of 0, then that means it is < 0.001). Since the Mann-Whitney, Wilcoxon and LQRT tests do not rely on a parametric assumption of normality, no explicit parametric assumptions were made. In certain cases, where we report results of a t-test as well, we assumed that the data distribution might be normal, but this was not formally tested.

We compared the success probabilities stratified by different clinical covariates: surgical outcome, Engel class, clinical complexity, handedness, gender, onset age, and surgery age. We then estimated the effect size differences between distributions in the form of a Cohen’s d statistic. Cohen’s d was estimated using a non-parametric bootstrapping on the observed data with 5000 re-samples used to construct a 95% confidence interval [99]. The null hypothesis of our experimental setup was that the success probabilities came from the same population. The alternative hypothesis was

that the populations were different (i.e. a feature could distinguish success from failed outcomes, or between different Engel classes).

Feature evaluation using predicted probability of successful surgery

The fragility and all baseline features proposed generated a spatiotemporal heatmap using EEG snapshots of ictal data. To compare spatiotemporal heatmaps across features, we computed a probability of success (i.e. a confidence score) that is hypothesized to be high for success outcomes and low for failures for "good" features. We expected that fragility would follow a trend of decreasing confidence as CC, Engel score and ILAE score increase. For each clinical covariate group, we measured the effect size difference via bootstrapped sampling, and the statistical p-value between the distributions. We **hypothesized that**: i) fragility would have an effect size difference significantly different from zero when comparing success vs failed outcomes, ii) in addition, this effect size would correlate with meaningful clinical covariates, such as CC and Engel class and iii) both the effect size and p-value would be better than the proposed baseline features.

The higher the probability of success (closer to 1), the more likely the feature indicated a successful surgery, and the lower it was (closer to 0), the more likely the feature indicated a failed surgery. To compute this value, we first partition the heatmap into a SOZ and SOZ^C . This forms the two sets of signals that represent the spatiotemporal feature values of the SOZ set vs the SOZ^C set of electrodes. Then we take windows of interest, where clinicians find most valuable for SOZ localization: the period before seizure and right after seizure onset, and performing a nested CV of RF models. The efficacy of each proposed feature is evaluated based on how well the trained RF model is able to predict the surgical outcomes. We tested our hypotheses stated above by computing a probability of success from each feature heatmap for

each patient, and estimated the distribution differences of the CS between various clinical covariates.

Spatiotemporal feature heatmap interpretability

To determine how valid the output probability values are, we first computed a calibration curve, which told us how well-calibrated the probability values were. We furthermore compared the calibration curves across neural fragility, spectral features and graph metrics. With relatively good discrimination measured by the AUC and good calibration, we were able to then compare the CS across clinical complexity (CC) scores, Engel scores and ILAE scores. Since epilepsy and reasons for failed surgeries are so complex, these are clinical methods for stratifying patient groups based on observed etiology. We analyzed how the success probability differs across each of these categories. In addition, we looked at how the success probabilities might differ across other clinical variables, such as sex (M vs F), handedness (R vs L), epilepsy onset age (years), and age during surgery (years).

Qualitatively reading off a spatiotemporal heatmap is highly interpretable as one can match raw iEEG segments to certain time periods in the heatmap. For every patient, the time-varying quantile signals (from 10th to the 100th) of the SOZ and SOZ^C were computed for every iEEG heatmap, as specified in [Methods - Experimental design](#). We used permutations feature importance sampling to obtain a relative weighting of each signal over time and how important it was in allowing the RF to correctly determine surgical outcome. This was visualized as a heatmap showing the mean and std importance scores of the SOZ and SOZ^C statistics, as shown in Extended Data Figure 7).

In addition, we claim that human interpretability of the spatiotemporal heatmap relies on contrast between the SOZ and SOZ^C regions in successful outcomes. Using the results of the feature importance permutation test, we computed for every heatmap,

an interpretability ratio, which was defined as:

$$I = \frac{F_{SOZ}(90th)}{F_{SOZ^C}(90th)}$$

where I is the interpretability ratio for a specific subject's feature heatmap F . $F_{SOZ}(90th)$ is the 90th quantile and up feature values of the SOZ , and $F_{SOZ^C}(90th)$ is for the SOZ^C . This ratio is then stratified according to surgical outcome, which we expect higher ratios for successful outcomes and lower ratios for failed outcomes. We quantified this difference using Cohen's D effect size and Mann Whitney U-test Pvalues (see [Methods - Statistical analysis](#)).

Fragility heatmaps are more interpretable than all other EEG feature maps

We can parse the RF model to determine important aspects of the spatiotemporal heatmap that are important in predicting surgical outcome. To do so, we perform permutations on the heatmap inputs to the RF models to measure their relative importances over space and time. We observed that the AUC metric was affected primarily by a combination of the highest (90th quantiles and up) neural fragility values of both the SOZ and SOZ^C contacts. The SOZ^C neural fragility as much as 10 seconds before seizure onset impacted the AUC as did neural fragility of the SOZ right at seizure onset. For both the SOZ and the SOZ^C fragility distributions, the 80th quantile and below did not contribute to the predictive power. In different patients across different clinical centers, the practice of marking seizure onset times can vary due to varying methodologies [7]. As a result, in the SOZ^C , there was some variation in terms of which time point in the heatmap mattered most.

Although strong predictive capabilities of an EEG marker of the SOZ are promising, it is also important that the marker be presented in an interpretable manner to clinicians. We next show how fragility heatmaps are the most interpretable over all

baseline features. In Extended Data Figure 9a, there are two heatmaps computed for the same seizure event in Patient_01: one is a beta band map (left) and one is a neural fragility map (right). Both maps are normalized across channels and both are computed with similar sliding windows. However, less contacts "stand-out" as pathological in the beta-band heatmap before seizure onset, with the majority of the map being different shades of blue. In contrast, in the fragility heatmap, one contact (**ATT1** from Figure ??) is fragile the entire duration before seizure onset (solid white line), and then a few more contacts become fragile after the electrographic onset of the seizure. These fragile areas that "pop-out" in the heat-map as red-hot areas occur in the clinically annotated SOZ and this patient had a successful surgery.

To quantify interpretability, we compute an interpretability ratio: the ratio of the feature values in the 90th quantile between the *SOZ* and the *SOZ^C* over the section of data used by the feature's RF model. This measures the contrast that one sees between the extreme values in the *SOZ* versus the extreme values they see in the *SOZ^C*. The larger the ratio, then the more contrast the map will have. In Extended Data Figure 9b, we show that the effect size difference between successful and failed outcome of this interpretability ratio is largest in neural fragility when compared to all baseline features. It is well-known that RF models are scale-invariant [95], so it is plausible that there are portions of heatmaps that distinguish one channel from another that can be parsed out via a decision tree and not the naked eye, which leads to high AUC in the beta band representation in Figure ?. For example a decision tree can discriminate between 0.3000 and 0.2995, which on a normalized color-scale is difficult to parse by visual inspection. Neural fragility on the other hand, shows marked differences between the clinically annotated *SOZ* (red electrodes on the y-axis) and the actual fragility values even before seizure onset.

Data availability

We also released the raw iEEG data for patients from NIH, UMH, UMMC, and JHH in the OpenNeuro repository in the form of BIDS-iEEG (<https://openneuro.org/datasets/ds003029>). Due to restrictions on data sharing from CClinic, we were unable to release the raw iEEG data that we received from this site. Dataset from CClinic is available upon request from authors at the CClinic.

Code availability

All main figures of the manuscript can be reproduced using Gigantum at <https://gigantum.com/adam2392/neural-fragility-ictal-study-figures> [Gigantum2021]. We include a jupyter notebook written in Python to help reproduce figures. An example of neural fragility being run on Patient_01 can be shared upon request due to licensing restrictions. The neural fragility algorithm has been implemented in a FDA 510k approved software medical device (current 510k number: K201910). More information will be available at www.neurologicsolutions.co. Otherwise, please contact corresponding authors for more information regarding a clinical demonstration.

Results - Neural fragility can localize the epileptogenic zone

Neural fragility is a paradigm shift in the EEG analytics space. It is a concept based on the conjecture that focal seizures arise from a few fragile nodes, i.e., the SOZ, which renders the cortical epileptic network on the brink of instability. When one observes iEEG data during interictal, or preictal periods, activity recorded from each channel *appears* to hover around a baseline value (Figure 2-1 left). If the network is "balanced", then it will respond transiently to an impulse, but always returns to a baseline value (e.g. Figure 2-2ab). In contrast, when one observes iEEG data during a seizure event,

activity (i) grows in amplitude, (ii) oscillates, and (iii) spreads in the brain when the network is perturbed (Figure 2-1 right). This is a consequence of an "unbalanced" network that does not return to a baseline value (e.g. Figure ??c). From a dynamical systems perspective, the iEEG network has switched from a stable (non-seizure) to an unstable (seizure) network.

Biologically, imbalance due to perturbations between excitatory and inhibitory connections of a neural network can occur through any number of mechanisms, such as elevated glutamate [102, 103], genetic disorder impacting synaptic inhibition [104], decreased GABA [105], inclusion of axo-axonic gap junctions [106], loss of inhibitory chandelier cells [107], or axonal sprouting from layer V excitatory pyramidal cells [108]. This imbalance within a neural network may lead to functional instability, where impulses at certain nodes lead to recurring seizures. While iEEG cannot distinguish between excitatory and inhibitory neuronal populations, the concept of imbalance causing the network to be on the brink of instability can be modeled by neural fragility at the iEEG network level.

To demonstrate how fragility is computed from a dynamical model, we consider a 2-node network as shown in Figure 2-2. In Figure 2-2a), a stable network is shown where excitation and inhibition are balanced. The network model is provided in the top row and takes a linear form, $\mathbf{x}(t + 1) = \mathbf{A}\mathbf{x}(t)$, where t is a time index (typically one millisecond). When the inhibitory node is stimulated by an impulse, both nodes transiently respond and the EEG returns to baseline (bottom row in Figure 2-2). In panel b), the inhibitory node's connections are slightly perturbed in a direction that makes the inhibitory node *less* inhibitory (see changes to its connectivity to the excitatory node). Now, when the inhibitory node is stimulated by an impulse, the responses from each node have a larger transient response but still return to baseline. Finally, in panel c), the inhibitory node's connections are further perturbed in a direction that makes the inhibitory node *less* inhibitory. Now, when the inhibitory

node is stimulated by an impulse, the responses oscillate demonstrating that the network has gone unstable. The fragility of the inhibitory node is thus quantified as $\sqrt{8}$ which is the norm of the perturbation vector applied to the first column of A . Our conjecture is that small changes in connection strengths at *SOZ* nodes cause an imbalance in connectivity between nodes in the network, resulting in susceptible seizures.

To test our conjecture, we estimate a linear time-varying model with a sliding window of A matrices, that characterize a linear dynamical system: $x(t + 1) = Ax(t)$ [81, 82]. This is a generative model representing the linear dynamics between iEEG channels within a small window of time. Each A matrix is *estimated* from data via a least-squares method. We have shown that this linear approximation is a valid model of the data [82]. From this model, we compute the minimum 2-norm perturbation matrix, $\{\Delta\}_{j=1}^N$, over all N channels [81] (see Extended Data Figure 1). The 2-norm of each perturbation matrix represent the neural fragility for that channel. Computing the fragility now across sequentially estimated A matrices results in a spatiotemporal neural fragility heatmap. For a full description of neural fragility, see Methods Section.

Neural fragility agrees with clinicians on successful surgical outcomes

To qualitatively assess the usefulness of fragility in localizing electrodes of interest, we first look at specific examples of patients with varying outcomes and epilepsy etiologies (see Figure 3-1). We analyzed with fragility and demonstrate how it may provide additional information for SOZ localization. In Figure 3-7, we show three patients with differing surgical treatments, outcomes, Engel class and clinical complexity along with their fragility heatmaps and corresponding raw iEEG data (for full clinical definitions; see Supplementary Excel table). See Figure 3-8 for the entire heatmap over the seizure event.

In Figure 3-7a, the red electrode labels on the y-axis correspond to the clinical *SOZ* electrodes; the red electrodes are typically a subset of the resected region. It shows the period 10 seconds before and after electrographic seizure onset (black dashed line). In Patient_1, the fragility heatmap agreed with clinical visual EEG analysis, identifying the *SOZ*, which was surgically resected and led to a seizure free patient. The clinical *SOZ* has high fragility, even before seizure onset, which is not visible in the raw EEG. The heatmap for Patient_1 also captures the propagation of seizure activity (Extended Data Figure 2). This patient had a successful surgery, and so we can assume the resected tissue likely contained the epileptic regions; it is likely clinicians correctly localized the EZ. When viewing the raw EEG data in Figure 3-7b (top), Patient_1 has iEEG signatures that are readily visible around seizure EEG onset (Figure 3-7b). We see high-frequency and synchronized spiking activity at onset that occurs in electrodes that clinicians annotated as *SOZ*, which correspond to the most fragile electrodes at onset. In addition, the fragility heatmap captures the onset (**ATT** and **AD** electrodes) and early spread of the seizure (**PD** electrodes). Moreover, **ATT1 (anterior temporal lobe area)** shows high fragility during the entire period before seizure onset (Figure 3-7). This area was not identified with scalp EEG, or non-invasive neuroimaging.

Neural fragility disagrees with clinicians on successful surgical outcomes

In Figure 3-7, Patient_26 and Patient_40 both show regions with high fragility that were *not* in the clinically annotated *SOZ* (or the resected region), and both had recurrent seizures after surgery. From seizure onset, many electrodes in both patients exhibit the clinically relevant EEG signatures, such as spiking and fast-wave activity [88]. In the raw EEG, one can see synchronized spikes and spike-waves, but ultimately the epileptic regions were not successfully resected. Visual analysis of

the EEG was insufficient for Patient_26 and Patient_40, which ultimately led to insufficient localizations and failed surgical outcomes.

Patient_26 had a resection performed in the right anterior temporal lobe region where clinicians identified the *SOZ* (**RAD**, **RHD** and **RTG40/48** electrodes). However, **ABT** (**anterior basal temporal lobe**), **PBT** (**posterior basal temporal lobe**) and **RTG29-39** (**mesial temporal lobe**) electrodes were highly fragile compared to the clinical *SOZ*, but not annotated as *SOZ*. In the raw EEG shown in Figure 3-7b, it is not apparent that these electrodes would be part of the *SOZ*. Patient_40 had laser ablation performed on the electrode region associated with **Q2**, which was not fragile. However, **X'** (**posterior-cingulate**), **U'** (**posterior-insula**) and **N'/M'/F'** (**superior frontal gyrus**) electrodes were all fragile compared to **Q2**, which recorded from a lesion in the right periventricular nodule. Based on these heatmaps, the fragile regions could be hypothesized to be part of the *SOZ*, and possibly candidates for resection.

Neural fragility outperforms other features in predicting the surgical outcome of patients

To test the validity of neural fragility and the baseline features as *SOZ* markers, we investigate each feature's ability to predict surgical outcomes of patients when stratified by the set of *SOZ* contacts and the rest which we denote as the *SOZ* complement, SOZ^C (for a distribution of patient outcomes, see Supplementary Figure I-1 and Table 1). Neural fragility in the *SOZ* was significantly higher than the SOZ^C in successful patients as compared to failed patients (Success pvalue = $3.326e-70$, Fail pvalue = 0.355; Figure 3-4) Patient_01 has higher neural fragility in the *SOZ* when compared to Patient_26 and Patient_40 (Figure 3-5). This effect is seen when pooling patients across all centers as well, where neural fragility is either i) higher before the seizure onset, or ii) has a marked increase starting at seizure onset (Figure 3-6). To

evaluate this at a single subject level, we train a Structured Random Forest model (RF) for each feature that takes in a partitioned spatiotemporal heatmap based on the clinically annotated *SOZ* and generates a probability of success - a confidence score in the clinical hypothesis (for full details, see [Methods](#) Section). We test each feature's model on a held out data set by applying a threshold to the model's output and computing a receiver operating characteristic (ROC) curve. The ROC curve plots true positive rates versus false positive rates and the area under the curve (AUC), a measure of predictive power of the feature. We also compute the precision (PR) or positive predictive value (PPV) for each feature, which is the proportion of predicted successful or "positive" results that are true positives (actual successful surgeries). In addition, we compute the negative predictive value (NPV) as well. The larger the AUC/PPV/NPV is for a feature, the more predictive it is and thus more valid as an iEEG marker of the *SOZ*.

Since each patient's implantation has varying number of electrodes, we summarize each feature's distribution of the *SOZ* and *SOZ^C* electrodes into quantile statistics over time (see [Methods - Experimental design](#)). As an input to the RF models, we compute the quantile statistics over time of the *SOZ* and *SOZ^C* set for each patient and each feature, which are input into a machine learning RF model. RF models are attractive because they are non-parametric, interpretable (they are a set of decision trees performing a consensus procedure), and able to handle higher dimensional data better compared to other models, such as Logistic Regression [109]. As an output of the trained RF model, each heatmap gets mapped to a probability that the outcome will be a success. An RF model is tuned for each feature through 10-fold cross-validation (CV; see [Methods - Experimental design](#)), resulting in a uniform benchmark against neural fragility on the same set of patients. Similar to neural fragility, all benchmark features are computed as heatmaps (Figure 3-3). The "high-gamma" frequency band feature encompasses what some would consider HFOs (i.e. 90-300 Hz).

In terms of AUC (measures discrimination), neural fragility performs the best (Figure ??a). Compared to the top 3 leading baseline features, neural fragility outperforms the beta band (15-30 Hz) power by more than 13%. The AUC of fragility is the highest with a value of 0.88 +/- 0.064, compared to the next best representation, the beta frequency band, with a value of 0.82 +/- 0.040. From the ROC and PR curves, we observe that the fragility consistently has a higher sensitivity for the same false positive rate compared to the 20 other feature representations (Extended Data Figure 6). In terms of effect size, neural fragility improves over the beta frequency band with a large effect size of 0.97 Cohen's D with 9 out of 10 folds improving the AUC (Paired Wilcoxon Rank-sum PValue = 0.027 (Extended Data Figure 6).

In terms of PR (measures PPV), neural fragility also performs the best (Figure ??b). In terms of average precision, which weighs the predictive power in terms of the total number of patients, neural fragility also obtains an average precision of 0.83 +/- 0.076, which is >5% better than the next best feature. In addition, compared to the clinical surgical success rate of 47%, fragility had a 76% +/- 6% accuracy in predicting surgical outcome, a PPV of 0.903 +/- 0.103 and a NPV of 0.872 +/- 0.136. In terms of PR, neural fragility improves over the beta band power with a medium effect size of 0.57 Cohen's D with 8 out of 10 folds improving the PR (PValue = 0.08).

When we compare the success probabilities predicted by the models between surgical outcomes, we observe that neural fragility separates success and failed outcomes the most with a Cohen's D of 1.507 (1.233-1.763; 95% confidence interval) (Figure ??c) and pvalue of 6.748e-31 (Figure ??d). In addition to having good discrimination, we compute how well-calibrated the model is - that is having the success probabilities values reflect true risk strata in the patient population. For example, a perfectly calibrated model would have a 20% confidence in a set of patients with exactly 20% success outcomes. We quantify how well calibrated the success probability distributions are over the held-out test set and find that the RF model trained on neural fragility

produces well-calibrated predictions (Extended Data Figure 6). The Brier-loss (a measure of calibration; 0 being perfect) was 0.162 +/- 0.036, which was a 6.7% improvement compared to the next best feature.

Neural fragility correlates with expected clinical covariates

Neural fragility also correlates with more granular treatment outcomes and clinical complexity. Successful seizure-free outcomes (Engel I and ILAE 1) and failure seizure-recurrence outcomes (Engel II-IV) are defined at 12+ months post-op. In addition, we can categorize patients by their clinical complexity (CC) as: (1) lesional, (2) focal temporal, (3) focal extratemporal, and (4) multi-focal (Figure 3-1a) [7]. We stratify the distribution of the success probabilities based on Engel score and show a decreasing trend in success probability as Engel score increases (Figure 3-11b). The effect sizes when comparing against Engel I were 1.067 for Engel II ($P = 4.438e-50$), 1.387 for Engel III ($P = 2.148e-69$), and 1.800 for Engel IV ($P = 4.476e-74$). Although the AUC indirectly implies such a difference would exist between Engel I (success) and Engel II-IV (failures), we also observe that confidence decreases as the severity of the failure increases; Engel IV patients experience no changes in their seizures, suggesting the true epileptic tissue was not localized and resected, while Engel II patients experience some changes, suggesting there was portions of the true epileptic tissue that may have been resected. We also compare the success probability distributions with respect to the ILAE score, which is another stratification of the surgical outcomes (Figure 3-11c). There is a similar trend as seen in the Engel score - as ILAE score increases, the success probability decreases.

We also analyze the success probability with respect to the epilepsy severity measured by the clinical complexity (CC) of the patient, which is a categorization of the etiology of the disease. CC is determined by what type of seizures the patient exhibits rather than the severity of the seizures after-surgery (see [Methods - Data](#)

collection). CC is a factor that is determined before surgery and one we expect could correlate with failure rate. The higher the CC, the more difficult localization is and hence more likely seizures recur after surgery. In Figure 3-11a, we observe that CC1 and CC2 (i.e. lesional and temporal lobe) patients had a similar distribution of success probabilities (Cohen’s $D = 0.020$; MW U-test PValue = 0.799; LQRT PValue = 0.76), while CC3 and CC4 had significantly lower distributions (CC3: [Cohen’s $D = 0.779$; MW U-test PValue = $2.808e-19$; LQRT PValue = 0.00]; CC4: [Cohen’s $D = 1.138$; MW U-test PValue = $7.388e-26$; LQRT PValue = 0.00]). This trend is not optimized for directly in our discrimination task, but it aligns with clinical outcomes. CC1 and CC2 are comparable, which agrees with current data suggesting that lesional and temporal lobe epilepsy have the highest rates of surgical success [7, 72]. Extratemporal (CC3) and multi-focal (CC4) patients tend to have lower success rates due to difficult localizations and thus the neural fragility confidence in those *SOZ* localizations should be low [7].

The highest values of neural fragility (i.e. red zones) that differentiates the *SOZ* and *SOZ^C* contribute the most to making a correct classification (Figure 3-12). In general neural fragility is not correlated with any single frequency band (Figure 3-13). We also show how fragility heatmaps are the most interpretable over all baseline features. When comparing the contrast between *SOZ* and *SOZ^C* of success and failed patients, neural fragility has the largest difference, whereas beta power is hard to distinguish (Figure 3-14). Finally, we examine the model predictions based on gender, handedness, onset age and surgery age to show that there are no relevant differences (Supplementary Figure I-2).

Discussion

Challenges in validating iEEG features as SOZ markers

Clinical case complexity and surgical outcomes

Limitations of the most popular iEEG features

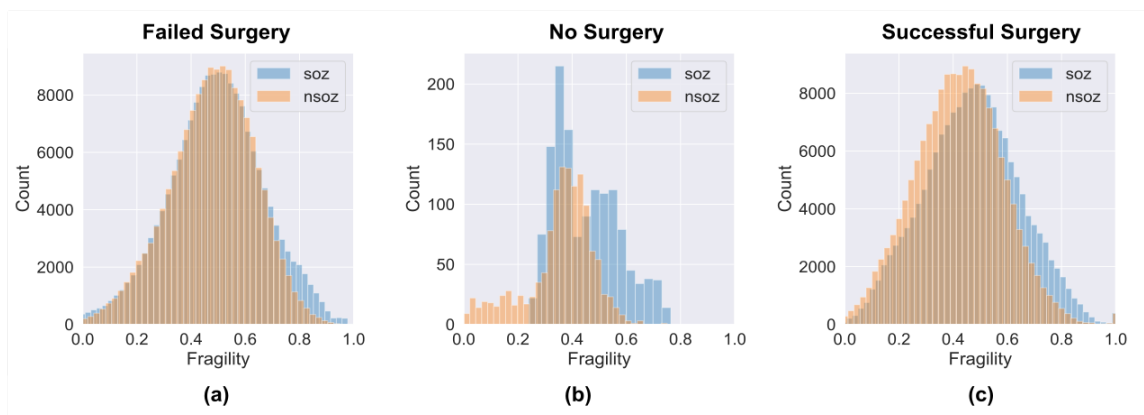


Figure 3-4. Pooled fragility distribution analysis for all patients - failed (a), no surgery (b) and successful surgery (c) datasets. Each *SOZ* (soz in blue bars) and *SOZ^C* ('nsorz' in orange bars) distribution per patient was bootstrap sampled (see [Methods](#) for more information on sampling) and then compared using the one-sided Mann-Whitney U test. The corresponding test yielded a statistic of 2776334 (PValue = 0.355) for the failed patient outcomes and a statistic of 36836739 (PValue = 3.326e-70) for the successful patient outcomes. The patients without resection were not included in the analysis comparing to outcome, but these patients can present as interesting case studies where the SOZ was hypothetically localizable, but perhaps was too close to eloquent areas.

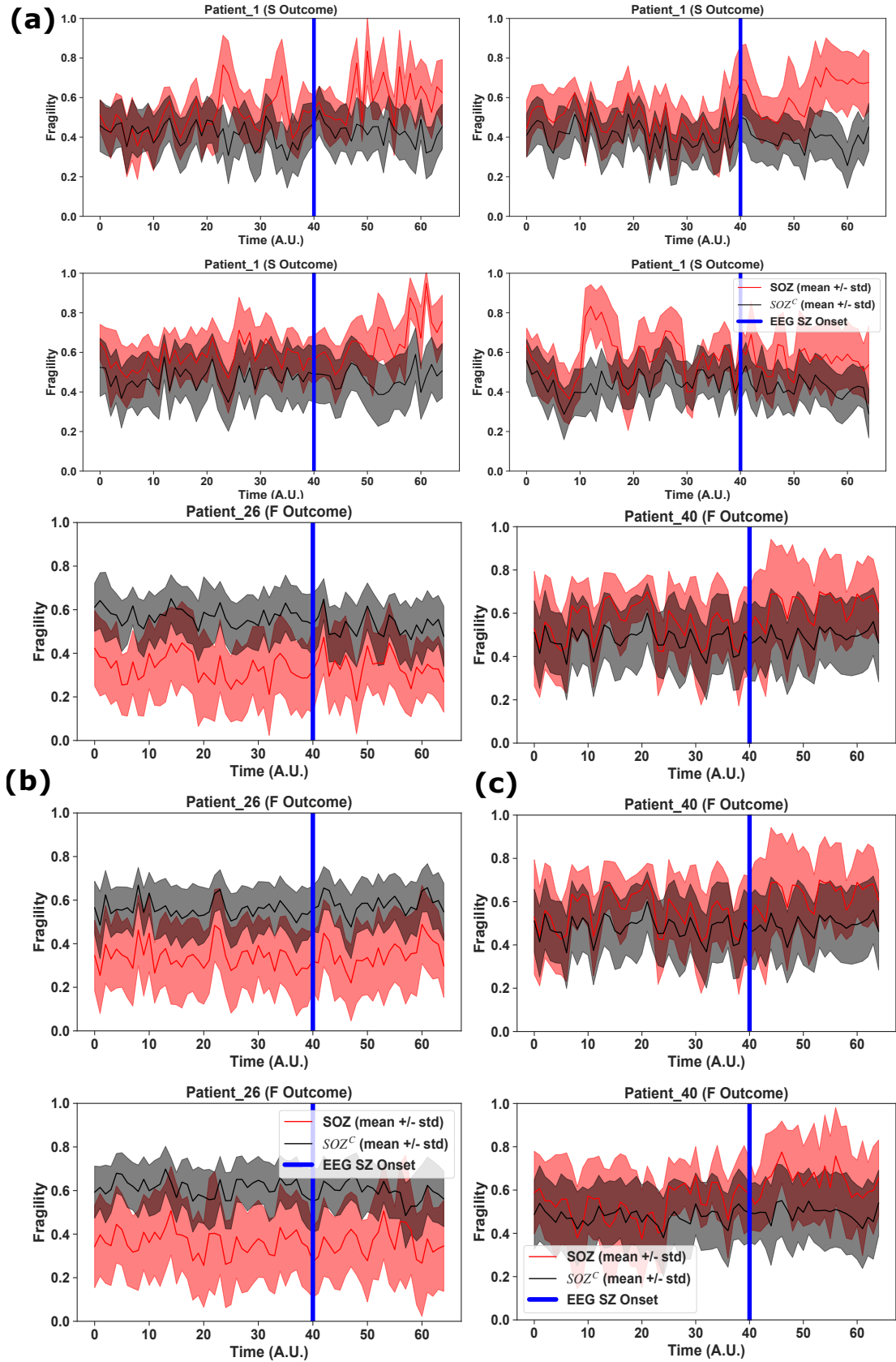


Figure 3-5. (Caption next page.)

Figure 3-5. Patient-specific SOZ vs SOZ^C neural fragility near seizure onset - Red SOZ vs black SOZ^C signals for patients presented in Figure ??: Patient_01 **(a)**, Patient_26 **(b)**, Patient_40 **(c)**. For each patient, the ictal snapshots available are visualized around seizure onset with 5 seconds before onset until the first 20% of the seizure. Not necessarily all electrodes in the clinically annotated SOZ are part of the EZ when the patient had a successful outcome. Therefore, if neural fragility had value in contrasting true EZ electrodes from non-EZ electrodes, then any extra electrodes clinically annotated in the SOZ should have relative lower fragility. The lines represent mean \pm sem.

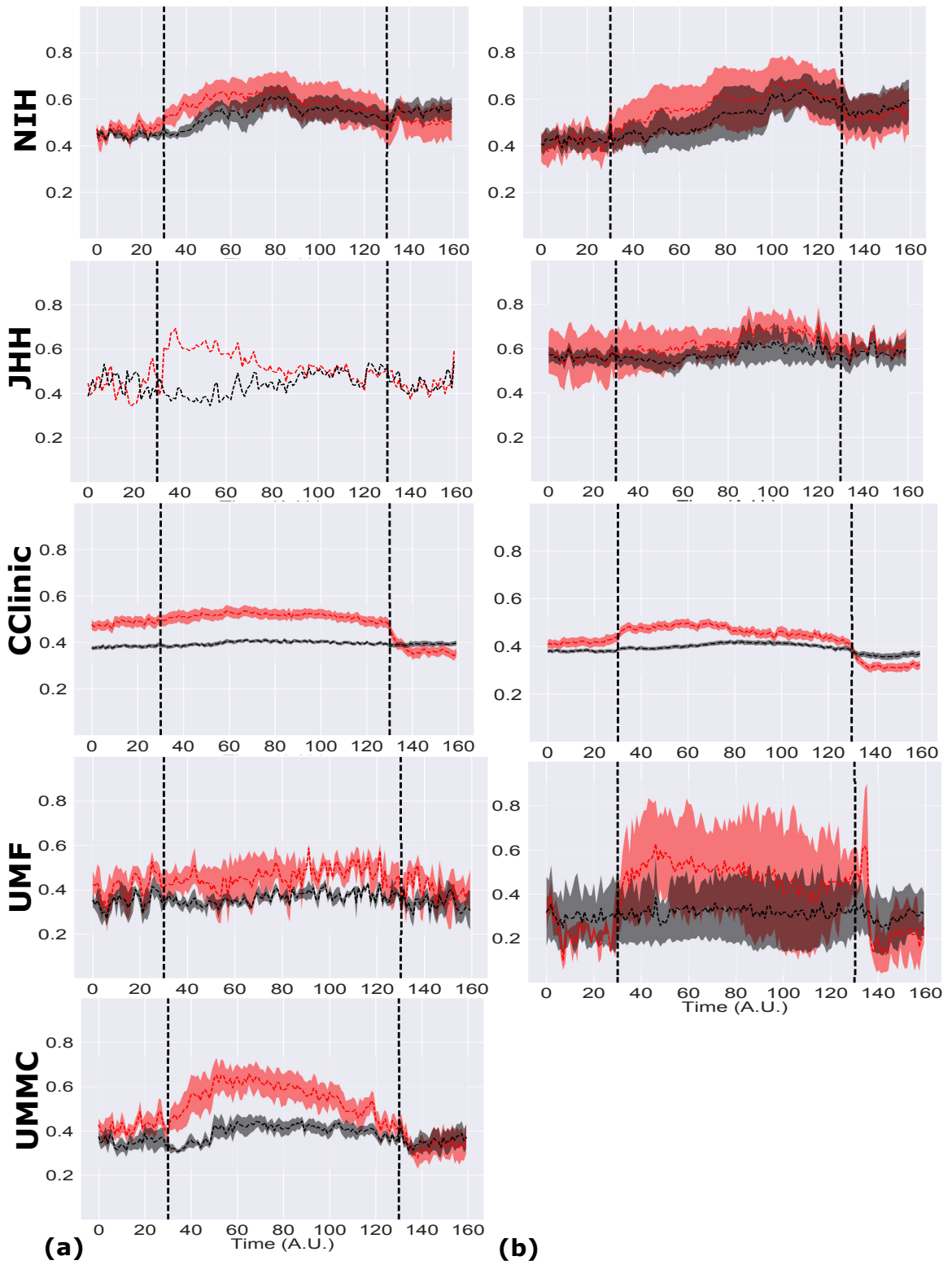


Figure 3-6. (Caption next page.)

Figure 3-6. Pooled-patient per clinical center SOZ vs SOZ^C neural fragility - Red SOZ vs black SOZ^C fragility signals for pooled patients within each of the five centers with successful **(a)** and failed outcomes **(b)** for NIH (n=14), JHH (n=4), CC (n=61), UMH (n=5), and UMMC (n=7) (top to bottom respectively). Note UMMC only had successful outcomes, so there was no curve for the failures. Seizure periods were resampled and normalized to 100 samples for averaging and viewing purposes. In JHH and UMH, there were only one and two patients in successful outcomes respectively. The lines represent mean \pm sem.

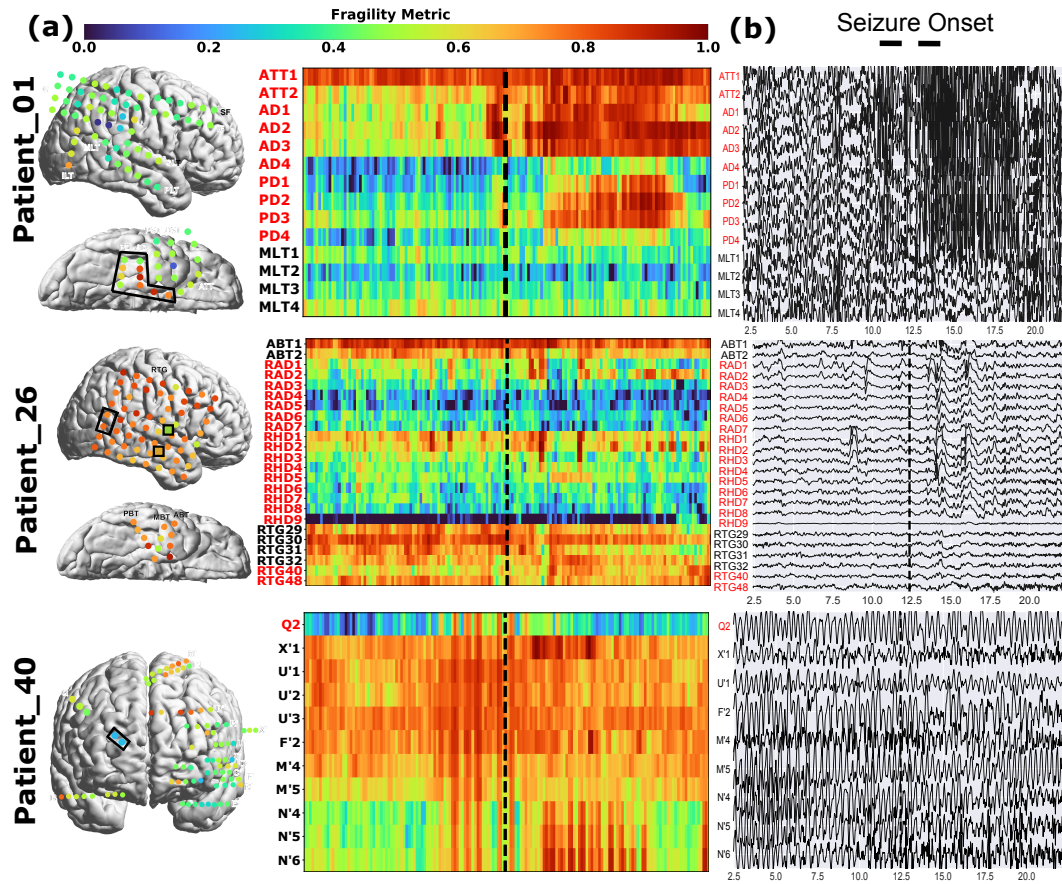


Figure 3-7. Fragility heatmaps, and corresponding raw EEG traces of successful and failed outcome patients. (a) From top to bottom, Patient_1 (success, NIH treated, CC1, Engel score 1), Patient_26 (failure, JHH treated, CC3, Engel score 4), and Patient_40 (failure, CClinic treated, CC4, Engel score 3) are shown respectively. The color scale represents the amplitude of the normalized fragility metric, with closer to 1 denoting fragile regions and closer to 0 denoting relatively stable regions. **(Left)** Overlaid average neural fragility value of each electrode in the window of analysis we used. Black dark squares represent a depth electrode that is not shown easily on the brain. Black lines outline where the clinicians labeled *SOZ*. Note in Patient_26, RAD and RHD electrodes are denoted by the squares with the color showing the average over the entire electrode. **(Right)** Clinically annotated heatmaps of the implanted ECoG/SEEG electrodes with red y-axis denoting *SOZ* contacts. The red contacts are also part of the surgical resection in these patients. Data is shown in the turbo colormap. Best seen if viewed in color. (b) Corresponding raw EEG data for each patient with electrodes on y-axis and time on x-axis with the dashed white-lines denoting seizure onset. Each shows 10 seconds before seizure onset marked by epileptologists, and 10 seconds after. EEG was set at a monopolar reference with line noise filtered out. Not all electrodes are visualized in the brain plot because channels that were deemed noisy, or in white matter were not included in analysis (for more information, see Methods Section). In addition, only a select set of channels are chosen for the heatmap and time-series for sake of visualization on a page and to demonstrate select channels that demonstrated different fragility values. Each EEG snapshot is shown at a fixed scale for that specific snapshot that was best for visualization, ranging from 200 μ V to 2000 μ V.

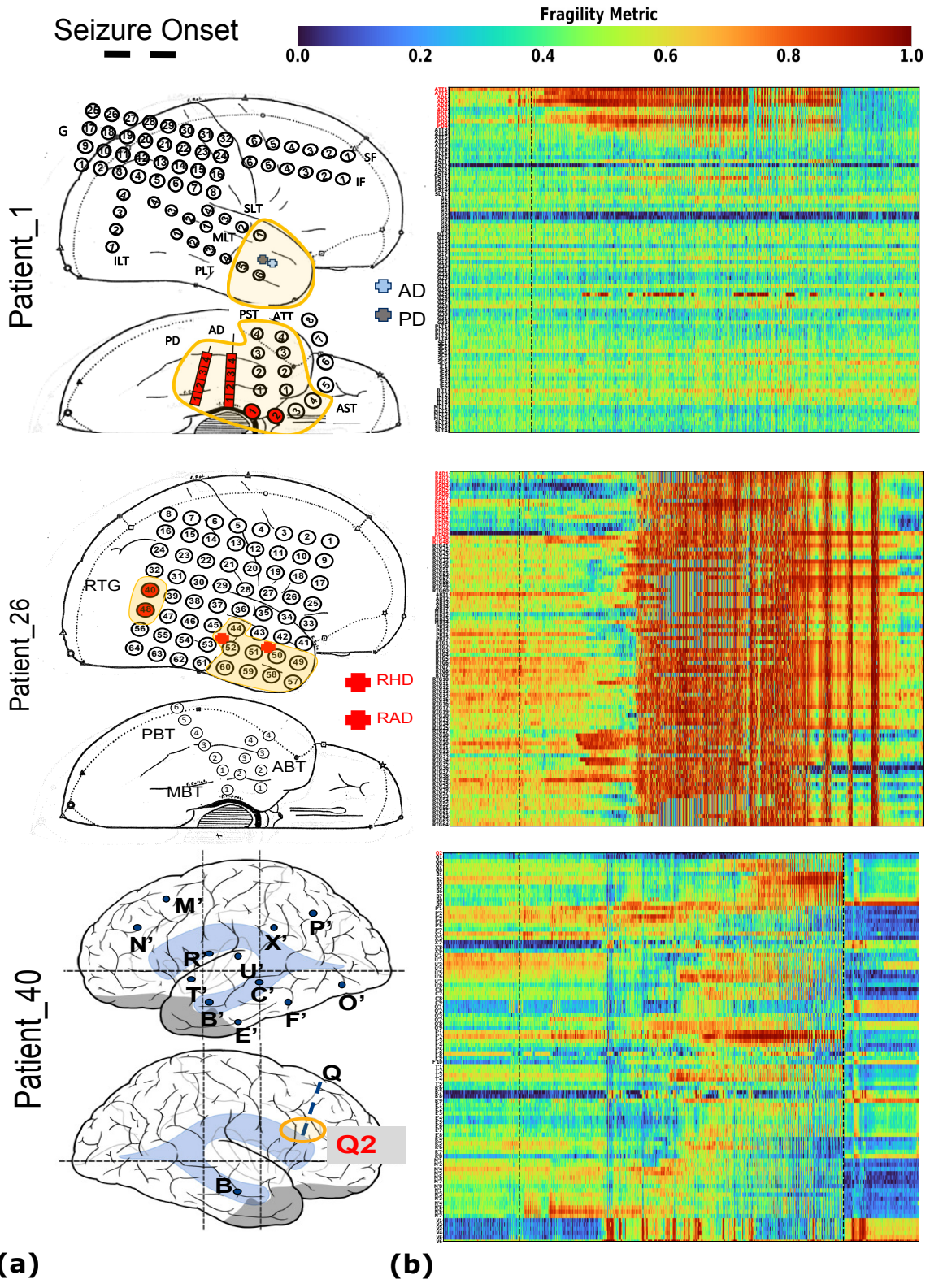


Figure 3-8. (Caption next page.)

Figure 3-8. Entire fragility heatmap of seizures in successful and failed surgical outcomes - Fragility heatmaps with electrodes on y-axis and time on x-axis with the dashed white-lines denoting seizure onset and offset. Shows a period of 30 seconds before seizure onset and 30 seconds after seizure offset. **(a)** Shows clinically annotated maps of the implanted ECoG/SEEG electrodes with red denoting SOZ contacts. **(b)** shows spatiotemporal fragility heatmaps for example of successful outcome (Patient_01), and failed outcome (Patient_26 and Patient_40). The color scale represents the amplitude of the normalized fragility metric, with closer to 1 denoting fragile regions and closer to 0 denoting relatively stable regions. The contacts in red and orange are part of the SOZ and RZ, respectively as defined in Methods section. Note that the red contacts are also part of the RZ. Within the seizures, estimating the linear systems are not as stable, which can be seen by fragility "everywhere" in the map. Visualized with Turbo continuous colormap. Best seen if viewed in color.

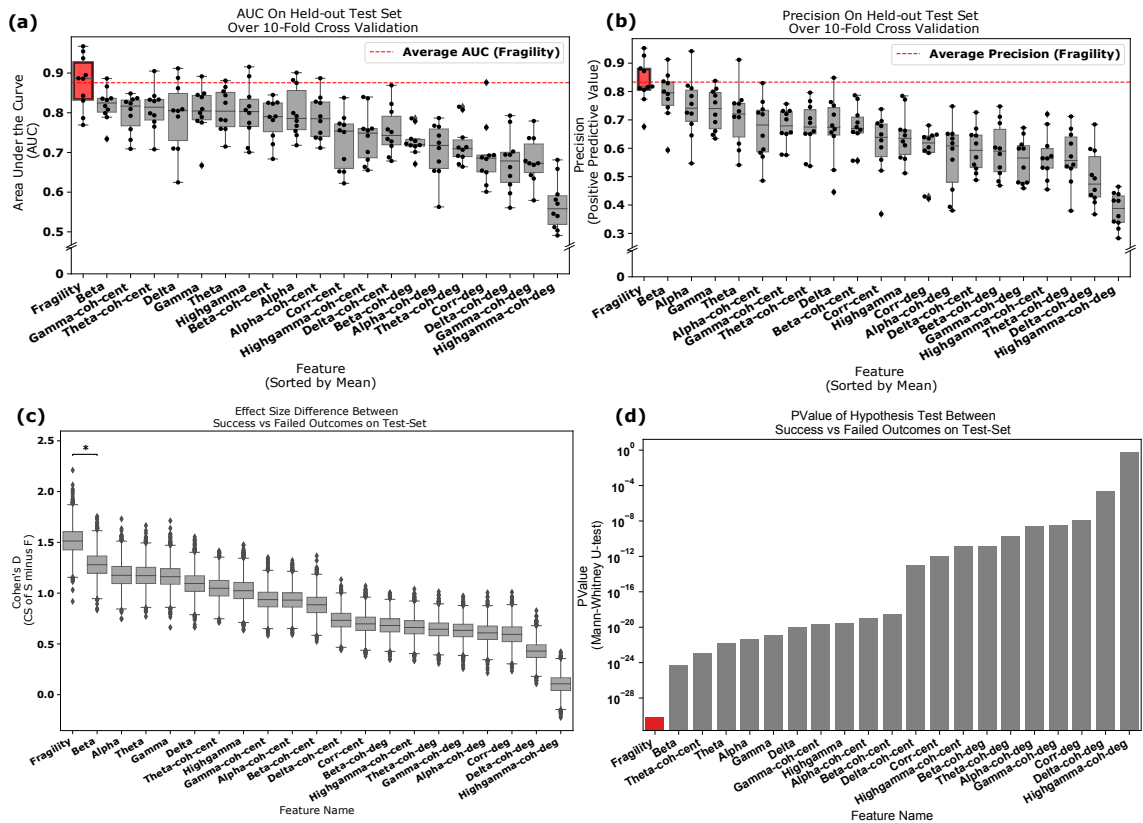


Figure 3-9. Area under the curve and average precision performance. Specific results for neural fragility are marked in red for each of the panels (a-d). **(a)** Discrimination plot (measured with AUC) shows the relative performance of benchmark feature representations compared to that achieved with neural fragility. Neural fragility has a median AUC of 0.89 (boxplot summary = 0.77, 0.97, 0.83, 0.93; min, max, first quartile, third quartile). **(b)** A similar average-PR curve shows the relative positive predictive value of all features compared with fragility. Average precision is the analogous area under the curve for the PR curve. Neural fragility has a median PR of 0.82 (boxplot summary = 0.68, 0.95, 0.81, 0.88; min, max, first quartile, third quartile). **(c)** A summary of the Cohen's D effect size measurements between the success and failed outcome distributions across all features. The effect size of neural fragility is significantly greater than that of the beta band (alpha = 0.05). Neural fragility has a median effect size of 1.51 (boxplot summary = 0.92, 2.21, 1.43, 1.60; min, max, first quartile, third quartile). **(d)** The corresponding PValues of the effect size differences between success and failed outcomes, computed via the one-sided Mann-Whitney U-test. Note that the samples in (c) are not shown for visual sake; data was approximately bell-curve shaped and a box plot adequately summarizes the main descriptive statistics of the distribution. For box plot summary statistics (min, max, median, first quartile and third quartile) of other features, see Supplemental Data Table for this figure.

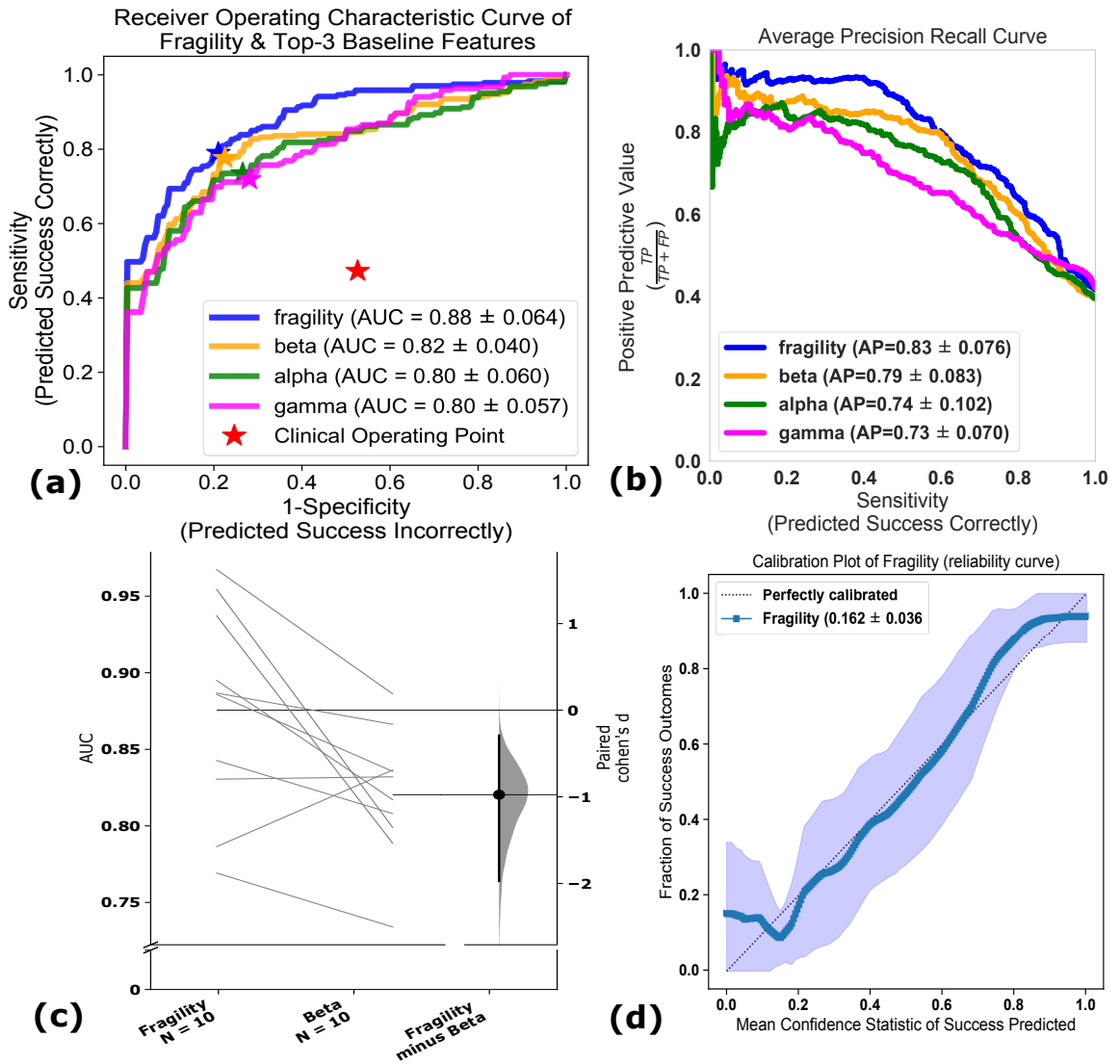


Figure 3-10. (Caption next page.)

Figure 3-10. Comparison of classification models using different features - (a)

The ROC curve over 10 folds of cross-validation of the held-out test set obtained by applying a Random Forest model onto the spatiotemporal heatmaps to predict surgical outcome (see Methods section). Fragility and the top-3 baseline features in terms of AUC are visualized. The shaded area represents the standard deviation of the curve obtained by linear interpolation for visualization purposes. The AUC of fragility obtained a 0.88 +/- 0.064 over the 10 standard deviation with a relative improvement of 7.2% improvement in AUC compared to the next best feature representation (i.e. the beta frequency band). At the Youden point (stars), neural fragility obtains a balanced accuracy score of 0.76 +/- 0.06, and an improvement of 0.32 in TPR and 0.32 in FPR compared to the clinical operating point (red star). **(b)** The average PR curve showing that fragility is better than the top 3 features by at least an average precision of 0.04. **(c)** A paired estimation plot showing how the same test set of patients differed in AUC depending on whether it was using the fragility, or beta feature heatmap representation. The paired Cohen's D effect size was computed at -0.975 (-1.97 to -0.29; 95% CI). The p-values associated with the difference between Neural Fragility and the Beta frequency band were 0.0204, 0.0273, and 0.0225 using the one-sided Wilcoxon rank-sum test, permutation test, and the paired student t-test respectively. **(d)** Calibration curve showing the fraction of actual successful surgical outcomes on the y-axis vs the average CS output on the x-axis. The curve measures how calibrated the predicted success probability values are to the true risk stratification of the patient population. The closer a curve is to the $y = x$ line, then the more calibrated a model is. It is quantified by the Brier-loss (closer to 0 is better), which is shown in the legend, and is significantly lower than the next best feature (an improvement of 15%). The shaded region represents 95% confidence interval of two standard deviations.

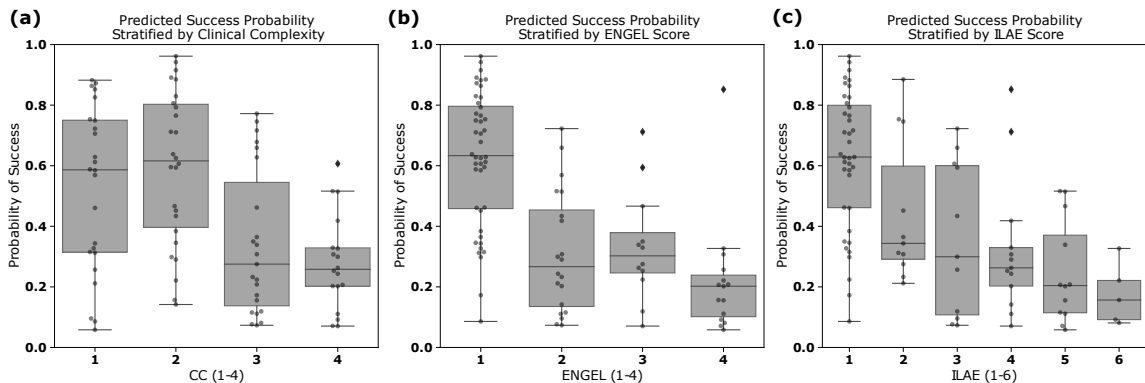


Figure 3-11. Neural fragility of patients stratified by clinical covariates. (a) Distribution of success probability values per patient stratified by clinical complexity (CC; see [Methods - Data collection](#)), where lesional (1) and temporal lobe epilepsy (2) patients have similar distributions because they are generally the "easier" patients to treat, whereas extratemporal (3) and multi-focal (4) have lower general probabilities because they are "harder" patients to treat. It is important to note that the classification experiment posed did not explicitly optimize this separation between clinical case complexities. There is a median predicted probability of success of 0.59 (boxplot summary = 0.06, 0.88, 0.31, 0.75; min, max, first quartile, third quartile) for CC 1. For CC2, CC3, and CC4, there is a median probability of success of 0.62 (boxplot summary = 0.14, 0.96, 0.40, 0.80), 0.28 (boxplot summary = 0.07, 0.77, 0.14, 0.55), and 0.26 (boxplot summary = 0.07, 0.61, 0.20, 0.33) respectively. (b) The distribution of the probability values per patient stratified by Engel score. Due to the AUC being high for fragility, it is expected that Engel I has high predicted probability of success, while Engel II-IV have lower success probability. However, the relative downward trend in the success probabilities from Engel II-IV indicated that neural fragility is present in the clinical *SOZ* in varying degrees from Engel II-IV, suggesting that it correlates with the underlying severity of failed outcomes. Engel IV has the lowest average predicted probability of success as expected. Engel I, II, III, and IV subjects had a median predicted probability of success of 0.63 (boxplot summary = 0.09, 0.96, 0.46, 0.80), 0.27 (boxplot summary = 0.07, 0.72, 0.14, 0.45), 0.30 (boxplot summary = 0.07, 0.71, 0.25, 0.38) and 0.20 (boxplot summary = 0.06, 0.85, 0.10, 0.24) respectively. (c) A similar distribution for another measure of surgical outcome, the ILAE score, where 1 are considered success and 2-6 are considered failure. Here, ILAE 2-5 follow a decreasing trend with ILAE-6 having the lowest average predicted probability of success. ILAE 1-6 has a median predicted probability of success of 0.63 (boxplot summary = 0.09, 0.96, 0.46, 0.80), 0.34 (boxplot summary = 0.21, 0.88, 0.29, 0.60), 0.30 (boxplot summary = 0.07, 0.72, 0.11, 0.60), 0.26 (boxplot summary = 0.07, 0.85, 0.20, 0.33), 0.20 (boxplot summary = 0.06, 0.52, 0.11, 0.37), and 0.16 (boxplot summary = 0.08, 0.33, 0.09, 0.22) respectively.

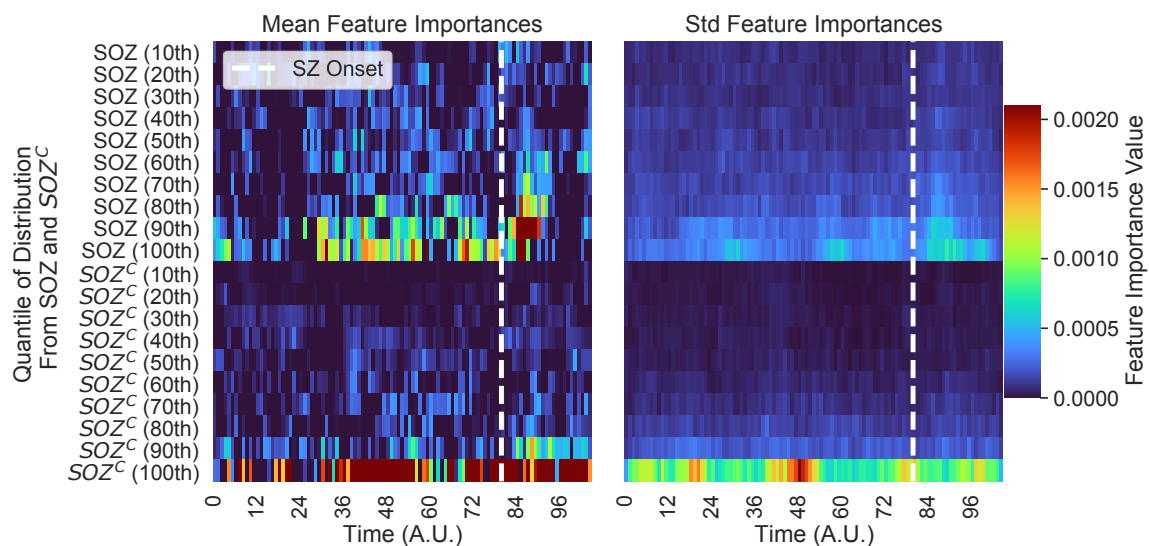


Figure 3-12. Estimated feature importance (mean and stdev) of the associated fragility heatmap used estimated using permutation - The metric of interest was the concordance statistic (i.e. AUC) of the ROC curve. The original feature map is transformed into a 20-dimensional set of time-varying statistics of its *SOZ* and *SOZ^C* electrodes describing the quantiles of the spatiotemporal heatmap (10% - 100% quantiles). This time-varying summary allows these heatmaps to be pooled together across subjects when training a Random Forest classifier as described in Methods section.

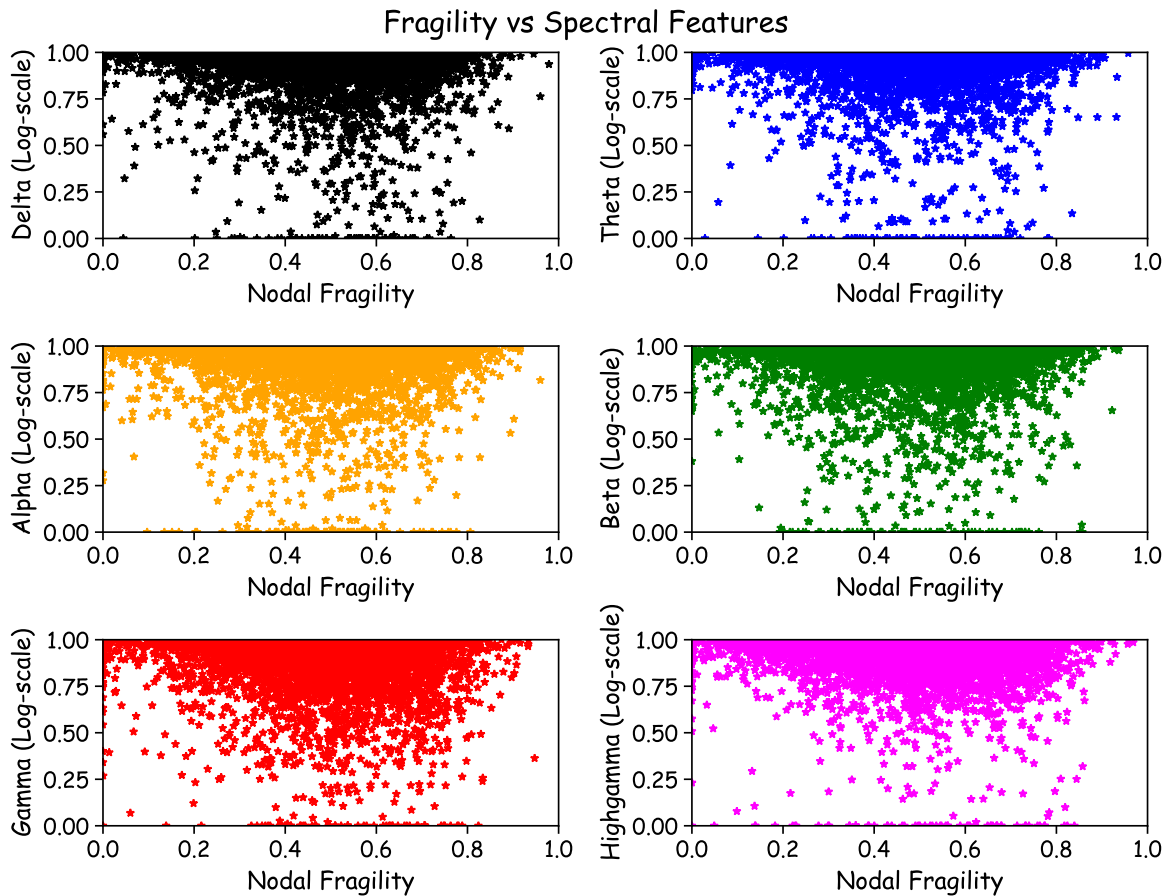


Figure 3-13. Neural fragility vs frequency power values - Fragility versus frequency power in the delta, theta, alpha, beta, gamma and highgamma band for Patient_01, Patient_26, and Patient_40. For band definitions, refer to ?? - ??. Every point represents the spectral power and neural fragility value from a randomly chosen window and electrode from one of the patients. No significant correlation is seen or computed from the data. Each spectral feature and fragility are normalized as described in Methods section.

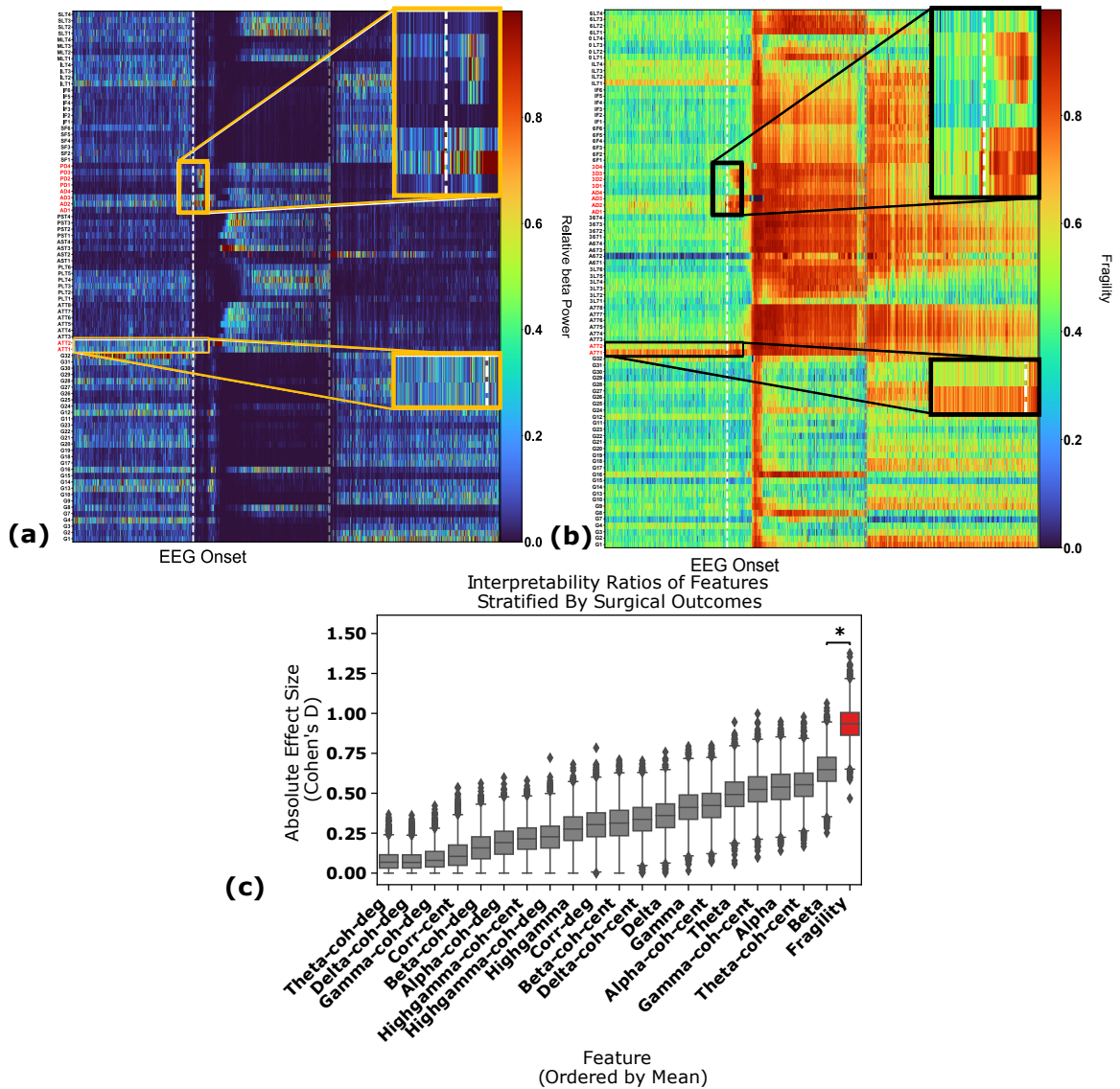


Figure 3-14. Interpretability ratio of feature heatmaps - (a) Two heatmap examples of a seizure snapshot of Patient_01 (NIH treated, ECoG, CC1, Engel I, ILAE 1) with the beta frequency band (left) and the neural fragility heatmap (right). Both colormaps show the relative feature value normalized across channels over time. The black line denotes electrographic seizure onset. **(b)** A box plot of the interpretability ratio that is defined in Results Section computed for every feature. The y-axis shows an effect size difference between the interpretability ratios of success and failed outcomes. The interpretability ratio for each patient's heatmap is defined as the ratio between the feature values in the two electrode sets ($\frac{SOZ}{SOZ^c}$). Neural fragility is significantly greater than the beta band (alpha level=0.05).

Chapter 4

Neural Fragility of the Intracranial EEG Network During Intraoperative and Postoperative Monitoring

Localizing the EZ is an ill-posed task as it is impossible to identify despite multimodal pre-operative assessments. The definition requires one to resect brain tissue and then verify that a patient is seizure-free to be certain that the EZ was correctly identified. In cases of seizure-freedom, it is impossible to be certain whether a smaller resection may have achieved similar outcomes. Clinicians typically have to wait 6-12 months (or more), to obtain accurate outcome measurements of a surgical resection in terms of an Engel score, or ILAE classification [11, 12].

If seizures reoccur, re-operations have increased risk of permanent postoperative neurological deficits [21], health-care costs are 32% higher than in patients with successful first-time surgeries [22], and the delay in surgery may lead to a more widespread seizure network and lesser likelihood of surgical success [23]. When localizing the EZ, the focus is typically on identifying the SOZ, the brain regions that initiate seizures, and the EPZ, the regions associated with early propagation of the seizure activity. This requires observation of the seizures. As a result, there are lengthy hospital stays and increased risks of complications [24, 25]. Interictal localization typically relies

on visual identification of "epileptic signatures", such as beta-buzz, high-frequency oscillations, or interictal spiking [26–28]. This requires clinicians to visually inspect intracranial electroencephalography (iEEG) data where they attempt to identify abnormalities in the iEEG channels that may correlate to the *SOZ*. Unfortunately, this task is challenging to even the most experienced clinicians because epilepsy is fundamentally a network disease, which cannot be entirely defined by the current methods of localization. Due to imprecise EZ localization, healthy neural tissue may be included within resection margins potentially resulting in avoidable neurological deficit [Gonzalez-Martinez2007, Yardi2020LongtermSurgery, Tellez-Zenteno2005, Spencer2008OutcomesChildren, McIntosh2012]. Furthermore, surgical resection may yield poor outcomes in the most challenging cases with success rates varying between 30-70% [Engel2012a].

Several localization algorithms have been proposed to better leverage iEEG recordings to localize the EZ. Many entail investigations of the spectral power in each iEEG channel, including high frequency oscillations (HFOs) [Gliske2015]. However, these approaches do not consider network properties of the brain because they treat each EEG channel independently. Others have proposed graph-based analysis of iEEG [43–45, 59, 80, 110], but these approaches fail to identify internal network properties that cause seizures to occur in the first place. Moreover, underlying graph and connectivity structure is typically not observed, but estimated from data. These methods define a connectivity function based on methods such as Pearson correlation [59], or coherence [43]. However, any noise in the estimation procedure can drastically alter the underlying graph metrics, such as centrality, or degree. In [47], it is shown that that graph measures are not unique to a graph. Many graphs have the same degree distribution but are completely different graphs.

There is an unmet need to develop more robust biomarkers of the EZ in order to determine the extent of a resection, thereby optimizing the surgical outcome, while

limiting the amount of brain tissue removed. The presence of a robust biomarker could facilitate and expand the utility of intraoperative electrocorticography. One surgical strategy could involve an incremental procedure whereby electrocorticography is leveraged to guide the extent of resection. At present, electrocorticography is limited to the detection of interictal discharges, with limited utility. A biomarker that leverages interictal data, resilient to anesthetic effect and specific to the EZ would significantly advance surgical approaches for focal epilepsy.

Recently, it was proposed that neural fragility, a structured perturbation of a networked dynamical system estimated from iEEG ictal data has the potential to be a robust biomarker of the EZ [81, 111]. This model is dynamic, based on a robust least-squares estimate [82, 112] and models intrinsic stability properties of the system. That is, the propensity for seizures in our model occur as a property of eigenvalue perturbations.

In this study, we evaluate neural fragility as a correlate of surgical outcome using pre and post resection iEEG interictal recordings of the same subjects. We hypothesize that neural fragility of the brain network will decrease in cases of successful surgical resection. In iEEG data, neural fragility will modulate with respect to the surgical outcome, increasing, or staying the same after resection in the context of residual epileptic tissue, and decreasing after resection if the procedure was successful. We first test this hypothesis by using a virtual in-silico environment to simulate various scenarios of failed and successful resections. Using The Virtual Brain (TVB) simulation platform and a virtual epileptic patient model, we simulate possible resective scenarios, and compute neural fragility of the simulated pre/post resection recordings. We demonstrate that neural fragility decreases overall in the iEEG network when resections are successful, but stays the same, or increases when resections do not capture the EZ. We then further validate this hypothesis with a dataset of 6 patients (5 success and 1 failure outcome) selected from the Hospital for Sick Children (HSC),

and find that fragility significantly increases after a failed resection, while it decreases significantly after all successful resections. Since we are analyzing interictal data, we also compute HFOs using a root-mean square (RMS) detector. We demonstrate that neural fragility predicts outcome better compared to more established frequency band power, or HFOs. Our results suggest that a networked-dynamical biomarker, neural fragility, may be helpful in predicting surgical outcome and extent of the resected area using pre and post-resection iEEG recording data. This can potentially improve surgical success rates and allow clinicians to incrementally operate on the EZ thereby limiting the amount of brain tissue needed to be resected for the patient to be seizure free.

Methods - Dataset and Code

Ethics Statement

Decisions regarding the need for invasive monitoring and the placement of electrode arrays were made independently of this work and part of routine clinical care. All data were acquired with ethics approval from the Research Ethics Board (REB) at the Hospital of Sick Children. The acquisition of data for research purposes was completed with no impact on the clinical objectives of the patient stay.

Data availability

Due to the unique nature of the data from the hospital for Sick Children and HIPAA concerns, the dataset cannot be made publicly available. Instead the data is available upon request from the clinical co-authors. In addition, the TVB dataset used in simulations is accessible upon request from Marseille University.

Code availability

Code used for reproducing the figures and running parts of the analysis are at <https://github.com/adam2392/sickkids>. We include a jupyter notebook written in Python to help reproduce figures. We also include jupyter notebooks that were used to run analysis, when applied to the raw data can reproduce the analyses.

The Hospital for Sick Children

iEEG extraoperative, intraoperative and postoperative data from 7 DRE patients who underwent intracranial EEG monitoring between January 2017 and December 2019, which included electrocorticography (ECoG) were collected from The Hospital for Sick Kids (HSC). One patient (E2) was excluded from analysis because the post-resection iEEG used a different implantation,

HSC Data were recorded using either a Nihon Kohden (Tokyo, Japan) acquisition system with a sampling rate of 2000 Hz. Signals were referenced to a common electrode placed subcutaneously on the scalp, on the mastoid process, or on the subdural grid. The time of seizure onset was indicated by a variety of stereotypical electrographic features which included, but were not limited to, the onset of fast rhythmic activity, an isolated spike or spike-and-wave complex followed by rhythmic activity, or an electrodecremental response. We discarded electrodes from further analysis if they were deemed excessively noisy by clinicians, recording from white matter, or were not EEG related (e.g. reference, EKG, or not attached to the brain).

All patients underwent neuropsychological assessment prior to invasive monitoring, which included measures of Full-Scale intelligence quotient (IQ), verbal comprehension, visual spatial reasoning, visual fluid reasoning, working memory, and visual processing speed using the Wechsler Intelligence Scale for Children (WISC-V) and the corresponding WISC-V sub-tests. Verbal memory was indexed by a child's overall performance

in delayed free recall using the Children’s Memory Scale (CMS), Children’s Auditory Verbal Learning Test-2 (CAVLT-2), or the Child and Adolescent Memory Profile (ChAMP) [113]. Visual memory was indexed by the delayed free recall using the CMS. The FSIQ scores for each patient can be found in Table 1. Detailed neuropsychological profiling may be found in Supplementary Table 1.

We define successful outcomes as seizure free (Engel class I and ILAE scores of 1 and 2) at 12+ months post-op and failure outcomes with seizure recurrence (Engel classes 2-4) [85].

The Virtual Brain Data

We also used a single virtual epileptic patient for our simulation analysis with The Virtual Brain. One patient from [66] were used. Neuroimaging data, and specifically diffusion MRI were collected for these subjects and a full connectivity dataset was constructed that would allow TVB simulations. All acquisition information for those subjects can be found in their respective references. We list all patients metadata used in this paper in the Supplementary table. Details on the imaging and implantation data to instantiate the virtual epileptic patient are presented in Supplementary Materials.

Methods - Analysis

iEEG Data Preprocessing

Data was initially stored in the form of the European Data Format (EDF) files [114]. We preprocessed data into the BIDS-iEEG format and performed processing using Python3.6, Numpy, Scipy, MNE-Python and MNE-BIDS [78, 93, 94, 98, 115–117].

Every dataset was notch filtered at 60 Hz and its corresponding harmonics (with a cutoff window of 2 Hz), and bandpass filtered between 0.5 and the Nyquist frequency with a fourth order Butterworth filter. If correlated noise was present, a common

average reference was applied. EEG sequences were broken down into sequential windows and the features were computed within each window (see 4 for details). Values at each window of time were normalized across electrodes to values that could range from 0 up to at most 1, to allow for comparison of relative feature value differences across electrodes over time; the higher a normalized feature, the more we hypothesized that electrode was part of the EZ [81, 111]. This normalization scheme allows us to account for how relatively different channels are in terms of the proposed metric relative to other channels over time.

Channels with significant artifact were excluded. Artifact-free data segments of equal length were selected pre and post resection of the epileptogenic zone. As part of the surgical resection, certain channels were disconnected to allow the surgeons to get at certain tissue. These channels are represented as "NaN" recordings. Moreover, since surgical resection occurs, post-resection recordings will have then less channels compared to their pre-resection counterparts.

Neural Fragility Analysis

It is a concept based on the conjecture that focal seizures arise from a few fragile nodes, i.e., the , which renders the cortical epileptic network on the brink of instability. When one observes iEEG data during interictal, or preictal periods, activity recorded from each channel *appears* to hover around a baseline value. If the network is "balanced", then it will respond transiently to an impulse, but always returns to a baseline value. In contrast, when one observes iEEG data during a seizure event, activity (i) grows in amplitude, (ii) oscillates, and (iii) spreads in the brain when the network is perturbed. This is a consequence of an "unbalanced" network that does not return to a baseline value. From a dynamical systems perspective, the iEEG network has switched from a stable (non-seizure) to an unstable (seizure) network.

Biologically, imbalance due to perturbations between excitatory and inhibitory

connections of a neural network can occur through any number of mechanisms, such as elevated glutamate [102, 103, 118–122], genetic disorder impacting synaptic inhibition [104], decreased GABA [105], inclusion of axo-axonic gap junctions [106], loss of inhibitory chandelier cells [107], or axonal sprouting from layer V excitatory pyramidal cells [108]. This imbalance within a neural network may lead to functional instability, where impulse perturbations in certain nodes lead to recurring seizures. While iEEG cannot distinguish between excitatory and inhibitory neuronal populations, the concept of imbalance causing the network to be on the brink of instability can be modeled by neural fragility at the iEEG network level.

When one observes iEEG data during interictal, or preictal periods, activity recorded from each channel is noisy and hovers around a baseline value. In contrast, when one observes iEEG data during a seizure event, activity (i) grows in amplitude, (ii) oscillates, and (iii) spreads in the brain. From a dynamical systems perspective, the iEEG network has switched from a stable (non-seizure) to an unstable (seizure) network. Our conjecture is that small changes in connection strengths at EZ nodes cause an imbalance in inhibitory and excitatory connectivity between brain regions. Either inhibition is decreased and/or excitation is increased; thus, if the A is perturbed then over excitation can occur manifesting in a seizure.

Time Frequency Representation Analysis

We computed HFOs using a variety of methods. HFOs were computed using `mne-hfo`, an open-source Python implementation of HFO detection algorithms [123]. The root mean-squared (RMS) detector is used [49, 124, 125]. We defined HFOs as the union of ripples (80-250 Hz) and fast ripples (250-500 Hz) as detected by the RMS detector.

We also constructed frequency-based features from frequency bands of interest by applying a multi-taper Fourier transform over sliding windows of data with a window/step size of 2.5/0.5 seconds [43]. We required relatively longer time windows

to accurately estimate some of the lower frequency bands. Each EEG time series was first transformed into a 3-dimensional array (electrodes X frequency X time), and then averaged within each frequency band to form six different spectral feature representations of the data. We break down frequency analysis as follows:

1. Delta Frequency Band [0.5 - 4 Hz]
2. Theta Frequency Band [4 - 8 Hz]
3. Alpha Frequency Band [8 - 13 Hz]
4. Beta Frequency Band [13 - 30 Hz]
5. Gamma Frequency Band [30 - 90 Hz]
6. High-Gamma Frequency Band [90 - 300 Hz]
7. HFO = R & FR [80-250 Hz & 250-500 Hz]

The Virtual Brain Patient-Specific Modeling

TVB is a neuroinformatics platform used in the simulation of whole-brain neural dynamics. It incorporates biologically realistic computational models and simulation of brain network dynamics using connectome-based approaches and directly linking them to various brain imaging modalities [66, 67, 69, 126]. We use the resting-state Epileptor model, designed to simulate resting state interictal activity. We set a region to be EZ, with the rest normal and then measure the iEEG output of the TVB model. This data consists of the pre-resection simulation. Afterwards, we simulate data from three resective scenarios that fully captures the EZ, partially captures the EZ, or completely fails to capture the EZ. To simulate a resection of a region, we removed the connections of that region to all other regions and then generated the resulting iEEG data.

SEEG electrodes were implanted in the regions suspected to be in the EZ. Each electrode had 10–15 contacts (length: 2 mm, diameter: 0.8 mm, contacts separation:

1.5 mm). To determine electrode positions, an MRI was performed after electrodes implantation (T1 weighted anatomical images, MPRAGE sequence, TR = 1900 ms, TE = 2.19 ms, $1.0 \times 1.0 \times 1.0 \text{ mm}^3$, 208 slices) using a Siemens Magnetom Verio 3T MR-scanner. To reconstruct patient specific connectomes (DTI-MR sequence, angular gradient set of 64 directions, TR = 10.7 s, TE = 95 ms, $2.0 \times 2.0 \times 2.0 \text{ mm}^3$, 70 slices, b weighting of 1000 s/mm^2 , diffusion MRI images were also obtained on the same scanner. The study was approved by the Comité de Protection (CPP) Marseille 2, and all patients signed an informed consent form.

To quantify the proximity and number of tracks between electrodes, structural and diffusion MRI data were obtained via a processing pipeline to derive individualized cortical surface and large-scale connectivity. Cortical and subcortical surfaces were reconstructed along with volumetric parcellations using the Desikan–Killiany atlas, with the cortical regions subdivided in four (280 cortical regions and 17 subcortical regions). We obtained electrode positions by coregistering the parcellation with the MRI scan, and assigning each contact to the region containing most of the reconstructed contact volume. To compute the number of tracks between electrodes, head-motions and eddy-currents were corrected in diffusion data. Fiber orientation was estimated with constrained spherical deconvolution, and 2.5×10^6 streamlines were obtained by probabilistic tractography. We used the anatomically-constrained tractography (ACT) and the spherical-deconvolution informed filtering of tractograms (SIFT) frameworks to improve reproducibility and biological accuracy. The number of tracks between two pairwise electrodes was then obtained by summing the number of tracks whose extremities belong to the corresponding pairwise brain regions.

We utilize the Epileptor model, where it was originally designed to produce realistic seizure dynamics [Jirsa2014]. We specifically, use an extension of the original Epileptor model, called the resting-state Epileptor, which is capable of reproducing interictal spikes [Courtiol2020DynamicalEpilepsy]. The resting-state Epileptor

equations are as follows:

$$\dot{x}_{1,i} = y_{1,i} - f_1(x_{1,i}, x_{2,i}) - z_i + I_{ext1,i} \quad (4.1)$$

$$y_{1,i} = \frac{1}{\tau_1}(1 - 5x_{1,i}^2 - y_{1,i}) \quad (4.2)$$

$$\dot{z}_i = \frac{1}{\tau_0}(4(x_{1,i} - x_{0,i}) - z_i - K_s \sum_{j=1}^N C_{ij}(x_{1,j} - x_{1,i})) \quad (4.3)$$

$$\dot{x}_{2,i} = -y_{2,i} + x_{2,i} - x_{2,i}^3 + I_{ext2,i} + 0.002g(x_{1,i}) - 0.3(z_i - 3.5) \quad (4.4)$$

$$y_{2,i} = \frac{1}{\tau_2}(-y_{2,i} + f_2(x_{1,i}, x_{2,i})) \quad (4.5)$$

$$\dot{x}_{3,i} = d(-x_{3,i}^3 + 3x_{3,i}^2 + y_3 + K_{rs} \sum_{j=1}^N C_{ij}(x_{3,j} - x_{3,i})) \quad (4.6)$$

$$y_{3,i} = d(-10x_{3,i} - y_{3,i} + a) \quad (4.7)$$

where

$$f_1(x_1, x_2) = \begin{cases} x_1^3 - 3x_1^2 & \text{if } x_1 < 0 \\ (-m + x_2 - 0.6(z - 4)^2)x_1 & \text{if } x_1 \geq 0 \end{cases}$$

$$f_2(x_1, x_2) = \begin{cases} 0 & \text{if } x_2 < -0.25 \\ 6(x_2 + 0.25) & \text{if } x_2 \geq -0.25 \end{cases}$$

$$g(x_1) = \int_{\tau_0}^{\tau} e^{-\gamma(t-\tau)} x_1(\tau) d\tau$$

The output that is measured in the original Epileptor model is the LFP, defined as $x_2 - x_1$. In the resting-state Epileptor model, the output is defined as a convex combination of the fast and intermediate subpopulation activity and the resting-state subpopulation activity.

$$Y = p_i(-x_{1,i} + x_{2,i}) + (1 - p_i)x_{3,i}, \quad 0 < p_i < 1 \quad (4.8)$$

The i indexes the N discrete brain regions (i.e. 84 brain regions in a Desikan-Killiany atlas). Here, the x_1, y_1 variables correspond to the fastest time scale accounting

for low-voltage fast discharges (i.e. very fast oscillations). The x_2, y_2 variables correspond to an intermediate time scale accounting for spike-and-wave discharges. The z slow-permittivity variable corresponds to the slowest time scale, responsible for autonomously switching between interictal and ictal states in the form of a direct current (DC) shift [Ikeda1999FocalRecording, Vanhatalo2003VeryDC-EEG, Jirsa2014]. This variable takes the system through saddle-node and homoclinic bifurcations for seizure onset and offset respectively. The x_3, y_3 variables account for transient behavior, in the form of spindle-like patterns, which added allow the Epileptor model to reproduce resting-state oscillatory wave patterns and also reproduce interictal spikes. The x_0 serves as a hyperparameter, denoting the degree of epileptogenicity of a brain region. If x_0 is greater than a critical value, of -2.05, then the brain region can trigger seizures autonomously. Otherwise, it is in an equilibrium state. The a hyperparameter relative to the critical value of -1.74, also represents the degree of epileptogenicity during the interictal resting state. The C_{ij} are the weights based on the subject’s structural connectivity matrix and K_s, K_{rs} are the respective large-scale scaling parameters of the connectivity weights in the seizure and resting-state subpopulations. Note that $C_{ij} = 0, \forall i = j$ because we assume that the neural mass model of one brain region already accounts for internal connectivity effects. The interictal and preictal spikes occur when these variables are excited by the fast oscillation system via the coupling term, $g(x_1)$. The characteristic frequency rate d , fixed to 0.02, sets the natural frequency of the third subsystem (10 Hz), the most powerful frequency peak observed in electrographic recordings at rest [LopesDaSilva1997AlphaModels, Buzsaki1992High-frequencyHippocampus]. For more detailed discussion on the Epileptor and extensions, see [Jirsa2014, Courtiol2020DynamicalEpilepsy, Houssaini2020TheBlock].

In our system, we set a range of x_0 value combinations for the EZ and propagation regions, with $x_0 = -2.10$ for the clinically hypothesized EZ region. Then $x_0 = -2.35$

was set for the normal region for all simulations. Our goal here is to match the real data situation as closely as possible, where we are not comparing seizures, but resting-state iEEG activity. The a variable is set to -1.74. Finally, $p_i = 0.2$. We set EZ regions based on what the clinicians thought for this patient. The other parameters, $\tau_0 = 4000$; $\tau_2 = 10$; $K_s = -5$; $\gamma = 0.01$ and then the rest of the parameters were set as in [Jirsa2017].

The system of stochastic differential equations were solved using an Heun Stochastic integration scheme with an integration step of 0.05, which gave values of the local field potentials in 4.8. To start the simulation at a realistic point, initial conditions were computed and stored for each simulation using a burn-in period of 15 seconds. Simulations were 30 seconds long afterwards. Additive white Gaussian noise was introduced into the variables x_2 and y_2 with mean 0 and variance of 0.0005 and to x_3 with a mean of 0 and variance of 0.0001. Additionally, observational colored noise was added to the iEEG simulated data with a mean of 0 variance of 1.0 and noise correlation (i.e. color) in time of 0.1. The iEEG data was modeled using a forward solution that uses an inverse gain mean-field model from the LFP. The details of which are described in [Jirsa2017].

To simulate a "virtual" resection, we took the actual clinical resection performed, and "removed" those regions in the structural connectivity matrix for that patient. This corresponded to "zeroing" out those rows and columns for that brain region, simulating the removal of that region. When we remove these brain regions, we also virtually removed the corresponding iEEG channels in those brain regions. We then used the above setup to simulate neural dynamics and corresponding iEEG activity pre and post resection. Afterwards, these snapshots of data can be analyzed using neural fragility as described in [Neural Fragility Analysis](#). They are then compared as described in [Statistical Analysis](#).

Statistical Analysis

To compare pre and post resection data, we computed Cohen’s D effect size differences between the feature representations of these two data sessions. We use the Mann-Whitney U test and K-Sample MANOVA test to compute a PValue with α Type I error rate set to 0.05. The distance function utilized in the K-Sample MANOVA is the distance correlation function, which is a more robust version of Pearson correlation [127]. The null hypothesis of our experimental setup was that the pre resection metrics came from the same population as the post resection. The alternative hypothesis was that the populations were different.

Since the feature representation heatmaps (i.e. neural fragility spatiotemporal heatmap) show a metric over time of all the recorded channels, samples are not necessarily independent. To account for correlations in time, we use a contiguous bootstrapping procedure to estimate the Cohen’s D and PValues with $n=100$ bootstrap samples. That is the typical bootstrap algorithm is carried out along the time-axis. Each bootstrap sample in time consists of all the channels, along with a small window of 10 samples (i.e. about 1 second). Then these bootstrap samples are compared between the pre and post resection heatmaps, generating a bootstrap distribution with a reported mean and standard deviation with 95% confidence intervals typically reported.

Results

In this work, we analyze pre and post resection iEEG data and compute neural fragility of the iEEG network to compare the changes in fragility stratified by the actual surgical outcome (see Figure 4-1). iEEG provides high temporal resolution data that enables clinicians to visually detect abnormal activity, such as spikes and high frequency bursts, in between seizures (interictal) and during seizures (ictal).

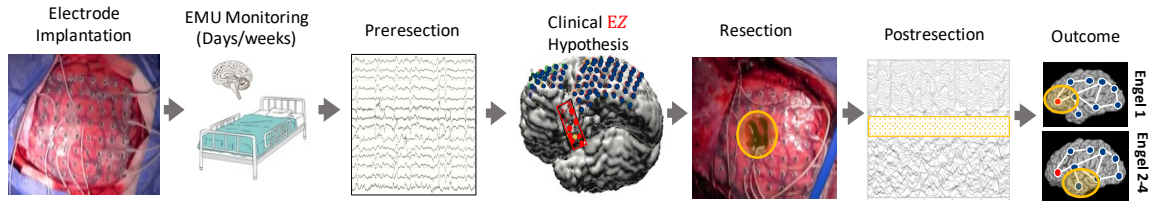


Figure 4-1. Clinical workflow with continuous iEEG monitoring before and after a surgical resection An overview of the DRE treatment clinical procedure. Patients are accepted into the Epilepsy Monitoring Unit (EMU) and implanted with intracranial electrodes to undergo monitoring. They are typically in the EMU for many days, up to a few weeks. Pre-resection iEEG data is used to form a clinical EZ hypothesis (red circled region). The clinical EZ is an estimate of the true EZ, and may contain the EZ, or not at all. Based on the clinical EZ hypothesis, a surgical resection is subsequently performed to remove that region of the brain (orange circled region). This is evaluated post-hoc (i.e. after the surgery is completed), which is why the EZ is difficult to define. There is not clinical biomarker that can define the EZ prospectively, thus the patient outcome after resections determine if clinicians successfully localized the EZ. Immediately afterwards in these patient recordings, post-resection iEEG data is recorded. Patients have followups 12+ months later to determine the actual outcome of the surgical treatment and whether the true EZ was successfully removed. The outcome of the patient is then measured in terms of Engel scores, where I is seizure free, and II-IV represent increasing levels of post-op seizure severity.

Moreover, intraoperative data may refine and modify the resection plan in real-time, by capturing primarily interictal data to study electrophysiological changes within the irritative zone following resection [25, 128, 129]. To extend our work in [81] and [111], we first provide some theoretical analysis of neural fragility to demonstrate that it is a well-defined metric assuming we have a good estimator for the linear system from data. Now that we have a well-defined metric, we hypothesize that neural fragility of iEEG data will modulate with respect to the successful surgical resection of the EZ.

To test this hypothesis, we use TVB to generate simulated iEEG data from real patient diffusion tensor imaging (DTI) connectomes, and show how neural fragility modulates with proposed complete, partial and incomplete resections of the EZ. We then demonstrate that neural fragility modulates pre and post resection in DRE patients that underwent surgical resection at HSC. A neurosurgical procedure at HSC collects intraoperative iEEG using the same chronically implanted electrodes

used for extraoperative mapping. These data facilitate resective epilepsy surgery by allowing one to observe the iEEG network while a surgery takes place. Intraoperative electrocorticography (ECoG) monitoring in [128] allows real-time monitoring of the brain and allows for post-resection recordings that from electrodes sampling the identical brain regions. Thus, clinically, one could monitor the patient for a brief period of time after resective surgery to determine if there are any recurring seizures, or epileptic activity [25, 130]. If one has a proposed marker for the underlying EZ, the model can be validated continuously throughout the operation. This provides a distinct advantage over the classical "resect and wait" retrospective datasets because we have access to post-resection recordings [25, 128].

Finally, we analyze every HSC patient's iEEG using 7 other frequency-based benchmark features, resulting in spatiotemporal heatmaps for every feature. The baseline features include spectral power in various frequency bands (e.g. delta band 1-4 Hz) and HFOs computed via an root mean-square (RMS) detector. We consider all of these as potential EEG representations of the epileptic network to see if they correlate with surgical outcome based on pre and post resection data.

Neural fragility of an iEEG network

Neural fragility is a concept based on the conjecture that focal seizures arise from a few fragile nodes, i.e., the EZ, which renders the epileptic network on the brink of instability. In [111], neural fragility is introduced in the context of "balanced" and "imbalanced" networks. Balanced networks respond transiently to an impulse, returning to baseline values, whereas imbalanced networks respond to an impulse with electrical activity that grows in amplitude, oscillates and spreads in the brain. From a dynamical systems perspective, the epileptic iEEG network is an unstable network (capable of seizing). Neural fragility of a node in the epileptic network is defined as the minimum amount of perturbation on the network structure required to move

the system from a stable to unstable state. This specific perturbation can take on a variety of forms. In [111], a column perturbation (modifying the outgoing connections of one node) was applied for *EZ* localization. In this work, we further this notion and use a row perturbation (modifying the incoming connections of one node) and column perturbation to specify that a region in the epileptic network is fragile (see Figure 4-2). We compute product-fragility (i.e. the product of the row and column perturbation norms) to determine which nodes are fragile in both a column and row aspect. We hypothesize that epileptic regions are more detectable if they have both high row and column fragility. Because both perturbations are normalized to have norm less than one, taking the product will result in more stable maps. Taking a sliding window over the iEEG data, we estimate a linear dynamical system using least-squares [82] (see Methods section). Then we compute this over a sliding window of the iEEG data to get a spatiotemporal fragility heatmap.

Neural fragility modulates after complete, partial and incomplete resection of the EZ in simulation

To determine how neural fragility of the entire observed iEEG network can potentially be used as an estimator for surgical outcome, we first study how the entire networks' neural fragility modulates in an in-silico environment using TVB. Using the resting-state Epileptor model, we simulate iEEG data using real patient connectomes derived from DTI and T1 MRI data [64, 67, 69]. We set the EZ regions for each patient simulation based on the actual clinically hypothesized EZ. For full details on simulations, see Methods Section on TVB. We model resections by removing that part of the structural connectome. Complete, partial and incomplete resections are modeled as a complete removal of the EZ brain region, partial removal of the EZ, and then a completely incorrect resection of a non-epileptic brain region. For a breakdown of some of the clinical characteristics present in the TVB dataset, see Supplementary

Table -III.

In Figure ??a-c, we show the neural fragility heatmap for an example of a complete, partial and incomplete in-silico resection of the EZ. Neural fragility decreases significantly (K-sample MANOVA PValue = $4.16e-7$) in the successful resections with a Cohen’s D effect size $\tilde{1.4}$ and $\tilde{28}$ times greater than the partial and incomplete resections respectively. The successful resection resulted in an effect size difference between the overall network fragility of 0.761 ± 0.322 , while a failed resection resulted in an effect size of 0.025 ± 0.244 .

Neural fragility decreases in patients with successful resections

Next, we validated our results from TVB simulations on iEEG data from pediatric cases (n=6) with DRE that had epilepsy monitoring and subsequent resective surgery from HSC. This dataset is unique because the chronically same electrodes continue to record throughout the resection, while sampling the identical brain regions [128]. For a full clinical description of the patients from HSC, see Supplementary Table -II.

In Figure 4-4a, we show a product neural fragility heatmap of the pre and post resection iEEG sessions. The post-resection session is considerably lower in values over the entire network, when compared to the pre-resection session. In this specific patient, Figure 4-5, shows that E3 had an effect size decrease in neural fragility of 1.43 ± 0.530 (95% CI). The difference between the post and pre resection was significant at $\alpha = 0.05$ with a PValue of $3.12e-12$ (K-Sample MANOVA with distance correlation).

Neural fragility increases in patient with failed resection

In this dataset, subject E1 had surgical failure with seizure recurrence (Engel III, ILAE 4) after their initial surgical resection. In Figure 4-4b, we compute the product neural fragility heatmap of the pre and post resection iEEG sessions and report that fragility increases in the post-resection iEEG. From pre to post resection session, the

neural fragility of the iEEG network increased by 0.567 ± 0.441 (mean +/- std of Cohen's D effect size).

Compared to the other subjects, E1 is the only subject that had an increase in neural fragility after surgery (Figure 4-5). All other subjects had a decrease in neural fragility ranging from a decrease of 0.845 (subject E7) to 2.324 (subject E5) measured in Cohen's D effect size. Results were similar if a common average reference was applied to the data as well (see Figure 4-6). All the heatmaps show a marked decrease in neural fragility over the entire network when there was a successful surgical outcome, whereas it increased in the patient with a failed outcome.

When only analyzing column neural fragility (applying the column perturbation to the estimated system), we observed that channels inside/outside the clinically annotated EZ were highly fragile in the successful/failed surgical outcome with patient E3 and E1 respectively (see Figure 4-7). This is similar to what was observed in [111]. However, the separation between the failed subject (E1) and the rest (E3-7) in terms of Cohen's D effect size was not as pronounced unless a product neural fragility was used.

Comparing neural fragility and time-frequency spectral features of iEEG

In addition to evaluating neural fragility on the HSC dataset, we also compute common time-frequency based features that would serve as a benchmark. The frequency bands presented and HFOs are common univariate channel features that are looked at by clinicians and the research community in the context of iEEG epilepsy [27, 43, 48, 80, 131]. See Methods Section for full details on how we compute these benchmark features. In Figure 4-5, we compare the pre vs post fragility and compare results to our benchmark features. Fragility is the only one with a clear separation between E1 (i.e. the subject with a failed surgical resection) and patients E3-7 (subjects with

Engel I and ILAE 1 surgical outcomes). Moreover, none of the spectral features result in a difference between the pre and post resection sessions (Figure ??).

Discussion

In this study, we analyze neural fragility, a networked-dynamical systems proposed biomarker of epileptogenicity, from a theoretical perspective and using in-silico and human iEEG data. We demonstrate that neural fragility increases/decreases after a failed/successful surgery respectively. We first confirmed this hypothesis in a virtual epileptic patient, where we demonstrate how different in-silico resective scenarios will affect the overall iEEG network fragility. We then demonstrated the same findings in six pediatric DRE patients from HSC, where all successful surgical patients had a decrease in neural fragility. One patient with a failed surgical outcome showed an increase in overall network fragility.

The effect of anesthesia on epileptic dynamics

Neural fragility is also resilient to the state of anesthesia, as recordings from HSC were performed intraoperatively under constant total intravenous anesthetic (TIVA). Since anesthesia is not fully understood, modeling its effects on the brain are difficult. Combining experimental and observational results about anesthesia may result in more accurate TVB models [132]. The marker is also help with interictal data alone as the input variable. We find that other interictal measures, namely HFOs and EEG spectral content were of less utility than the neural fragility metric.

Neural fragility compared to traditional proposed features of the EZ

Currently, no prospective definition of the EZ exists. Although HFOs were initially promising [48–51, 53, 54], the existence of physiological HFOs [56], problems with

reproducibility of HFO studies [49, 53, 55] and inconclusiveness of existing clinical trials [27] suggest that we need to evaluate other approaches. Neural fragility of a neural network approaches the problem of EZ localization from a networked dynamics perspective. Epileptic nodes within a network are hypothesized to cause an imbalance in the network characterized by its network structure. From a biological view, imbalance due to perturbations between excitatory and inhibitory connections of a neural network can occur through any number of mechanisms, such as elevated glutamate [102, 103, 118–122, 133], genetic disorder impacting synaptic inhibition [104], decreased GABA [105], inclusion of axo-axonic gap junctions [106], loss of inhibitory chandelier cells [107], or axonal sprouting from layer V excitatory pyramidal cells [108]. This imbalance within a neuronal network can cause system instability, where impulses at certain nodes lead to recurring seizures. Although iEEG cannot distinguish between excitatory and inhibitory neuronal populations, the concept of imbalance causing the network to be on the brink of instability can be modeled by neural fragility at the iEEG network level.

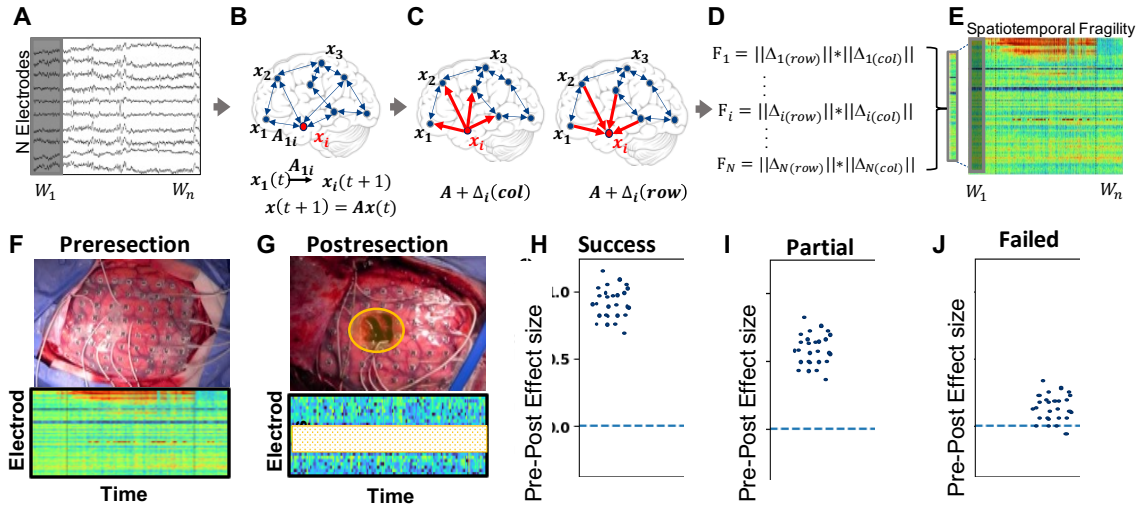


Figure 4-2. Computing fragility as the product of column and row perturbations (A) From a small time window of N iEEG electrodes, (B) a linear time-invariant dynamical system, represented as an A matrix, is estimated. (C) Neural fragility is computed as the minimum amount of energy (measured in norm), represented as a Δ matrix, required to destabilize the linear system. This can be computed for every node within the N -node network (i.e. iEEG electrodes). The norm of the Δ matrix can be computed as a column perturbation over the N nodes, where the perturbation matrix computed has a rank-1 structure with 0's in every column except for the node being perturbed. Similarly, the norm of the Δ matrix can be computed as a row perturbation over the N nodes, where the perturbation matrix computed has a rank-1 structure with 0's in every row except for the node being perturbed. (D) The row and column fragility are combined as a product for all electrodes at every single time point. (E) This is then summarized as a spatiotemporal heatmap. (F) Taking iEEG data from pre-resection sessions, we compute heatmaps and then compare these with (G) post-resection sessions. When we compare the spatiotemporal values between the two sessions using a bootstrap sampling procedure, we expect (H) successful surgeries to have a positive effect size. (I) Partially failed surgeries, where the EZ is not fully captured, should result in smaller, but still positive effect size. (J) Finally, a failed surgery, where the EZ is not resected at all would result in a 0 effect size, or even possibly negative effect size difference between pre and post resection sessions. If a biomarker can detect the presence of the EZ in the network, then one expects it to modulate depending on if the EZ is successfully removed.

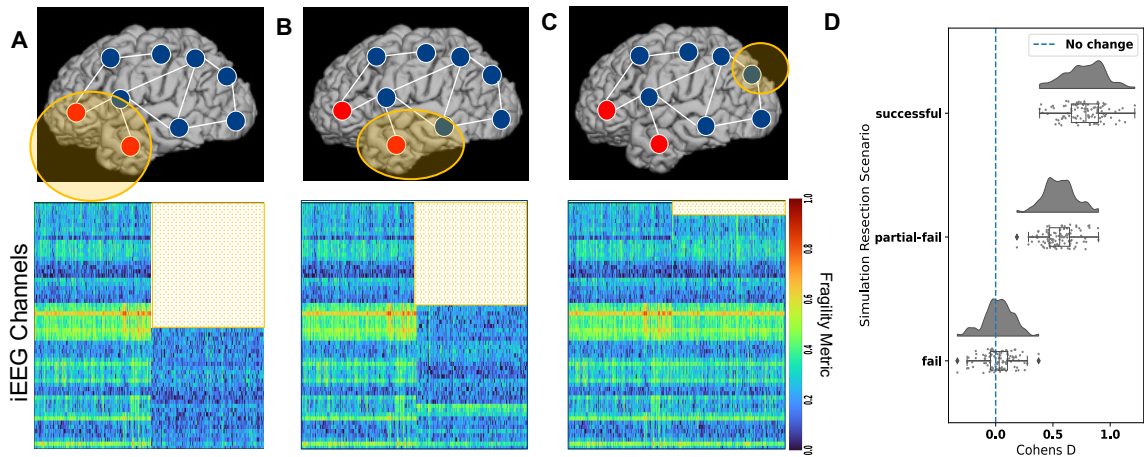


Figure 4-3. Neural product fragility of complete, partial and incomplete in-silico resections of the EZ (A) Neural fragility heatmap of a successful resection of the underlying EZ. The heatmap shows two concatenated sessions: the pre-resection iEEG and post-resection iEEG. The white region represents the channels that were in the resected regions for the post-resection iEEG simulation. (B) Neural fragility of a partially successful resection, where one epileptic region was resected, but another one was left in. Values in the post-resection period still go down, but relative to panel (a), they are slightly higher. (C) Neural fragility of a completely failed resection, where an incorrect brain region was removed. There is qualitatively very little difference with respect to the pre-resection session. The turbo colormap is used in these heatmaps a-c. (D) A summary effect size difference between pre and post resection fragility values for the three resective scenarios from a-c. Each dot represents the Cohens D effect size computed on a bootstrap sample from pre and post resection heatmap. The successful resections have an improvement in overall network fragility (positive Cohen's D), while the failed resection shows essentially no effect difference. The Cohen's D effect size of successful, partial, and incomplete resections were 0.761 ± 0.322 (PValue of $4.16e-7$), 0.542 ± 0.272 (PValue of $2.19e-5$) and 0.025 ± 0.244 (PValue of $4.12e-3$) respectively (all effect sizes are 95% confidence interval). All PValues were computed using a K-Sample MANOVA test using distance correlation with 0.05 alpha level. For more information on how the bootstrap procedure was implemented, see [Statistical Analysis](#).

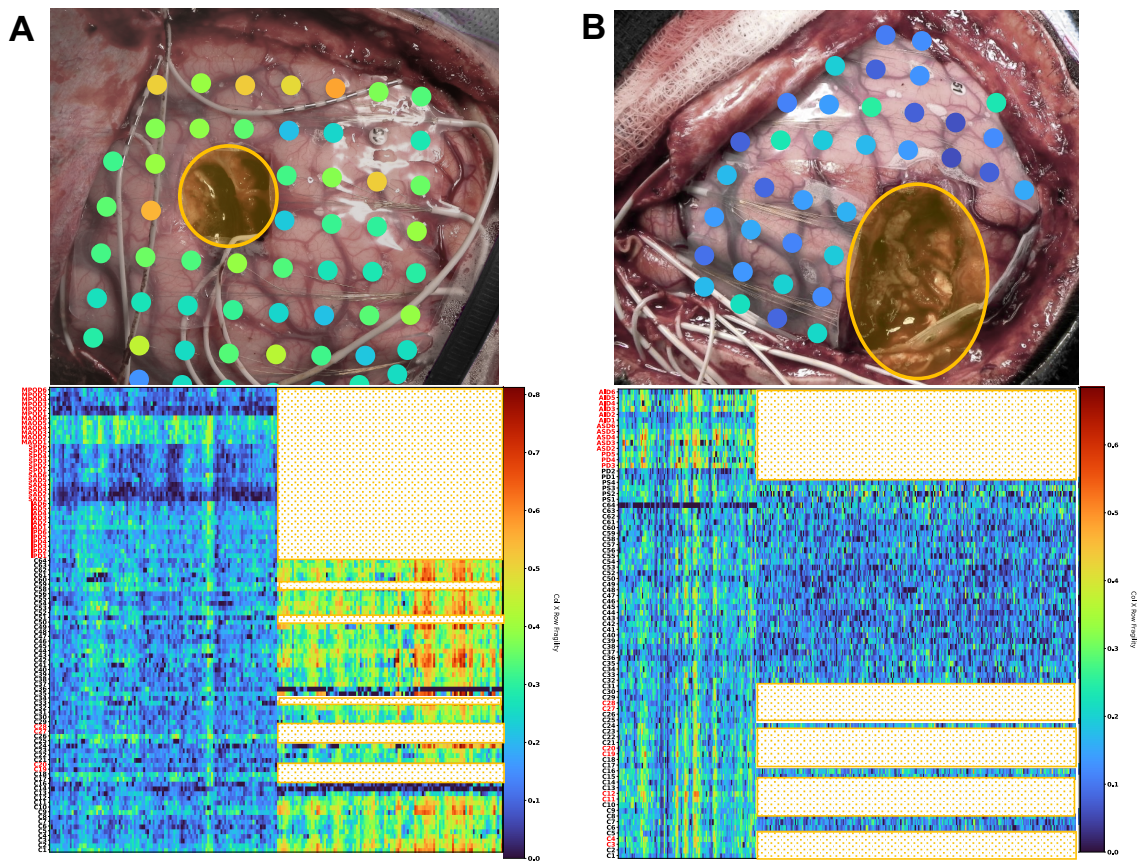


Figure 4-4. Neural product fragility of successful and failed resections in DRE patients at Sick Children Hospital (A) Resected brain photograph (top) of subject E1 from HSC with Engel III outcome. The heatmap (bottom) shows neural fragility of the pre and post-resection iEEG for a patient with failed resection. The heatmaps show two concatenated sessions: the pre-resection iEEG and post-resection iEEG. Values in the post-resection period go up. (B) Resected brain photograph (top) of subject E3 from HSC with Engel I outcome. The heatmap (bottom) shows neural fragility heatmap of the pre and post-resection iEEG for a patient with successful resection. The heatmap shows fragility goes down in the post-resection period. The white region represents the channels that were in the resected regions for the post-resection iEEG simulation, or disconnected due to surgical necessity. The turbo colormap is used in these heatmaps. On the heatmaps' y-axis, are channel labels, with red channel labels annotated as part of the clinical EZ hypothesis. Note that not all channels are annotated, as some are discarded due to poor recording quality (more information in ??). In addition, depth electrodes are not visualized as they are all removed as part of the surgical procedure. We analyzed the raw iEEG under a monopolar reference.

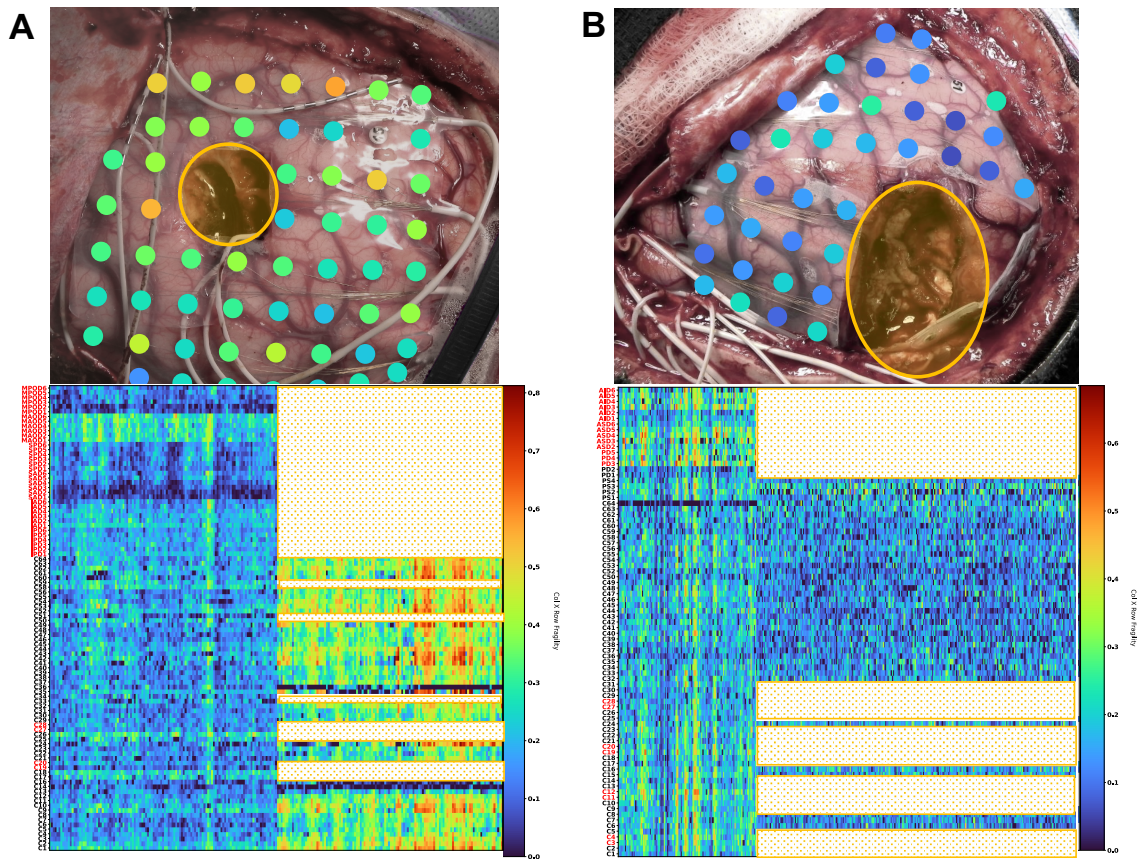


Figure 4-5. Neural fragility of pre vs post resection effect size differences (A) A summary effect size difference between pre and post resection fragility values for the six patients. Each dot represents the Cohens D effect size computed on a bootstrap sample from pre and post resection heatmap. The successful resections have an improvement in overall network fragility (positive Cohen's D), while the failed resection shows an actual increase in overall network fragility. **(B)** Showing the distribution of pvalues computed from the same bootstrap samples in (a), that are computed using a K-Sample MANOVA test with alpha level of 0.05. For more information on how the bootstrap procedure was implemented, see [Statistical Analysis](#). **(C)** A summary effect size difference between pre and post resection HFO rate values for the six patients. Each dot represents the Cohens D effect size computed on a bootstrap sample from pre and post resection session. A positive effect size indicates that there was a decrease in the HFO rates. HFOs were computed using the RMS detector, described in [Time Frequency Representation Analysis](#). **(D)** Corresponding pvalues computed over bootstrap samples of the HFO rates using a Wilcoxon rank-sum test. The graph is displayed on a log-scale on the y-axis.

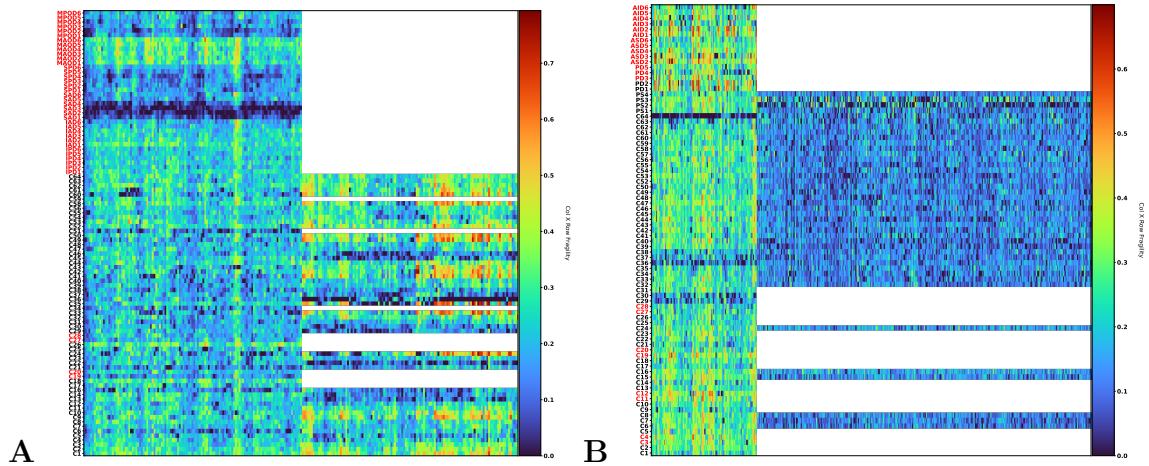


Figure 4-6. Product neural fragility heatmaps using common average referencing (A) Subject E1 with common average reference and (B) subject E3 with common average reference. This is the same heatmaps over the same period of data as Figure 4-4, but using a different reference on the data.

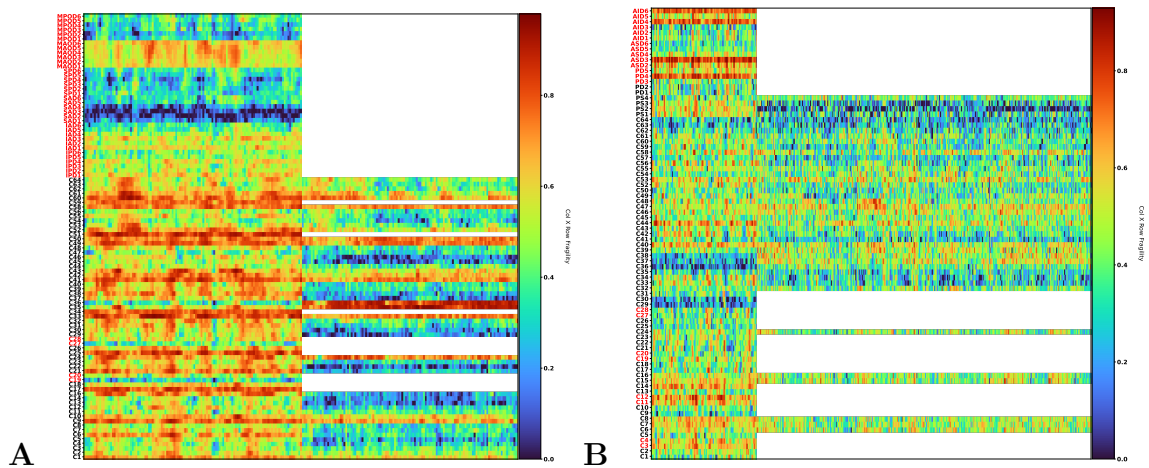


Figure 4-7. Column perturbation neural fragility heatmaps using common average referencing (A) Subject E1 with common average reference and (B) subject E3 with common average reference. This is the same heatmaps over the same period of data as Figure 4-4, but using a different reference on the data.

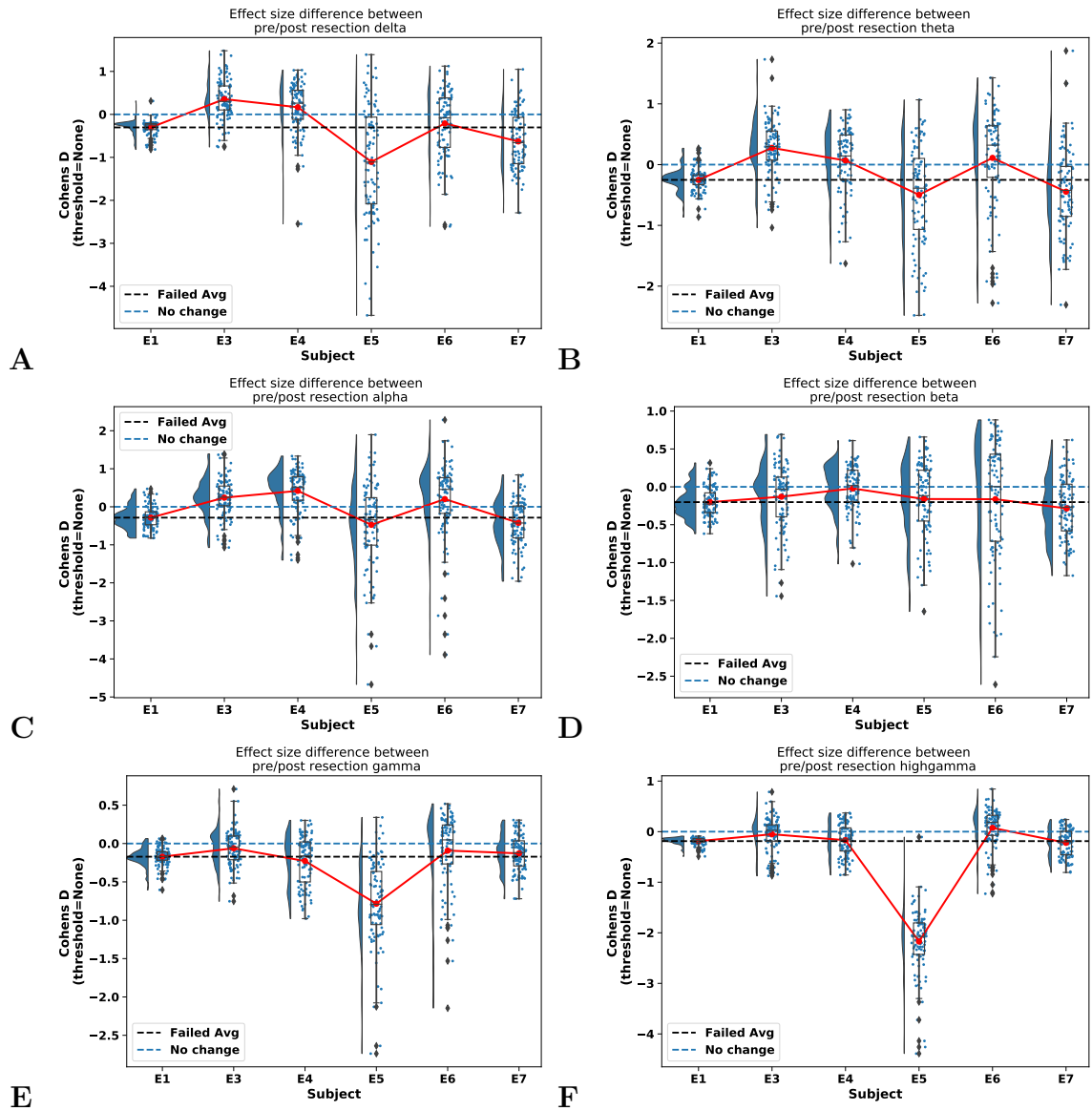


Figure 4-8. Pre vs post resection effect size plots of power in frequency bands (a)-(f) Are delta, theta, alpha, beta, gamma, and highgamma frequency bands respectively. For full details on computing the frequency band power heatmaps, see Methods Section. For examples of the time-frequency heatmaps for all subjects and all frequency bands computed, see Supplementary files.

Conclusions and general discussion

Challenges in validating iEEG features as SOZ markers

Many features have been proposed as potential biomarkers for the SOZ, but none have successfully translated into the clinical workflow [7, 42, 43, 50, 51, 57, 59]. Current limitations for evaluating computational approaches to localization can be largely attributed to i) the lack of ground-truth labels for the true underlying SOZ (it cannot be observed in practice because there is no biomarker), ii) insufficient benchmarking to other iEEG features and iii) a lack in sufficient sampling across epilepsy etiologies.

Since there is no ground truth to drive algorithmic development, one can instead look for features that correlate with clinicians when stratified by outcome measures. Our approach sees if the feature values of the clinically annotated SOZ are "high" in success patients and "low" in failed patients. More rigorously we use feature values of SOZ and SOZ^C to predict surgical outcomes, which is a good approach since we lack ground truth labels of our desired variable. Note that developing algorithms to directly predict the SOZ will at best replicate what the current standard practice is, and achieve a rate of 30-70% surgical success rate [42, 43, 50, 51, 57]. In addition, electrodes within the SOZ may not be a part of the true EZ, but are annotated because of their "appearance" to be the onset of seizures. At best, it can be assumed that in successful surgical outcomes, the EZ is an unknown subset of the SOZ and resected zone. Hence one desires a feature that has relatively high confidence in the

clinically annotated *SOZ* in success outcomes compared to failed outcomes.

Even with a seemingly successful feature derived from data, it is important to benchmark against existing approaches to provide a holistic view of the value of the said feature. Without benchmarking, it is easy to become overly optimistic in terms of the performance of a feature, whereas it may very well be that other iEEG features perform just as well. In this study, we benchmark neural fragility against 20 other proposed features. While other traditional features such as the power in the beta band seem to be informative in *SOZ* localization [26], neural fragility outperforms in effect size, p-value and interpretability.

Although predicting surgical outcomes in our experimental setup is promising, it will be important to understand why certain localizations are successful and why certain are insufficient. If neural fragility is a good marker, then we expect successful outcomes to have high fragility in their clinically annotated SOZ, and lower fragility in the *SOZ^C*, which is shown in this study. Understanding failed localizations and why they failed becomes more difficult. For example, in patients with lesions on MRI scans that correlate with the patient’s EEG and seizure semiology, surgical resection can lead to seizure freedom in approximately 70% of patients [7]. Even in these relatively straightforward cases, localization is not perfect, possibly due to chronic effects of epilepsy such as kindling, which can cause neighboring tissue to become abnormal and epileptogenic [134, 135]. This is why there is a need to sample a heterogeneous and large patient population and derive a feature is invariant on average to epilepsy type and clinical covariates. In this study, we spent over four years to successfully collect and annotate this heterogeneous dataset of 91 patients.

Clinical case complexity and surgical outcomes

In our dataset, we saw varying outcomes across the five clinical centers. Difference in seizure outcomes across the clinical centers can be explained by several contributory factors affecting the complexity of the epileptic syndromes. The multifactorial contributory factors can be related to i) the percentage of non-lesional versus lesional cases, ii) multiple surgical interventions in the past, iii) patient selection and iv) group experience. For example, JHH is a tertiary referral center with high complexity cases (non-lesional MRIs, multiples surgical interventions in the past, complex semiology and EEG interpretation). In addition, data collection is limited depending on clinician resources and retrospective data availability. The relative center-by-center outcomes are not reflective of the actual center's surgical outcome rate, but rather samples from the clinical cases that those clinicians saw at the time of our IRB. The pooled 91 patients though do reflect the approximately 50% surgical success rates seen in DRE patients [Engel2012a, McIntosh2012, Yardi2020]. By including a multitude of centers, we sought to build a diversified sample of varying clinical complexities and practices, thus lending the evaluation of neural fragility more confidence. An important next step would be the prospective evaluation of neural fragility in the context of different clinical case complexities to determine if surgical treatment can be improved with *SOZ* localization assistance.

Virtual epileptic patients can guide EZ hypotheses

Using TVB, a neuroinformatics platform, we were able to simulate whole-brain activity to pose hypotheses about how a proposed biomarker might modulate as a function of resections. The advantage of such a platform is that we can simulate data where we know exactly where the EZ is, and then perform in-silico resections by zeroing out the corresponding rows and columns of the structural connectivity matrix. This

demonstrates that algorithms, such as neural fragility can be used in conjunction with computational modeling with TVB to explore algorithmic performance in a realistic simulation environment.

In 4, we incorporated the resting-state ("interictal") Epileptor model to model resting-state epileptic dynamics [67], but future simulated data could possibly be improved with improved understanding of interictal dynamics.

Why Neural Fragility Performs Well

Rather than analyzing iEEG data at the channel and signal processing level, we seek to model the underlying network dynamics that might give rise to seizures in the form of neural fragility in a dynamical network model. A notion of fragility in networks is commonly seen in analysis of structural [136], economic [137] and even social networks [138]. Although we are not directly analyzing the structural nature of neuronal network, there are studies that have characterized epilepsy in terms of structural fragility and network organization [77, 139]. Specifically, in cellular studies [107, 108], epilepsy is caused by changes, or "perturbations" in the structural network (i.e. chandelier cell loss, or abnormal axonal sprouting from layer V pyramidal cells), which causes loss of inhibition or excessive excitation respectively; these biological changes cause downstream aberrant electrical firing (i.e. seizures). In this study, we analyze a functional network, characterized by a dynamical system derived from the iEEG recordings. Each electrode's effect on the rest of the network is captured by a time-varying linear model that we proposed in [82]. Each node is an electrode, which is recording aggregate neuronal activity within a brain region. By quantifying the fragility of each node, we determine how much of a change in that region's functional connections is necessary to cause seizure-like phenomena (e.g. instability). As a result, high neural fragility is hypothesized to coincide with a region that is sensitive to minute perturbations, causing unstable phenomena in the entire network (i.e. a

seizure).

Presenting neural fragility as spatiotemporal heatmaps allows clinicians to qualitatively assess which electrodes and time points are most fragile within an iEEG network, aggregating any existing data sources (e.g. MRI, neuropsych evaluations, etc.) to formulate a localization hypothesis. By analyzing the fragility heatmaps of patients retrospectively, we conclude that i) fragility is high in electrodes present in the *SOZ* when the patient’s surgery resulted in seizure freedom (i.e. Engel class I) and ii) high fragility is present in electrodes present outside the *SOZ* when the patient’s surgery resulted in seizure recurrence (i.e. Engel class II-IV). In the context of fragility theory of a network, seizure recurrence can be due to perturbations of highly fragile regions in the epileptic network that were left untreated. Importantly, fragility of an electrode within a certain window does not correlate directly with gamma or high-gamma power, which are traditional frequency bands of interest for localizing the *SOZ* [38, 43, 71, 80, 140–143]. This implies that neural fragility presents independent information on top of what clinicians look for in iEEG data. If translated into the clinic, neural fragility can serve as an additional source of information that clinicians can utilize for localization.

Converging to a prospective definition of the EZ

In retrospective studies, validating a proposed biomarker is difficult because one does not know which clinically annotated channels correspond to the true underlying EZ. Typically, approaches have tried to either i) build a prediction model for the clinically annotated epileptic channels [80, 144], ii) build a prediction model for the clinical annotations on only successful patients [57] and iii) building a prediction model conditioned on the clinical annotations that predicts surgical outcome [111]. Building a prediction model for the clinical annotations would not obtain a model of the EZ, since current outcomes vary between 30-70% [33]. Building the prediction model for only patients with successful surgical outcomes limits the amount of data one can

use, but also is limited since not all the clinically annotated electrodes are necessarily epileptogenic. Building a prediction model conditioned on the clinical annotations to predict surgical outcome is a good measure since it takes advantage of both failed and successful outcomes, but also lacks a direct relationship to the underlying EZ because subject variability is still very high. For example, patients can have seizures recur due to kindling, which would not be necessarily due to the EZ [119, 134]. By analyzing iEEG data before and after a surgical intervention on the same subject, we have a better estimate of patient-specific EZs because we can observe the post-resection iEEG for seizures and existence of a proposed biomarker.

Outlook of neural fragility and continuous post operative iEEG

Although our results are encouraging, we have a limited sample size of 6 pediatric patients with only 1 surgical failure. Future studies should keep track of all data available for subjects that had a failed resection to illuminate why certain subjects fail and validate any proposed biomarker. Furthermore, these patients were all children under the age of 18, and thus future research would have to further validate that these results hold for adults.

The paradigm of intraoperative continuous iEEG monitoring to obtain pre and post-resection iEEG data of the same set of electrodes presents with an opportunity to study dynamics as a result of surgical interventions. However, clinical epilepsy is moving towards stereotactic EEG implantations and the surgical procedure for keeping electrodes implanted during a resection has not been developed. Future clinical developments that enable similar pre and post-resection sEEG data will be important to see if neural fragility still modulates with respect to surgical outcomes. If sEEG data can be obtained, caution should be taken to annotate white matter contacts [145].

Scientific and Technological Advances Emerging from Neural Fragility

Neural fragility has the potential to re-define how epilepsy surgery is performed, departing from the classical “localization paradigms” and “en-bloc resections” to a personalized “network-based” user-friendly visualization and surgical strategy. By developing a novel 3D (brain region, time, fragility) network-based method for anatomical representation of the epileptiform activity, including the seizure onset areas and the early propagation zone, this study will have high impact with the potential to offer a safer, more efficient, and cost-effective treatment option for a highly challenging group of patients with disabling DRE. More precise SOZ localization using neural fragility would also guide of chronic implantation of neurostimulation devices aimed to suppress seizures with bursts of current when detected [146–153].

Neural fragility may also be relevant in detecting epileptogenic regions in the brain when applied to interictal (between seizures) iEEG recordings. Ictal or seizure iEEG data are currently the gold standard in clinical practice for localizing the *SOZ* [7, 88]. However, having patients with electrodes implanted for long periods of time, and requiring the monitoring of multiple seizure events over many weeks carries the risk of infection, sudden death, trauma and cognitive deficits from having repeated seizures. This contributes to the large cost of epilepsy monitoring [1, 2, 154–157]. If a candidate iEEG marker could be found that is able to provide strong localizing evidence using only interictal data, then it would significantly reduce invasive monitoring time [139].

Neural fragility is an EEG marker that can also further advance our knowledge of neural mechanisms of seizure generation that will then drive more effective interventions. For example, fragility can be used to identify pathological tissue that are then removed and tested in vitro for abnormal histopathological structure [107, 108]. Knowledge of structural abnormalities may inform new targeted drug treatments. In the future,

specific fragility patterns can be correlated with specific pathological substrates. Likely, the specific pathological substrates will have different therapeutic approaches. As an example, epilepsy caused by focal cortical dysplasia is treated with focal surgical resection, but post-encephalic epilepsy may have a better therapeutic response with immunosuppressants and steroids.

Finally, neural fragility may have broader implications in understanding how underlying brain network dynamics change during intervention (e.g. drugs or electrical stimulation). Fragility analysis can be applied as a method of assessing the efficacy of specific drug trials to specific pathological groups, which include not only epilepsy but other neurological conditions such as Alzheimer's disease or the spectrum of dementias. Commonly, the current optimal criteria to recognize therapeutic success in many neurological conditions is purely clinical, but clinical responses are not immediate. This delay in recognizing the appropriate drug and adequate therapeutic doses is highly detrimental. Computational methods as fragility could provide an additional criteria for drug responses, which can be immediate, guiding the treating physician to the correct treatment without delays and unnecessary drug trials. Furthermore, if neural fragility could be accurately obtained from non-invasive tests or from permanently implanted devices, the current fragility of the network could be used as a surrogate marker of patient's current clinical state. As such, the changes in the fragility could be used as a proxy for improvement or recurrences that occur as medication doses (or other treatments, such as Keto Diet [158]) are changed over time.

References

1. Berg, A. T. Identification of Pharmacoresistant Epilepsy. *Neurologic Clinics* **27**. Publisher: NIH Public Access, 1003–1013 (Nov. 2009).
2. WHO & Organization, W. H. Epilepsy (2019).
3. Jobst, B. C. Consensus over individualism: Validation of the ILAE definition for drug resistant epilepsy. *Epilepsy Currents* **15**. Publisher: American Epilepsy Society, 172–173 (2015).
4. Begley, C. E. & Durgin, T. L. The direct cost of epilepsy in the United States: A systematic review of estimates. *Epilepsia* **56**, 1376–1387 (Sept. 2015).
5. Jehi, L. The epileptogenic zone: Concept and definition. *Epilepsy Currents* **18**. Publisher: American Epilepsy Society, 12–16 (2018).
6. Penfield, W. Epileptogenic lesions. *Acta neurologica et psychiatrica Belgica* **56**, 75–88 (Feb. 1956).
7. Sheikh, S. *et al.* Redefining success in epilepsy surgery: The importance of relative seizure reduction in patient reported quality of life. *Epilepsia*, 2078–2085 (August 2019).
8. Talairach, J. *et al.* Surgical therapy for frontal epilepsies. *Advances in neurology* **57**, 707–32 (1992).
9. Spencer, S. S. Neural networks in human epilepsy: Evidence of and implications for treatment. *Epilepsia* **43**. Publisher: Blackwell Publishing, Inc., 219–227 (Mar. 2002).
10. Nair, D. R., Mohamed, A., Burgess, R. & Lüders, H. A critical review of the different conceptual hypotheses framing human focal epilepsy. *Epileptic Disorders* **6**, 77–83 (2004).
11. Engel, J., Levesque, M. F. & Shields, W. D. Surgical treatment of the epilepsies: presurgical evaluation. *Clinical neurosurgery* **38**. Publisher: Raven Press, 514–534 (1992).
12. Scheffer, I. E. *et al.* ILAE classification of the epilepsies: Position paper of the ILAE Commission for Classification and Terminology. *Epilepsia* **58**. Publisher: John Wiley & Sons, Ltd (10.1111), 512–521 (Apr. 2017).
13. Rho, J. M. & White, H. S. Brief history of anti-seizure drug development. *Epilepsia Open* **3**. Publisher: Wiley-Blackwell Publishing Ltd, 114–119 (Dec. 2018).
14. Goldenberg, M. M. Overview of Drugs Used For Epilepsy and Seizures. *Pharmacy and Therapeutics* **35**, 392–415 (July 2010).

15. St Louis, E. K. & Cascino, G. D. Diagnosis of Epilepsy and Related Episodic Disorders. *Continuum (Minneapolis, Minn.)* **22**, 15–37 (Feb. 2016).
16. Angus-Leppan, H. Diagnosing epilepsy in neurology clinics: a prospective study. *Seizure* **17**, 431–436 (July 2008).
17. Elger, C. E. & Hoppe, C. Diagnostic challenges in epilepsy: seizure under-reporting and seizure detection. *The Lancet. Neurology* **17**, 279–288 (Mar. 2018).
18. Podell, M. Antiepileptic drug therapy. *Clinical Techniques in Small Animal Practice* **13**, 185–192 (Aug. 1998).
19. Moosa, A. N. V. Antiepileptic Drug Treatment of Epilepsy in Children. *Continuum (Minneapolis, Minn.)* **25**, 381–407 (Apr. 2019).
20. Jobst, B. C., Darcey, T. M., Thadani, V. M. & Roberts, D. W. Brain stimulation for the treatment of epilepsy: Brain Stimulation in Epilepsy. *Epilepsia* **51**, 88–92 (July 2010).
21. Grote, A. *et al.* A second chance—reoperation in patients with failed surgery for intractable epilepsy: long-term outcome, neuropsychology and complications. *Journal of Neurology, Neurosurgery, and Psychiatry* **87**, 379–385 (Apr. 2016).
22. Langfitt, J. T. *et al.* Health care costs decline after successful epilepsy surgery. *Neurology* **68**, 1290–1298 (Apr. 17, 2007).
23. Andrews, J. P. *et al.* Association of Seizure Spread With Surgical Failure in Epilepsy. *JAMA neurology* **76**, 462–469 (Apr. 1, 2019).
24. Youngerman, B. E., Khan, F. A. & McKhann, G. M. Stereoelectroencephalography in epilepsy, cognitive neurophysiology, and psychiatric disease: Safety, efficacy, and place in therapy. *Neuropsychiatric Disease and Treatment* **15**. Publisher: Dove Medical Press Ltd., 1701–1716 (2019).
25. Yan, H. *et al.* Method of invasive monitoring in epilepsy surgery and seizure freedom and morbidity: A systematic review. *Epilepsia* **60**. Publisher: Blackwell Publishing Inc., 1960–1972 (Sept. 2019).
26. Sharma, A. *Epileptic seizure prediction using power analysis in beta band of EEG signals* in. International Conference on Soft Computing Techniques and Implementations, ICSCIT 2015 (Institute of Electrical and Electronics Engineers Inc., June 2016), 117–121.
27. Gloss, D., Nevitt, S. J. & Staba, R. The role of high-frequency oscillations in epilepsy surgery planning. *Cochrane Database of Systematic Reviews* **2017**. Publisher: John Wiley and Sons Ltd (Oct. 2017).
28. Staley, K. J. & Dudek, F. E. Interictal spikes and epileptogenesis. *Epilepsy Currents* **6**, 199–202 (Dec. 2006).
29. González-Martínez, J. A., Srikiyvilaiikul, T., Nair, D. & Bingaman, W. E. Long-term seizure outcome in reoperation after failure of epilepsy surgery. *Neurosurgery* **60**, 873–880, discussion 873–880 (May 2007).
30. Yardi, R. *et al.* Long-term outcomes of reoperations in epilepsy surgery. *Epilepsia* **61**. Publisher: Blackwell Publishing Inc., 465–478 (Mar. 2020).

31. Téllez-Zenteno, J. F., Dhar, R. & Wiebe, S. Long-term seizure outcomes following epilepsy surgery: a systematic review and meta-analysis. *Brain: A Journal of Neurology* **128**, 1188–1198 (Pt 5 May 2005).
32. Spencer, S. & Huh, L. Outcomes of epilepsy surgery in adults and children. *The Lancet. Neurology* **7**, 525–537 (June 2008).
33. Engel, J. *et al.* Early surgical therapy for drug-resistant temporal lobe epilepsy: A randomized trial. *JAMA - Journal of the American Medical Association* **307**. Publisher: JAMA, 922–930 (Feb. 2012).
34. Korzeniewska, A. *et al.* Ictal propagation of high frequency activity is recapitulated in interictal recordings: Effective connectivity of epileptogenic networks recorded with intracranial EEG. *NeuroImage* **101**, 96–113 (2014).
35. Jeppesen, J., Beniczky, S., Fuglsang-Frederiksen, A., Sidenius, P. & Jasemian, Y. Detection of epileptic-seizures by means of power spectrum analysis of heart rate variability: A pilot study. *Technology and Health Care* **18**, 417–426 (2010).
36. Alarcon, G., Binnie, C. D., Elwes, R. D. C. & Polkey, C. E. Power spectrum and intracranial EEG patterns at seizure onset in partial epilepsy. *Electroencephalography and Clinical Neurophysiology* **94**. Publisher: Elsevier, 326–337 (May 1995).
37. Tharp, B. R. & Gersch, W. Spectral analysis of seizures in humans. *Computers and Biomedical Research* **8**. Publisher: Academic Press, 503–521 (Dec. 1975).
38. Medvedev, A. V., Murro, A. M. & Meador, K. J. Abnormal interictal gamma activity may manifest a seizure onset zone in temporal lobe epilepsy. *International Journal of Neural Systems* **21**. Publisher: World Scientific Publishing Company, 103–114 (Apr. 2011).
39. Weiss, S. A. *et al.* Ictal high frequency oscillations distinguish two types of seizure territories in humans. *Brain : a journal of neurology* **136**. Publisher: Narnia, 3796–3808 (Pt 12 Dec. 2013).
40. Gliske, S. V. *et al.* Universal automated high frequency oscillation detector for real-time, long term EEG. *Clinical Neurophysiology* **127**, 1057–1066 (2016).
41. Jeppesen, J., Beniczky, S., Johansen, P., Sidenius, P. & Fuglsang-Frederiksen, A. Detection of epileptic seizures with a modified heart rate variability algorithm based on Lorenz plot. *Seizure* **24**. Publisher: W.B. Saunders Ltd, 1–7 (C 2015).
42. Li, A., Marmaduke, W., Viktor, J. & Sridevi, S. *27th Annual Computational Neuroscience Meeting (CNS*2018): Part Two* in. BMC neuroscience. **19**. Issue: S2 (BioMed Central, Oct. 2018), 65–65.
43. Burns, S. P. *et al.* Network dynamics of the brain and influence of the epileptic seizure onset zone. *Proceedings of the National Academy of Sciences* **111**. Publisher: National Academy of Sciences, E5321–E5330 (Dec. 2014).
44. Yaffe, R. B. *et al.* Physiology of functional and effective networks in epilepsy. *Clinical Neurophysiology* **126**, 227–236 (2015).
45. Shah, P. *et al.* Local structural connectivity directs seizure spread in focal epilepsy. *bioRxiv*. Publisher: Cold Spring Harbor Laboratory, 406793–406793 (Sept. 2018).
46. Bassett, D. S. & Sporns, O. Network neuroscience. *Nature neuroscience* **20**. Publisher: NIH Public Access, 353–364 (Feb. 2017).

47. Chung, J. *et al.* Statistical Connectomics. Publisher: OSF Preprints.
48. Gliske, S. V., Irwin, Z. T., Chestek, C. & Stacey, W. C. Effect of sampling rate and filter settings on High Frequency Oscillation detections. *Clinical Neurophysiology* **127**, 3042–3050 (Sept. 2016).
49. Fedele, T. *et al.* Resection of high frequency oscillations predicts seizure outcome in the individual patient. *Scientific Reports* **7**. Publisher: Nature Publishing Group, 13836–13836 (Dec. 2017).
50. Varatharajah, Y. *et al.* EEG-GRAPH: A factor-graph-based model for capturing spatial, temporal, and observational relationships in electroencephalograms in. Advances in Neural Information Processing Systems. **2017-Decem** (2017), 5372–5381.
51. Varatharajah, Y. *et al.* Integrating artificial intelligence with real-time intracranial EEG monitoring to automate interictal identification of seizure onset zones in focal epilepsy. *Journal of Neural Engineering* **15** (Dec. 2018).
52. Haegelen, C. *et al.* High-frequency oscillations, extent of surgical resection, and surgical outcome in drug-resistant focal epilepsy. *Epilepsia* **54**. Publisher: PMC Canada manuscript submission, 848–857 (May 2013).
53. Cuello-Oderiz, C. *et al.* Value of ictal and interictal epileptiform discharges and high frequency oscillations for delineating the epileptogenic zone in patients with focal cortical dysplasia. *Clinical Neurophysiology* **129**. Publisher: Elsevier Ireland Ltd, 1311–1319 (June 2018).
54. Höller, Y. *et al.* High-frequency oscillations in epilepsy and surgical outcome. A meta-analysis. *Frontiers in Human Neuroscience* **9**. Publisher: Frontiers, 574–574 (Oct. 2015).
55. Spring, A. M. *et al.* Interrater reliability of visually evaluated high frequency oscillations. *Clinical Neurophysiology* **128**, 433–441 (Mar. 2017).
56. Höller, P., Trinka, E. & Höller, Y. High-Frequency Oscillations in the Scalp Electroencephalogram: Mission Impossible without Computational Intelligence. *Computational Intelligence and Neuroscience* **2018**. Publisher: Hindawi Limited (2018).
57. Li, Y. H. *et al.* Localization of epileptogenic zone based on graph analysis of stereo-EEG. *Epilepsy Research* **128**. Publisher: Elsevier B.V., 149–157 (2016).
58. Khambhati, A. N. *et al.* Dynamic Network Drivers of Seizure Generation, Propagation and Termination in Human Neocortical Epilepsy. *PLOS Computational Biology* **11** (ed Kramer, M.) Publisher: Public Library of Science, e1004608–e1004608 (Dec. 2015).
59. Khambhati, A. N., Davis, K. A., Lucas, T. H., Litt, B. & Bassett, D. S. Virtual Cortical Resection Reveals Push-Pull Network Control Preceding Seizure Evolution. *Neuron* **91**. Publisher: NIH Public Access, 1170–1182 (Sept. 2016).
60. Lynall, M. E. *et al.* Functional connectivity and brain networks in schizophrenia. *Journal of Neuroscience* **30**. Publisher: Society for Neuroscience, 9477–9487 (July 2010).
61. Abreu, R., Leal, A. & Figueiredo, P. Identification of epileptic brain states by dynamic functional connectivity analysis of simultaneous EEG-fMRI: a dictionary learning approach. *Scientific Reports* **9**. Publisher: Nature Publishing Group, 638–638 (Dec. 2019).

62. Deuker, L. *et al.* Reproducibility of graph metrics of human brain functional networks. *NeuroImage* **47**, 1460–1468 (Oct. 1, 2009).
63. Skocik, M., Collins, J., Callahan-Flintoft, C., Bowman, H. & Wyble, B. I Tried a Bunch of Things: The Dangers of Unexpected Overfitting in Classification. *bioRxiv*. Publisher: Cold Spring Harbor Laboratory, 078816–078816 (Feb. 2016).
64. Jirsa, V. K., Stacey, W. C., Quilichini, P. P., Ivanov, A. I. & Bernard, C. On the nature of seizure dynamics. *Brain* **137**, 2210–2230 (2014).
65. Proix, T., Bartolomei, F., Guye, M. & Jirsa, V. K. Individual brain structure and modelling predict seizure propagation. *Brain : a journal of neurology* **140**, 641–654 (2017).
66. Proix, T., Jirsa, V. K., Bartolomei, F., Guye, M. & Truccolo, W. Predicting the spatiotemporal diversity of seizure propagation and termination in human focal epilepsy. *Nature Communications* **9**. Publisher: Nature Publishing Group (Dec. 2018).
67. Courtiol, J., Guye, M., Bartolomei, F., Petkoski, S. & Jirsa, V. K. Dynamical Mechanisms of Interictal Resting-State Functional Connectivity in Epilepsy. *The Journal of Neuroscience* **40**, 5572–5588 (July 15, 2020).
68. El Houssaini, K., Bernard, C. & Jirsa, V. K. The Epileptor Model: A Systematic Mathematical Analysis Linked to the Dynamics of Seizures, Refractory Status Epilepticus, and Depolarization Block. *eNeuro* **7**, ENEURO.0485–18.2019 (Apr. 2020).
69. Jirsa, V. K. *et al.* The Virtual Epileptic Patient: Individualized whole-brain models of epilepsy spread. *NeuroImage* **145**. Publisher: Academic Press Inc., 377–388 (Jan. 2017).
70. Hashemi, M. *et al.* The Bayesian Virtual Epileptic Patient: A probabilistic framework designed to infer the spatial map of epileptogenicity in a personalized large-scale brain model of epilepsy spread. *NeuroImage* **217**, 116839 (Aug. 15, 2020).
71. Bulacio, J. C. *et al.* Long-term seizure outcome after resective surgery in patients evaluated with intracranial electrodes. *Epilepsia* **53**. Publisher: Blackwell Publishing Ltd, 1722–1730 (Oct. 2012).
72. Vakharia, V. N. *et al.* Getting the best outcomes from epilepsy surgery. *Annals of Neurology* (2018).
73. Wu, C. & Sharan, A. D. Neurostimulation for the Treatment of Epilepsy: A Review of Current Surgical Interventions. *Neuromodulation: Technology at the Neural Interface* **16**, 10–24 (Jan. 2013).
74. McIntosh, A. M. *et al.* Long-term seizure outcome and risk factors for recurrence after extratemporal epilepsy surgery. *Epilepsia* **53**. Publisher: Epilepsia, 970–978 (June 2012).
75. McIntosh, A. M. *et al.* Temporal lobectomy: Long-term seizure outcome, late recurrence and risks for seizure recurrence. *Brain* **127**. Publisher: Oxford University Press, 2018–2030 (Aug. 2004).
76. Hermann, B. P. *et al.* Cognitive prognosis in chronic temporal lobe epilepsy. *Annals of Neurology* **60**. Publisher: Wiley Subscription Services, Inc., A Wiley Company, 80–87 (July 2006).

77. Sritharan, D. & Sarma, S. V. Fragility in Dynamic Networks: Application to Neural Networks in the Epileptic Cortex. *Neural Computation* **26**. Publisher: MIT Press One Rogers St., Cambridge, MA 02142-1209 USA journals-info@mit.edu, 2294–2327 (Oct. 2014).
78. Holdgraf, C. *et al.* iEEG-BIDS, extending the Brain Imaging Data Structure specification to human intracranial electrophysiology. *Scientific data* **6**. Publisher: NLM (Medline), 102–102 (June 2019).
79. Scharfman, H. E. The neurobiology of epilepsy. *Current Neurology and Neuroscience Reports* **7**. Publisher: NIH Public Access, 348–354 (July 2007).
80. Li, A. *et al.* Using network analysis to localize the epileptogenic zone from invasive EEG recordings in intractable focal epilepsy. *Network Neuroscience* **02**. Publisher: MIT Press One Rogers Street, Cambridge, MA 02142-1209 USA journals-info@mit.edu, 218–240 (June 2018).
81. Li, A., Inati, S., Zaghloul, K. & Sarma, S. *Fragility in epileptic networks: The epileptogenic zone* in. Proceedings of the American Control Conference (2017).
82. Li, A. *et al.* *Linear time-varying model characterizes invasive EEG signals generated from complex epileptic networks* in. Proceedings of the Annual International Conference of the IEEE Engineering in Medicine and Biology Society, EMBS (2017).
83. Li, A., Inati, S., Zaghloul, K. & Sarma, S. *Fragility in Epileptic Networks : the Epileptogenic Zone* in. American Control Conference (2017), 1–8.
84. Kato, T. *Perturbation Theory for Linear Operators* (Springer Berlin Heidelberg, Berlin, Heidelberg, 1995).
85. Hawasli, A. H. *et al.* Influence of white and gray matter connections on endogenous human cortical oscillations. *Frontiers in Human Neuroscience* **10** (June 2016).
86. Gonzalez-Martinez, J. *et al.* Robot-assisted stereotactic laser ablation in medically intractable epilepsy: Operative technique. *Neurosurgery* **10**. Publisher: Neurosurgery, 167–172 (2014).
87. Gonzalez-Martinez, J. & Najm, I. M. Indications and selection criteria for invasive monitoring in children with cortical dysplasia. *Child’s Nervous System* **30**. Publisher: Springer Verlag, 1823–1829 (Nov. 2014).
88. Bulacio, J. C., Chauvel, P. & McGonigal, A. Stereoelectroencephalography: Interpretation. *Journal of Clinical Neurophysiology* **33**, 503–510 (Dec. 2016).
89. See, S. J. *et al.* Surgical outcomes in patients with extratemporal epilepsy and subtle or normal magnetic resonance imaging findings. *Neurosurgery* **73**, 68–76 (July 2013).
90. Mezić, I. Spectral Properties of Dynamical Systems, Model Reduction and Decompositions. *Nonlinear Dynamics* **41**, 309–325 (Aug. 1, 2005).
91. Schmid, P. J. Dynamic mode decomposition of numerical and experimental data. *Journal of Fluid Mechanics* **656**. Publisher: Cambridge University Press, 5–28 (Aug. 2010).
92. Welch, P. D. The Use of Fast Fourier Transform for the Estimation of Power Spectra: A Method Based on Time Averaging Over Short, Modified Periodograms. *IEEE Transactions on Audio and Electroacoustics* **15**, 70–73 (June 1967).

93. Gramfort, A. *et al.* MNE software for processing MEG and EEG data. *NeuroImage* **86**. Publisher: Academic Press, 446–460 (Feb. 2014).
94. Gramfort, A. *et al.* MEG and EEG data analysis with MNE-Python. *Frontiers in Neuroscience* **7**. Publisher: Frontiers, 267–267 (Dec. 2013).
95. Breiman, L. Random Forests. *Machine Learning* **45**, 5–32 (2001).
96. Perry, R. *et al.* Manifold Forests: Closing the Gap on Neural Networks. *Arxiv* (Sept. 2019).
97. Tomita, T. M. *et al.* Sparse projection oblique randomer forests. *Journal of Machine Learning Research* **21** (2020).
98. Pedregosa, F. *et al.* Scikit-learn: Machine Learning in Python. *Journal of Machine Learning Research* **12**, 2825–2830 (2011).
99. Ho, J., Tumkaya, T., Aryal, S., Choi, H. & Claridge-Chang, A. Moving beyond P values: data analysis with estimation graphics. *Nature Methods* **16**. Publisher: Nature Publishing Group, 565–566 (July 2019).
100. Alyakin, A., Qin, Y. & Priebe, C. E. LqRT: Robust Hypothesis Testing of Location Parameters using Lq-Likelihood-Ratio-Type Test in Python. *Arxiv* (Nov. 2019).
101. Qin, Y. & Priebe, C. E. Robust hypothesis testing via Lq-likelihood. *Statistica Sinica* **27**, 1793–1813 (2017).
102. Crino, P. B. *et al.* Increased expression of the neuronal glutamate transporter (EAAT3/EAAC1) in hippocampal and neocortical epilepsy. *Epilepsia* **43**. Publisher: NIH Public Access, 211–218 (2002).
103. González-Martínez, J. A., Ying, Z., Prayson, R., Bingaman, W. & Najm, I. Glutamate clearance mechanisms in resected cortical dysplasia: Laboratory investigation. *Journal of Neurosurgery* **114**. Publisher: American Association of Neurological Surgeons, 1195–1202 (Apr. 2011).
104. Noebels, J. L. The biology of epilepsy genes. *Annual Review of Neuroscience* **26**. Publisher: Annu Rev Neurosci, 599–625 (2003).
105. Bradford, H. F. Glutamate, GABA and epilepsy. *Progress in Neurobiology* **47**. Publisher: Prog Neurobiol, 477–511 (1995).
106. Traub, R. D. *et al.* A possible role for gap junctions in generation of very fast EEG oscillations preceding the onset of, and perhaps initiating, seizures. *Epilepsia* **42**. Publisher: Epilepsia, 153–170 (2001).
107. DeFelipe, J. Chandelier cells and epilepsy. *Brain* **122**, 1807–1822 (Oct. 1999).
108. Jin, X., Prince, D. A. & Huguenard, J. R. Enhanced Excitatory Synaptic Connectivity in Layer V Pyramidal Neurons of Chronically Injured Epileptogenic Neocortex in Rats. *Journal of Neuroscience* **26**, 4891–4900 (May 2006).
109. Couronné, R., Probst, P. & Boulesteix, A. L. Random forest versus logistic regression: A large-scale benchmark experiment. *BMC Bioinformatics* **19**. Publisher: BioMed Central Ltd., 270–270 (July 2018).
110. Kini, L. G. *et al.* Virtual resection predicts surgical outcome for drug-resistant epilepsy. *Brain* **142**. Publisher: Oxford University Press, 3892–3905 (Dec. 2019).

111. Li, A. *et al.* Neural Fragility as an EEG Marker of the Seizure Onset Zone. *bioRxiv*, 862797–862797 (2019).
112. Simchowitz, M., Mania, H., Tu, S., Jordan, M. I. & Recht, B. *Learning Without Mixing: Towards A Sharp Analysis of Linear System Identification* in *Conference On Learning Theory* Conference On Learning Theory. ISSN: 2640-3498 (PMLR, July 3, 2018), 439–473.
113. Cohen, M. J. in *Encyclopedia of Clinical Neuropsychology* 556–559 (Springer New York, 2011).
114. Kemp, B., Värri, A., Rosa, A. C., Nielsen, K. D. & Gade, J. A simple format for exchange of digitized polygraphic recordings. *Electroencephalography and Clinical Neurophysiology* **82**, 391–393 (May 1992).
115. Gorgolewski, K. J. *et al.* The brain imaging data structure, a format for organizing and describing outputs of neuroimaging experiments. *Scientific Data* **3**, 160044–160044 (Dec. 2016).
116. Van Der Walt, S., Colbert, S. C. & Varoquaux, G. The NumPy array: A structure for efficient numerical computation. *Computing in Science and Engineering* **13**, 22–30 (Mar. 2011).
117. Virtanen, P. *et al.* SciPy 1.0: fundamental algorithms for scientific computing in Python. *Nature Methods* **17**. Publisher: Nature Research, 261–272 (Mar. 2020).
118. Greenamyre, J. T. The Role of Glutamate in Neurotransmission and in Neurologic Disease. *Archives of Neurology* **43**. Publisher: Arch Neurol, 1058–1063 (1986).
119. Zhang, W. Q., Hudson, P. M., Sobotka, T. J., Hong, J. S. & Tilson, H. A. Extracellular concentrations of amino acid transmitters in ventral hippocampus during and after the development of kindling. *Brain Research* **540**. Publisher: Brain Res, 315–318 (Feb. 1991).
120. Sherwin, A. *et al.* Excitatory amino acids are elevated in human epileptic cerebral cortex. *Neurology* **38**, 920–923 (June 1988).
121. Janjua, N. A., Kabuto, H. & Mori, A. Increased plasma glutamic acid in a genetic model of epilepsy. *Neurochemical Research* **17**. Publisher: Kluwer Academic Publishers-Plenum Publishers, 293–296 (Mar. 1992).
122. Simantov, R. *et al.* Changes in expression of neuronal and glial glutamate transporters in rat hippocampus following kainate-induced seizure activity. *Molecular Brain Research* **65**, 112–123 (Feb. 1999).
123. Li, A. MNE-HFO: An open-source Python implementation of HFO detection algorithms. Publisher: Zenodo (Feb. 1, 2021).
124. Burnos, S. *et al.* The morphology of high frequency oscillations (HFO) does not improve delineating the epileptogenic zone. *Clinical Neurophysiology* **127**. Publisher: Elsevier Ireland Ltd, 2140–2148 (Apr. 2016).
125. Kucewicz, M. T. *et al.* High frequency oscillations are associated with cognitive processing in human recognition memory. *Brain: A Journal of Neurology* **137**, 2231–2244 (Pt 8 Aug. 2014).

126. Jirsa, V. K., Sporns, O., Breakspear, M., Deco, G. & McIntosh, A. R. Towards the virtual brain: network modeling of the intact and the damaged brain. *Archives italiennes de biologie* **148**, 189–205 (Sept. 2010).
127. Shen, C. & Vogelstein, J. T. The exact equivalence of distance and kernel methods in hypothesis testing. *AStA Advances in Statistical Analysis* (Sept. 30, 2020).
128. Warsi, N. M. *et al.* Supplementing Extraoperative ElectroCorticography With Real-Time Intraoperative Recordings Using the Same Chronically Implanted Electrodes. *Operative Neurosurgery (Hagerstown, Md.)* **20**, 559–564 (May 13, 2021).
129. Yang, T., Hakimian, S. & Schwartz, T. H. Intraoperative ElectroCorticography (ECog): indications, techniques, and utility in epilepsy surgery. *Epileptic Disorders* **16**. [_eprint: https://onlinelibrary.wiley.com/doi/pdf/10.1684/epd.2014.0675](https://onlinelibrary.wiley.com/doi/pdf/10.1684/epd.2014.0675), 271–279 (2014).
130. Kuruvilla, A. & Flink, R. Intraoperative electrocorticography in epilepsy surgery: useful or not? *Seizure* **12**, 577–584 (Dec. 1, 2003).
131. Yaffe, R. *et al.* *Brain state evolution during seizure and under anesthesia: A network-based analysis of stereotaxic eeg activity in drug-resistant epilepsy patients* in. Proceedings of the Annual International Conference of the IEEE Engineering in Medicine and Biology Society, EMBS (IEEE, Aug. 2012), 5158–5161.
132. Abel, J. H. *et al.* Machine learning of EEG spectra classifies unconsciousness during GABAergic anesthesia. *PLOS ONE* **16**. Publisher: Public Library of Science, e0246165 (May 6, 2021).
133. During, M. J. & Spencer, D. D. Extracellular hippocampal glutamate and spontaneous seizure in the conscious human brain. *The Lancet* **341**. Publisher: Lancet, 1607–1610 (June 1993).
134. Bertram, E. The relevance of kindling for human epilepsy. *Epilepsia* **48**, 65–74 (SUPPL. 2 Apr. 2007).
135. Laxer, K. D. *et al.* The consequences of refractory epilepsy and its treatment. *Epilepsy and Behavior* **37**. Publisher: Academic Press Inc., 59–70 (2014).
136. Wilson, M. Network Topology and the Fragility of Tetrahedral Glass-Forming Liquids Temperature dependent structure of liquids, melts and glasses View project Glassy and liquid materials under pressure View project. *Article in Physical Review Letters* (2009).
137. Piccardi, C. & Tajoli, L. Complexity, centralization, and fragility in economic networks. *PLOS ONE* **13** (ed Suweis, S.) e0208265–e0208265 (Nov. 2018).
138. Wei, W., Joseph, K., Liu, H. & Carley, K. M. *The fragility of twitter social networks against suspended users* in. Proceedings of the 2015 IEEE/ACM International Conference on Advances in Social Networks Analysis and Mining, ASONAM 2015 (Association for Computing Machinery, Inc, Aug. 2015), 9–16.
139. Kramer, M. A. & Cash, S. S. Epilepsy as a disorder of cortical network organization. *Neuroscientist* **18**. Publisher: SAGE PublicationsSage CA: Los Angeles, CA, 360–372 (Aug. 2012).
140. Hughes, J. R. Gamma, fast, and ultrafast waves of the brain: Their relationships with epilepsy and behavior. *Epilepsy and Behavior* **13**, 25–31 (July 2008).

141. Grinenko, O. *et al.* A fingerprint of the epileptogenic zone in human epilepsies. *Brain* **141**. Publisher: Oxford University Press, 117–131 (Jan. 2018).
142. Elahian, B., Yeasin, M., Mudigoudar, B., Wheless, J. W. & Babajani-Feremi, A. Identifying seizure onset zone from electrocorticographic recordings: A machine learning approach based on phase locking value. *Seizure* **51**. Publisher: W.B. Saunders, 35–42 (Oct. 2017).
143. Matsumoto, A. *et al.* Pathological and physiological high-frequency oscillations in focal human epilepsy. *Journal of Neurophysiology* **110**, 1958–1964 (Oct. 2013).
144. Sumsky, S. L. & Santaniello, S. Decision Support System for Seizure Onset Zone Localization Based on Channel Ranking and High-Frequency EEG Activity. *IEEE Journal of Biomedical and Health Informatics* **23**, 1535–1545 (July 2019).
145. Greene, P., Li, A., González-Martínez, J. & Sarma, S. V. Classification of Stereo-EEG Contacts in White Matter vs. Gray Matter Using Recorded Activity. *Frontiers in Neurology* **11**. Publisher: Frontiers (2021).
146. Heck, C. N. *et al.* Two-year seizure reduction in adults with medically intractable partial onset epilepsy treated with responsive neurostimulation: Final results of the RNS System Pivotal trial. *Epilepsia* **55**. Publisher: Blackwell Publishing Inc., 432–441 (2014).
147. Morrell, M. J. Responsive cortical stimulation for the treatment of medically intractable partial epilepsy. *Neurology* **77**. Publisher: Lippincott Williams and Wilkins, 1295–1304 (Sept. 2011).
148. Meador, K. J., Kapur, R., Loring, D. W., Kanner, A. M. & Morrell, M. J. Quality of life and mood in patients with medically intractable epilepsy treated with targeted responsive neurostimulation. *Epilepsy and Behavior* **45**. Publisher: Academic Press Inc., 242–247 (Apr. 2015).
149. King-Stephens, D. *et al.* Lateralization of mesial temporal lobe epilepsy with chronic ambulatory electrocorticography. *Epilepsia* **56**. Publisher: Blackwell Publishing Inc., 959–967 (June 2015).
150. Loring, D. W., Kapur, R., Meador, K. J. & Morrell, M. J. Differential neuropsychological outcomes following targeted responsive neurostimulation for partial-onset epilepsy. *Epilepsia* **56**. Publisher: Blackwell Publishing Inc., 1836–1844 (Nov. 2015).
151. Anderson, C. T., Tcheng, T. K., Sun, F. T. & Morrell, M. J. Day-Night Patterns of Epileptiform Activity in 65 Patients with Long-Term Ambulatory Electrocorticography. *Journal of Clinical Neurophysiology* **32**. Publisher: Lippincott Williams and Wilkins, 406–412 (Oct. 2015).
152. Sun, F. T. & Morrell, M. J. Closed-loop Neurostimulation: The Clinical Experience. *Neurotherapeutics* **11**. Publisher: Springer US, 553–563 (July 2014).
153. Bergey, G. K. *et al.* Long-term treatment with responsive brain stimulation in adults with refractory partial seizures. *Neurology* **84**. Publisher: Lippincott Williams and Wilkins, 810–817 (Feb. 2015).
154. Brodie, M. J. *et al.* Commission on European Affairs: Appropriate standards of epilepsy care across Europe. *Epilepsia* **38**. Publisher: Blackwell Publishing Ltd, 1245–1250 (Nov. 1997).

155. Berg, A. T. & Kelly, M. M. Defining intractability: Comparisons among published definitions. *Epilepsia* **47**. Publisher: Blackwell Publishing Inc, 431–436 (Feb. 2006).
156. Kwan, P. & Brodie, M. J. Early Identification of Refractory Epilepsy. *New England Journal of Medicine* **342**. Publisher: Massachusetts Medical Society, 314–319 (Feb. 2000).
157. Wiebe, S., Blume, W. T., Girvin, J. P. & Eliasziw, M. A randomized, controlled trial of surgery for temporal-lobe epilepsy. *New England Journal of Medicine* **345**, 311–318 (Aug. 2001).
158. D’Andrea Meira, I. *et al.* Ketogenic Diet and Epilepsy: What We Know So Far. *Frontiers in Neuroscience* **13**, 5 (Jan. 29, 2019).

Clinical Center Patients						
Clinical Covariate	NIH	JHH	UMMC	UMH	CClinic	Total
Number Patients	14	4	7	5	61	91
Number Success	9	1	7	3	24	44
Number Failure	5	3	0	2	37	47
Number Male	6	n/a	7	1	30	44
Number Female	8	n/a	0	4	31	43

Table -I. A table of number of patients per clinical center (NIH = National Institute of Health; JHH = Johns Hopkins Hospital; UMMC = University of Maryland Medical Center; UMH = University of Miami Jackson Memorial Hospital; CClinic = Cleveland Clinic). Includes number of success, failures, and gender per group. Note that JHH did not retain gender information for these group of patients.

Patient Summary										
Subject	Pathology	Clinical complexity	Engel	ILAE	Ethnicity	Age	Onset Age	Handedness	Sex	Months Follow Up
E1	FCD type IIb	4	III	4	Caucasian	9	2	R	M	24
E3	FCD type IIb	1	I	4	Asian	13	9	R	F	6
E4	FCD type IIb	1	I	4	Caucasian	11	10	L	M	14
E5	FCD type IIa and IIb	4	I	4	Asian	11	9	R	M	24
E6	FCD type IIb	1	I	4	Caucasian	14	8	R	F	7
E7	left amygdala enlargement and hippocampal signal changes	2	I	4	LatinX	17	11	R	M	3

Table -II. A table of patients in study from the Hospital for Sick Children - There was a subject E2 with similar types of procedure done, but the dataset had different electrodes implanted before and after resection, rather than the same electrodes as with the rest of patients. We categorized patients by their clinical complexity (CC) as follows: (1) lesional, (2) focal temporal, (3) focal extratemporal, and (4) multi-focal^{Bulacio2016, Sheik2019}. If a patient presents with multiple categories, they are filed in the more complex case. Some patients presented with focal cortical dysplasia (FCD).

Patient Summary							
Subject	Clinical complexity	Engel	Age	Onset Age	Handedness	Sex	Months Follow Up
TVB01	2	I	36	7	n/a	M	12

Table -III. A table of patients in study used for TVB simulations.

Appendix I

Appendix

A. Estimating a linear time-invariant model from data

For each 500 ms window, we constructed a discrete-time linear time invariant model (of the form eq. 2.1) from the intracranial EEG recordings, which led to a sequence of models $\{\mathbf{A}_j\}$ for $j = 1, 2, \dots, 120$. Specifically, each recording from electrode i was considered a realization of a state variable $\mathbf{x}_i(t)$ for $i = 1, 2, \dots, N$ assumed to be generated by model $\mathbf{x}(t+1) = \mathbf{A}_j \mathbf{x}(t)$ for $t \in [500(j-1), 500j]$. Each state evolution matrix \mathbf{A}_j was estimated by minimizing the squared error between the data and the model. That is, $\|\mathbf{x}(t) - \hat{\mathbf{x}}(t)\|_2$ was minimized over \mathbf{A}_j such that $\hat{\mathbf{x}}(t+1) = \mathbf{A} \hat{\mathbf{x}}(t)$.

The following variables describe a window of data:

- T = window size (500 ms)
- N = number of electrodes
- $\mathbf{b} \in \mathbf{R}^{(T-1)N}$, where \mathbf{b} are the electrode recordings at the next time point
- $\mathbf{H} \in \mathbf{R}^{(T-1)N \times N^2}$
- $\mathbf{A} \in \mathbf{R}^{N \times N}$, where \mathbf{A} is the vectorized adjacency matrix we are interested in
- $\mathbf{x}_i(t), t = 1, 2, \dots, T$, are the iEEG time series from each window of electrode i

The model for the adjacency matrix is constructed by transforming the data and unknowns into a linear system of equations: $\mathbf{b} = \mathbf{H}\mathbf{X}$, and then solving the least squares problem in MATLAB using $\mathbf{X} = \mathbf{H} \setminus \mathbf{b}$. The following system of linear equations comes directly from writing out the recursion of the LTI model for each time step:

$$\begin{aligned} x_1(2) &= A_{1,1}x_1(1) + A_{1,2}x_2(1) + \dots + A_{1,N}x_N(1) \\ x_2(2) &= A_{2,1}x_1(1) + A_{2,2}x_2(1) + \dots + A_{2,N}x_N(1) \end{aligned}$$

⋮

$$\begin{aligned} x_N(2) &= A_{N,1}x_1(1) + A_{N,2}x_2(1) + \dots + A_{N,N}x_N(1) \\ x_1(3) &= A_{1,1}x_1(2) + A_{1,2}x_2(2) + \dots + A_{1,N}x_N(2) \\ x_2(3) &= A_{2,1}x_1(2) + A_{2,2}x_2(2) + \dots + A_{2,N}x_N(2) \end{aligned}$$

⋮

$$x_1(T) = A_{1,1}x_1(T) + A_{1,2}x_2(T) + \dots + A_{1,N}x_N(T)$$

⋮

$$x_N(T) = A_{N,1}x_1(T) + A_{N,2}x_2(T) + \dots + A_{N,N}x_N(T)$$

The model matrices are constructed as such and solved for each window.

$$\mathbf{b} = [x_1(2) \ x_2(2) \ \dots \ x_N(2) \ \dots \ x_1(T) \ x_2(T) \ \dots \ x_N(T)]^T$$

$$\mathbf{H} = \begin{bmatrix} x_1(1) \ \dots \ x_N(1) & 0 \ \dots \ 0 & 0 \ \dots \ 0 \\ 0 \ \dots \ 0 & x_1(1) \ \dots \ x_N(1) & 0 \ \dots \ 0 \\ \dots & \dots & \dots \\ 0 \ \dots \ 0 & 0 \ \dots \ 0 & x_1(1) \ \dots \ x_N(1) \\ \dots & \dots & \dots \\ x_1(2) \ \dots \ x_N(2) & 0 \ \dots \ 0 & 0 \ \dots \ 0 \\ \dots & \dots & \dots \\ 0 \ \dots \ 0 & 0 \ \dots \ 0 & x_1(2) \ \dots \ x_N(2) \\ \dots & \dots & \dots \\ x_1(T) \ \dots \ x_N(T) & 0 \ \dots \ 0 & 0 \ \dots \ 0 \\ \dots & \dots & \dots \\ 0 \ \dots \ 0 & 0 \ \dots \ 0 & x_1(T) \ \dots \ x_N(T) \end{bmatrix}$$

$$\mathbf{X} = [A_{11} \ A_{12} \ \dots \ A_{1N} \ A_{21} \ \dots \ A_{N,N-1} \ A_{NN}]^T$$

After solving for \mathbf{X} , it can be reshaped into a matrix \mathbf{A} . For each estimated \mathbf{A}_j , we then computed the minimum norm perturbation Γ_j for a row perturbation and the corresponding fragility metric $\|\hat{\Delta}_j\|_k$ at each node $k = 1, \dots, N$. The fragility metric is computed as:

$$\begin{aligned} j &= 1, \dots, 120, \text{ is the time indice.} \\ k &= 1, \dots, N, \text{ is the electrode indice.} \\ \|\hat{\Delta}_j\|_k &= (\max(\Gamma_j) - \Gamma_{j_k}) / \max(\Gamma_j) \end{aligned}$$

With the estimated minimum norm perturbation for each channel at each time window, the iEEG time series data can be used to determine fragility changes of each electrode over time. For each time window j , we have N values of fragility, one for each electrode k . We form a fragility matrix \mathbf{F} as follows:

$$\mathbf{F} = \begin{bmatrix} \|\hat{\Delta}_1\|_1 & \|\hat{\Delta}_2\|_1 & \dots & \|\hat{\Delta}_{120}\|_1 \\ \|\hat{\Delta}_1\|_2 & \|\hat{\Delta}_2\|_2 & \dots & \|\hat{\Delta}_{120}\|_2 \\ \dots & \dots & \dots & \dots \\ \|\hat{\Delta}_1\|_N & \|\hat{\Delta}_2\|_N & \dots & \|\hat{\Delta}_{120}\|_N \end{bmatrix}$$

B. Supplementary Figures

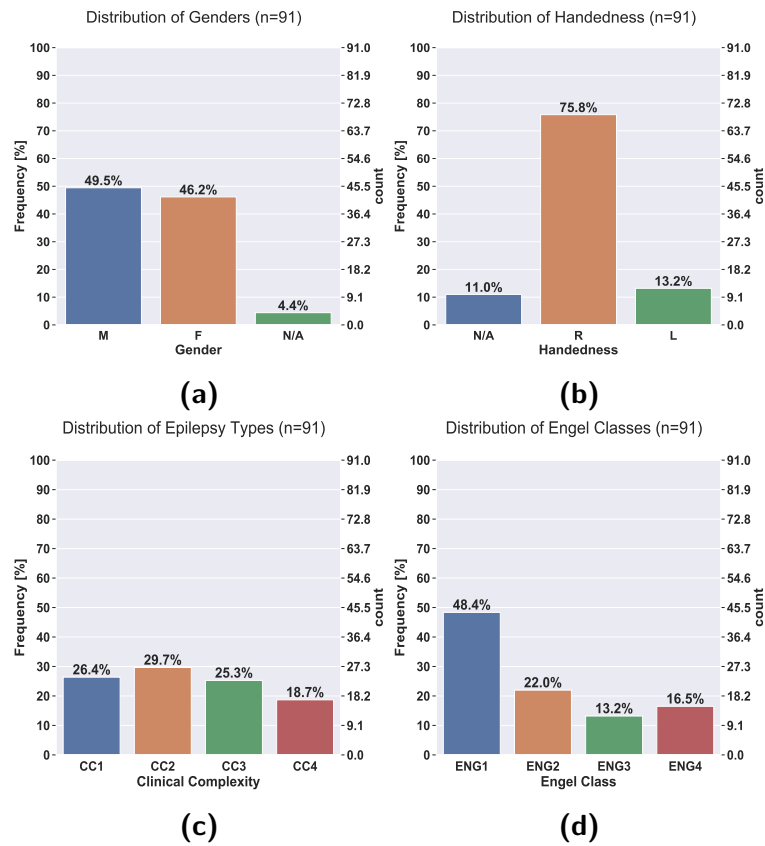


Figure I-1. Distributions of the 91 patient dataset based on a variety of clinical factors, such as gender **(a)**, handedness **(b)**, clinical complexity **(c)**, and Engel class **(d)**. The plots show distributions over the 91 patients used in analysis.

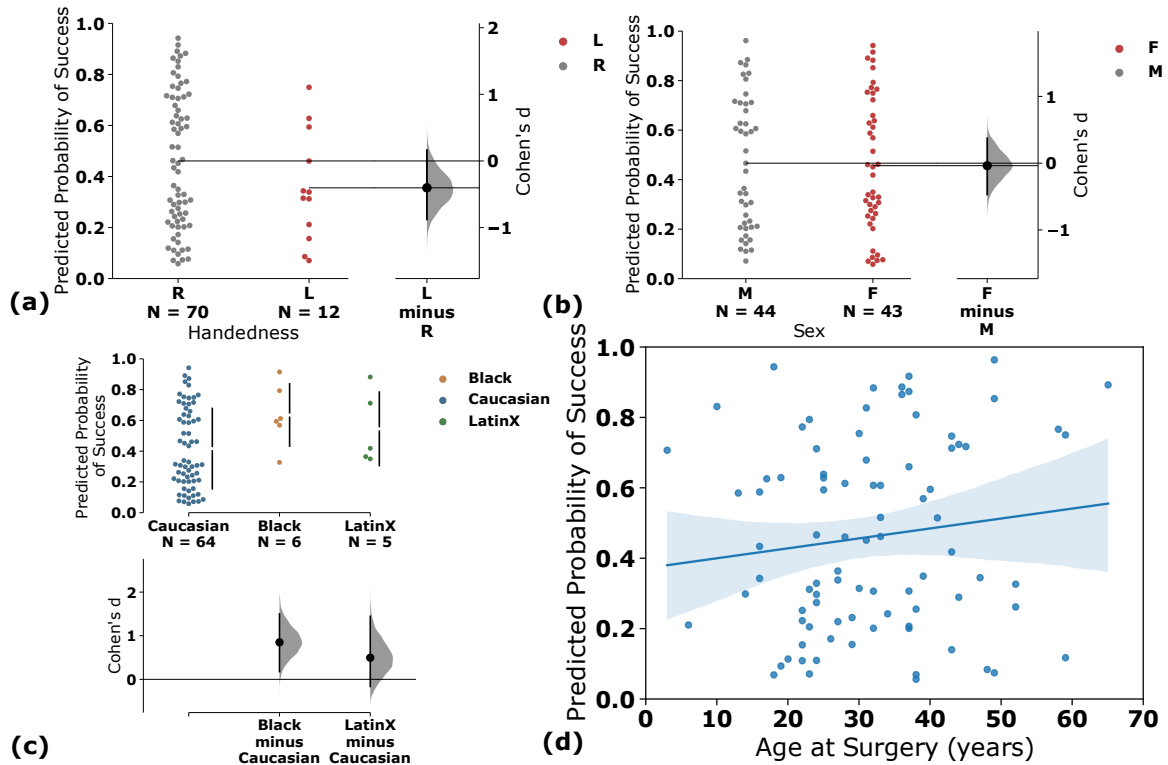


Figure I-2. Neural fragility correlation against non-epileptic clinical covariates - Fragility success probabilities (denoted as "Confidence Statistic" in y-axes) split by clinical factors, such as handedness **(a)**, gender **(b)**, ethnicity **(c)** and age at surgery **(d)**. Not all patients had data for each of these categories, so the subset of available data was used. Note the sample sizes vary across different groups shown. For ethnicity, we also had 1 Asian subject, but left it out because the permutation effect size estimation procedure does not work for 1 sample. Effect sizes were estimated using the permutation test and Mann Whitney U test described in ???. The corresponding effect sizes and p-values were (0.1/0.99) for handedness, and (0.12/0.7) for gender. The p-value was computed using the one-sided Mann-Whitney U test. The slope was negligibly close to 0 for surgery age linear fit. There was no relatively significant trend in the data related to ethnicity. The significant Cohen's D effect size difference is primarily due to the low sample sizes in non-Caucasian ethnicities. The error bars represent 95% confidence interval specified by 2 standard deviations.

3400 North Charles Street
 Baltimore, Maryland 21202 USA
 (+1) 805.807.5898
ali39@jhu.edu

EDUCATION AND DEGREES

2015–Present PhD Graduate student, Department of Biomedical Engineering
 Johns Hopkins University

2019–2021 MS Graduate student, Department of Applied Mathematics & Statistics
 Johns Hopkins University

2010–2015 Undergraduate student, Department of Bioengineering and Department of Mathematics
 University of California

RESEARCH EXPERIENCE

Johns Hopkins University

Department of Biomedical Engineering

(Aug. 2015–Present)

Graduate Student in the laboratory of a Dr. Sridevi Sarma

- Coordinated data pipeline of electrophysiological and clinical data of epilepsy patients from 5 hospitals in coordination with clinicians in setting up a HIPAA-compliant server for highly parallelized data analysis, resulting in **Nature Neuroscience publication**.
- Identified and developed signal processing and statistical analysis of clinical multi-modality datasets that resulted in over 400 pull requests merged in open-source packages with up to 1,000's of users (**Git, CI, unit-testing, software design & development**)
- Developed statistical and machine learning models on multivariate time series EEG, clinical and neuroimaging MRI and CT data to analyze different seizure localization models (model building & validation with **scikit-learn/keras/pytorch**, data wrangling with **pandas, numpy**).
- Coordinated open-source discussions on EEG and iEEG data formatting in a 79 international team of researchers on Github (**technical communication of the Brain Imaging Data Structure - BIDS**)
- Coordinated a team of engineers to develop a structure-aware Random Forest algorithm in Python and Cython to perform manifold learning (to be implemented as a PR into **scikit-learn**).

Aix-Marseille University

Theoretical Neurosciences Group

(Aug. 2017–Aug. 2018)

Visiting Research Scientist in the laboratory of a Dr. Viktor Jirsa

- Developed a high-throughput parallelized data pipeline for multi-modality 3D brain imaging using **Bash and Snakemake (Python DAG engine)** resulting in robust 3D brain visualizations.
- Designed **nonlinear biophysical models** with **linear dynamical systems analysis** to predict the surgical outcome in epileptic patients resulting in a paper to be submitted to Brain
- Developed a supervised deep learning pipeline using nonlinear computational modeling and a Recurrent-CNN model to perform patient-specific seizure detection (**Python/Keras/Pytorch**)
- Implemented open-source code on *The Virtual Brain* (a Human Brain Project) for generating observational noise, analysis of simulated source signals and scientific demos

TECHNIQUES AND SKILLS

Computing and Other Skills

- Power user of Linux/Unix and Macintosh systems
- Basic R and C++ programming
- Proficient at AWS usage, unit testing and continuous integration

- Expert at open source software
- Expert Python programming (Numpy, Scipy, Scikit-learn, Xarray, Pytorch, Keras, Tensorflow)
- Ethical use of human data in research

TEACHING EXPERIENCE

Johns Hopkins University (Sept. 2019-Jan. 2020)

Teaching Assistant

- NeuroData Design Course (BME 580.638): develop open source contributions to Python scientific computing libraries

Johns Hopkins University, Some school (Jan. 2019-May 2019)

Head Teaching Assistant

- Systems Bioengineering II Course (BME 580.424): coordinate 150 students and 6 TAs

University of California (Sept. 2014-May 2015)

Teaching Assistant

- Undergraduate Student Instructor for Data Structures Course (CSE 12) - C, C++.

PUBLICATIONS

[Neural Fragility as an EEG Marker of the Seizure Onset Zone.](#) Adam Li, C. Huynh, Z. Fitzgerald, I. Cajigas, D. Brusko, J. Jagid, A. Claudio, A. Kanner, J. Hopp, S. Chen, J. Haagensen, E. Johnson, W. Anderson, N. Crone, S. Inati, K. Zaghoul, J. Bulacio, J. Gonzalez-Martinez, S. V. Sarma. *Nature Neuroscience* **10.1038/s41593-021-00901-w**. (2021).

[Neural Fragility of the Intracranial EEG Network Decreases after Surgical Resection of the Epileptogenic Zone.](#) Adam Li, P. Myers, N. Warski, K. Gunnarsdottir, S. Kim, V. Jirsa, A. Oichi, H. Otusbo, G. Ibrahim, S. V. Sarma. *MedRxiv* **10.1101/2021.07.07.21259385**. (2021).

[Manifold Oblique Random Forests: Closing the Gap on Convolutional Neural Networks.](#) Adam Li*, R. Perry*, C. Huynh*, T. M. Tomita, R. Mehta, J. Arroyo, J. Patsolic, B. Falk, S. V. Sarma, J. T. Vogelstein. *ArXiv* **abs/1909.11799**. (2021).

[Classification of Stereo-EEG Contacts in White Matter vs. Gray Matter Using Recorded Activity.](#) P. Greene, Adam Li, J. González-Martínez, S. V. Sarma. *Frontiers in Neurology* **11**. 1806 (2021).

[Using network analysis to localize the epileptogenic zone from invasive EEG recordings in intractable focal epilepsy.](#) Adam Li*, B. Chennuri*, S. Subramanian, R. Yaffe, S. Gliske, S. William, R. Norton, A. Jordan, K. Zaghoul, S. Inati, S. Agrawal, J. Haagensen, J. Hopp, C. Atallah, E. Johnson, N. Crone, W. Anderson, Z. Fitzgerald, J. Bulacio, J. Gale, S. V. Sarma, J. Gonzalez-Martinez. *Network Neuroscience* **02**. 218–240 (2018).